UNIVERSITY of CALIFORNIA
Santa Barbara

Micro-Optomechanical Systems for Quantum Optics

A dissertation submitted in partial satisfaction of the
requirements for the degree of

Doctor of Philosophy

in

Physics

by

Dustin Paul Kleckner

Committee in charge:

Professor Dirk Bouwmeester, Chair
Professor Andrew Cleland
Professor Leon Balents

March 2010

The dissertation of Dustin Paul Kleckner is approved:

Professor Andrew Cleland

Professor Leon Balents

Professor Dirk Bouwmeester, Chair

March 2010

Micro-Optomechanical Systems for Quantum Optics

by

Dustin Paul Kleckner

Acknowledgements

This dissertation would not have been possible without the work of a large number of people. Roger Penrose and Christoph Simon made initial and continuing contributions to the theoretical understanding of the quantum behavior of optomechanical systems, setting the stage for everything that followed. Will Marshall and Michiel de Dood began our experimental work on optomechanical systems, developing the first methods for fabricating tiny mirrors attached to micromechanical resonators and integrating them into high finesse cavities. These methods were further developed by Nima Dinyari, Bart-Jan Pors and Johan de Jong, along with myself. Igor Pikovski, Luuk Ament, and Jeroen van den Brink aided in our analysis of the quantum/classical interpretation of the superposition experiment. Development of cleanroom nanofabrication techniques would not have been possible without the assistance of Susanna Thon, Hyochul Kim, Brian Pepper and Brian Thibeault, along with the rest of the support staff of the UCSB Nanofabrication Facility. William Irvine, Sumant Oemrawsingh and Susanna Thon contributed to the theoretical understanding and simulation of diffraction limited high finesse cavities. Simulations of rough diffraction limited cavities were carried out at the CNSI High Performance Computing Center, with the assistance of Paul Weakliem. Evan Jeffrey and Petro Sonin were instrumental in the development of the cryogenic cavity alignment system at the University of Leiden, which was also greatly aided by Giorgio Frossati, Eric Eliel and Harmen van der Meer. I have also benefited greatly from the presence of all past and present group members that I have not already mentioned: Hagai Eisenberg, Eduardo Fonseca, George Khoury, Juan Hodelin, Matt Rakher, Patrick O'Neill, Iman Aghilian, Jan Gudat, Hubert Krenner, Florian Haupt, Jenna Hagemeier, Amy Thompson, Christian Bonato, Dapeng Ding and Trey Suntrup. Finally, I would like to thank my adviser, Dirk Bouwmeester, for his support and guidance on all aspects of my research.

Curriculum Vitæ

Dustin Paul Kleckner

Education

2010	Ph.D. in Physics, University of California, Santa Barbara
2006	M.A. in Physics, University of California, Santa Barbara
2004	B.A. in Physics and Art, University of Minnesota Twin Cities

Publications

"Diffraction Limited High Finesse Optical Cavities," D. Kleckner, W. Irvine, S. Oemrawsingh and D. Bouwmeester, accepted for publication in *Physical Review A* (2010).

"Creating and verifying a quantum superposition in a micro-optomechanical system," D. Kleckner, I. Pikovski, E. Jeffrey, L. Ament, E. Eliel, J. van den Brink and D. Bouwmeester, *New Journal of Physics* **10**, 095020 (2008).

"Sub-kelvin optical cooling of a micromechanical resonator," D. Kleckner and D. Bouwmeester, *Nature* **444**, 75 (2006).

"High Finesse Opto-Mechanical Cavity with a Movable Thirty-Micron-Size Mirror," D. Kleckner, W. Marshall, M. J. A. de Dood, K. N. Dinyari, B.-J. Pors, W. T. M. Irvine, and D. Bouwmeester, *Physical Review Letters* **96**, 173901 (2006).

Honors and Awards

2004-2006	California NanoSystems Institute Fellow
2004	Graduation with Honors, Summa Cum Laude, University of Minnesota Twin Cities

Abstract

Micro-Optomechanical Systems for Quantum Optics

by

Dustin Paul Kleckner

Optomechanical systems offer a potential platform for testing quantum effects in relatively massive objects. We first examine the theory of optomechanical systems, primarily in the quantum limit, detailing a proposal for generating a superposition of a micro-mechanical resonator and the theory of optical feedback cooling. We then discuss the experimental requirements for observing these quantum effects and our attempts to construct an optomechanical system that meets these requirements. In particular, we describe a prototype system built from a tiny piece of dielectric mirror glued to an atomic force microscopy cantilever and use it to optically cool the cantilever to sub-Kelvin temperatures. In an effort to better understand the optical cavities used in optomechanical systems, we developed a new method for simulating the mode profiles and losses of diffraction limited high-finesse cavities. Finally, we cover our recent efforts to produce an improved optomechanical system, which includes the micro-fabrication of resonators with integrated mirrors, improvements to the optical cavity as a whole and the construction of a system capable of cryogenic temperatures.

Contents

List of Figures

List of Tables

Chapter 1

Introduction

Our initial interest in optomechanical systems began with a proposal to test quantum mechanics on relatively massive scales. In the late-90's, a number of theorists showed that the interaction between an optical cavity and a moving end mirror, mediated by radiation pressure, could be used to generate non-classical mechanical states of the moving end mirror[1–3]. This formed the basis for a proposal by Marshall et al. to create and observe a mechanical resonator in a superposition of vibrational states using the interference between two optical cavities, one of which contains an optomechanical system [4]. If completed, this experiment would constitute a demonstration of quantum mechanics in an object some 10^{12} times more massive than previous realizations involving C_{60} molecules [5, 6] or currents in superconducting devices [7, 8]. Unlike previous proposals, the system described by Marshall et al. appeared to be feasible with state of the art technology.

Shortly after this publication, work on building an appropriate optomechanical system began in the group of Dirk Bouwmeester. This work was initiated by Will Marshall and Michiel de Dood, with myself and others joining later. This resulted in the demonstration of one of the first purpose-built optomechanical systems (§4) and demonstrations of optical feedback cooling (§5), and work continues towards

realization of the original proposal.

Broadly speaking, an optomechanical system is any device with both an optical and mechanical degree of freedom and some coupling between them. The canonical example is a conventional optical cavity where one of the end mirrors is placed on a mechanical resonator. The radiation pressure of the field inside the optical cavity produces a force on the mechanical resonator, and the position of the mechanical resonator/mirror affects the detuning of the cavity. The theory of optomechanical systems in the classical limit began with Braginsky [9]. The first demonstration of the effects he predicted were in conventional microwave and visible-light optical cavities; modifications of the properties of the mechanical modes of the mirrors were observed when they were pumped with large input powers [10–12].

In this dissertation we are primarily concerned with microscopic mechanical systems, where the optomechanical coupling is strong enough that quantum effects can be potentially observed. Microtoroidal resonators could probably be considered the first devices that operated in this regime; the strong driving of vibrational modes via optical pumping was first observed in 2005 [13]. Since that time, a number of micro-optomechanical systems have been created, including gradient-force systems [14], membrane-in-the-middle systems [15] and others [16]. Gradient-force systems are nano-photonic cavities which are coupled to integrated mechanical degrees of freedom. A "membrane-in-the-middle" optomechanical system is made by putting a very thin dielectric membrane in the middle of a high finesse optical cavity. Changes in the position of the membrane cause a shift in the optical cavity modes, resulting in an interaction between the mechanical resonances of the membrane and the optical field. For the purposes of this dissertation, we are mostly concerned with "classic" optomechanical systems, which are quite literally composed of a tiny piece of mirror attached to a micro-mechanical resonator. Despite the rapid development of other types of devices, we believe this system is still best suited to the demonstration of quantum effects. This is

primarily because the clear separation of the optical and mechanical elements of the systems allows for ideal choices of materials and design for each.

Although proposals to create macroscopic superpositions motivated our research on optomechanical systems, a large number of other potential applications have been put forth. In addition to superpositions, optomechanical systems can be used to generate other quantum states in and between the mechanical and optical degrees of freedom. Proposals in this vein include entangling states of mechanical resonators to each other [17] or cavity fields [18], the creation of entangled photon pairs [19], the observation of discrete quantum jumps [15] and the cooling of mechanical resonators to the ground state (§2.3)[20, 21]. The strong interaction between the optical field and the mechanical oscillations makes the cavity behave like a nonlinear medium since the length of the cavity depends upon the intensity of the field in an analogous way to the optical length of a nonlinear material [22]. Because of this, micro-optomechanical systems would make an ideal test bed for ponderomotive squeezing, which has been proposed as a method to reduce noise in gravitational wave detectors [23] and may also have applications in information theory [24].

This thesis is arranged in a mixture of logical and chronological order. §2 begins with a discussion of the theory of optomechanical systems, primarily in a quantum framework, starting with the derivation of the quantum Hamiltonian of a general optomechanical system. This framework is used to describe two important experiments, the superposition proposal of Marshall et al. and optical feedback cooling. The experimental barriers to observing quantum effects in an optomechanical system are then examined in detail, with particular attention paid to the requirements of a superposition-type experiment (§3). Although these two chapters are presented first for clarity, much of the theoretical work was actually done in parallel with the experimental work described later.

§4 describes the realization of a prototype optomechanical system composed

of a tiny piece of dielectric mirror attached to a mechanical resonator. This system was then used to demonstrate active optical feedback cooling (§5). After the completion of this experiment, we began to reconsider the design of our optomechanical system with the goal of meeting the requirements for demonstration of true quantum phenomena. To better understand the effects of diffraction loss on ultra-high finesse optical cavities, we developed a new method for calculating the modes of cavities with finite end mirrors, which is described in §6. This method can be used to determine the effects of cavity geometry and the types of imperfections present in real systems. Finally, §7 describes our recent efforts to build a better optomechanical system, including the creation of micro-optomechanical systems using micro-fabrication techniques, improvement in the optomechanical cavity as a whole and early work on a system which can operate at cryogenic temperatures.

Chapter 2

Theory of Optomechanical Systems

In this chapter we will consider optomechanical systems from a purely theoretical perspective. Because our primary interest in these systems is to use them to demonstrate quantum effects, we begin by deriving the quantum Hamiltonian for a single mode optomechanical system (§2.1). Despite making a number of approximations, we show that this Hamiltonian is appropriate for realistic devices.

We then discuss in detail a proposed experiment for creating and observing a quantum superposition of a micromechanical resonator, using an optomechanical system to couple the quantum state of a single photon to a mechanical degree of freedom (§2.2). At finite temperatures, the mechanical degree of freedom will be excited well out of the ground state, posing significant questions about the interpretation that experiment demonstrates a true quantum superposition. Using the Wigner function as a tool, we examine the effects of temperature and environmentally induced decoherence in detail. We also briefly discuss some proposed mass-induced decoherence mechanisms that have been postulated to arise from the incompatibility of quantum mechanics and gravity. Although decoherence of this type is purely theoretical at present, a superposition experiment with an op-

tomechanical system could offer the first opportunity to probe the relevant mass regime.

In §2.3, we discuss optical feedback cooling, which uses the optical cavity in an optomechanical system to measure and reduce the effective temperature of the mechanical degree of freedom. Feedback cooling potentially allows one to reach the ground state of a mechanical resonator; we will discuss in which regimes this is possible. Finally, we treat one form of optical cooling in the quantum limit and show how it can be used to generate an unambiguous signal that the ground state has been reached. As well as being an interesting demonstration of the quantum nature of the mechanical resonator in its own right, this type of cooling is useful for the realization of the aforementioned superposition proposal as well as a number of related experiments.

2.1 Quantum Hamiltonian

To study optomechanical systems in the quantum limit, one first needs to construct a fully quantum Hamiltonian to describe the coupling between the optical and mechanical degrees of freedom. The simplest representation one can imagine is a 1-D optical cavity with one stationary mirror located at $z = 0$ and one movable mirror located at $z = q$, with mass m and moving in some potential $V(q)$ (fig. 2.1). We will assume both mirrors are perfectly reflecting and the motion of the mirror is non-relativistic. If we treat the optical field as a scalar potential that vanishes at the mirrors (ignoring polarization), the complete Hamiltonian of the system, as found by C.K. Law [25], is given by:

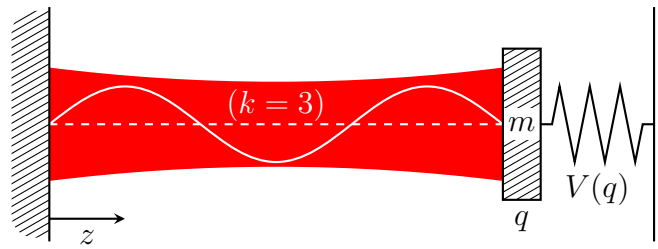

Figure 2.1: A diagram of a 1-D optomechanical system. A moving optical end mirror is located a $z = q$, has mass m and moves in a potential $V(q)$. The electric field of the third optical mode, $k = 3$, is sketched in white.

$$\hat{H} = \frac{(\hat{p} + \hat{\Gamma})^2}{2m} + V(\hat{q}) + \hbar \sum_k \omega_k(\hat{q}) \left[\hat{a}_k^\dagger \hat{a}_k + \frac{1}{2} \right] \tag{2.1}$$

$$\omega_k(\hat{q}) = \frac{k\pi c}{\hat{q}} \tag{2.2}$$

$$\hat{\Gamma} \equiv \frac{i\hbar}{2\hat{q}} \sum_{k,j} g_{kj} \left[\frac{k}{j} \right]^{1/2} \left[\hat{a}_k^\dagger \hat{a}_j^\dagger - \hat{a}_k \hat{a}_j + \hat{a}_k^\dagger \hat{a}_j - \hat{a}_k \hat{a}_j^\dagger \right] \tag{2.3}$$

$$g_{kj} = \begin{cases} (-1)^{k+j} \frac{2kj}{j^2 - k^2} & k \neq j \\ 0 & k = j \end{cases}, \tag{2.4}$$

where k is the longitudinal mode number and ω_k, $\hat{a}$ and $\hat{a}^\dagger$ are the corresponding frequency, annihilation and creation operators; $\hat{\Gamma}$ corresponds to an effective momentum in the opto-mechanical interaction, arising from the mixing of different spatial modes. As usual, the zero point energy of the optical field gives rise to an infinite energy when summing over the full (infinite) set of modes. This can be corrected by calculating the energy density of the continuum of modes outside the cavity and finding the (finite) difference of these two infinite energies as a function of $\hat{q}$. This gives rise to a Casimir term, resulting in a modified Hamiltonian:

$$\hat{H} = \frac{(\hat{p} + \hat{\Gamma})^2}{2m} + V(\hat{q}) + \hbar \sum_k \omega_k(\hat{q}) \hat{a}_k^\dagger \hat{a}_k - \frac{\hbar c \pi}{24 \hat{q}}, \tag{2.5}$$

where the Casimir term would have twice this value if we included polarization.

We can simplify the system by considering only a single optical mode, assuming all others are unpopulated:

$$\hat{H} = \frac{\hat{p}^2}{2m} + V(\hat{q}) + \hbar\omega_a(\hat{q})\hat{a}^\dagger\hat{a} - \frac{\hbar c\pi}{24\hat{q}}, \tag{2.6}$$

where ω_a is now the frequency of the single populated optical mode. Since $\hat{\Gamma}$ gives rise only to terms that mix the different modes, it must be zero if we restrict ourselves to a single mode. As a result, we have implicitly treated the optical field in the adiabatic limit; if the mechanical motion is not slow compared to the round trip time of a photon in the cavity it will cause coupling between the different modes, even if only one is initially occupied (see §2.1.1).

We will continue to simplify the system by assuming that the mechanical potential is harmonic about some equilibrium position L:

$$V(\hat{q}) = m\omega_c^2\hat{x}^2, \tag{2.7}$$

where $\hat{x} = \hat{q} - L$ is the displacement from equilibrium. If the resonator only makes a small motion about this equilibrium position ($\hat{x} \ll L$), we can consider only the first order change in ω_a about this equilibrium point:

$$\hat{H} = \hbar\omega_c\hat{c}^\dagger\hat{c} + \hbar\left[\omega_a(L) + \hat{x}\left.\frac{d\omega_a(\hat{q})}{d\hat{q}}\right|_{\hat{q}=L} + \cdots\right]\hat{a}^\dagger\hat{a} \tag{2.8}$$

$$\cong \hbar\omega_a\hat{a}^\dagger\hat{a} + \hbar\omega_c\hat{c}^\dagger\hat{c} - \underbrace{\frac{\omega_a}{L}x_0}_{g}\left(\hat{c} + \hat{c}^\dagger\right)\hat{a}^\dagger\hat{a}, \tag{2.9}$$

where $\hat{c}^{(\dagger)}$ are the annihilation (creation) operators for the mechanical harmonic oscillator, defined in the usual way, $x_0 = \sqrt{\frac{\hbar}{2m\omega_c}}$ is the size of the ground state wavepacket of the mechanical harmonic oscillator and g is the optomechanical coupling constant. In the second equation, and hereafter, we will let $\omega_a \to \omega_a(L)$. We have used the fact that the mechanical potential is harmonic to obtain: $\hat{x} = x_0\left(\hat{c} + \hat{c}^\dagger\right)$. We have also dropped the Casimir term; for most systems it

is negligibly weak. The second equation, eqn. 2.9, is the canonical optomechanical Hamiltonian, and the usual starting point for the quantum theory of micro-optomechanical systems.

2.1.1 Approximations

Before proceeding, it is worth checking the validity of our assumptions for realistic device parameters:

1. *The mechanical motion is non-relativistic.* The maximum velocity of the mechanical resonator is given approximately by:

$$v_{max} \sim \omega_c x_0 \sqrt{\bar{n}_c}, \tag{2.10}$$

where $\bar{n}_c = \left\langle \hat{c}^\dagger \hat{c} \right\rangle$ is the mean phonon number of the mechanical mode. As we will show in §2.2.4, for the system to be quantum mechanically coherent over a single period, we will require $\bar{n}_c \lesssim Q$, where Q is the mechanical quality factor. For realistic devices, $Q \lesssim 10^6$, $\omega_c \lesssim 10$ GHz and $x_0 \lesssim 1$ pm, and so:

$$v_{max} \lesssim 10 \text{ m/s} \ll c. \tag{2.11}$$

2. *We can consider only a single optical mode.* Even if we only excite a single optical mode, the equivalent momentum term $(\hat{p}+\hat{\Gamma})^2$ in the full Hamiltonian (eqn. 2.1) contains terms that mix the longitudinal optical modes. The lowest order cross terms will be of the form: $\hat{c}^{(\dagger)}\hat{a}_k^{(\dagger)}\hat{a}_{k\pm1}^{(\dagger)}$, where the $(\dagger)$ indicates these may be either creation or annihilation operators. These terms only conserve energy if the mechanical frequency is comparable to the spacing between optical modes:

$$\omega_c \sim \Delta\omega_a = \frac{\pi c}{L}. \tag{2.12}$$

If these terms do not conserve energy, they will not contribute significantly to the time evolution of the system (this is the commonly used rotating

wave approximation). In a relatively long optical cavity with $L = 100$ mm, the mode spacing is $\Delta\omega \sim 10$ GHz, which is comparable to the highest frequency one could expect to reach in an optomechanical resonator. Despite this, increasing the frequency, ω_c, and cavity length, L, both decrease the optomechanical coupling, g, making it very difficult to achieve sufficiently strong photon-phonon coupling in these systems. For exactly this reason, we will generally be concerned with much lower frequency systems (kHz - MHz), and hence $\omega_c \ll \Delta\omega_a$. In this case we can ignore $\hat{\Gamma}$, even when multiple modes are occupied.

The condition that the mechanical frequency must be much smaller than the mode splitting is equivalent to requiring that the mechanical period is much longer than the round trip time of a photon in the cavity. Thus we see that considering only a single mode implicitly treats the optical field in the adiabatic limit.

3. *The mechanical motion is small compared to the cavity length.* The maximum displacement will be given by:

$$x_{max} \sim x_0\sqrt{\bar{n}_c}. \tag{2.13}$$

The shortest possible optical cavity has length $\lambda/2$, where λ is the wavelength of relevant mode of the optical cavity; $\lambda \sim 1$ μm for practical cavities. Thus we find:

$$x_{max} \lesssim 1 \text{ nm} \ll \frac{\lambda}{2} \sim 500\text{nm}. \tag{2.14}$$

4. *The Casimir force is negligible.* For a real 3-D optical cavity, some number of transverse optical modes will be supported in addition to the fundamental. This should multiply the Casimir energy by some constant, N_m, corresponding to the effective number of modes*. If we then expand the total Casimir

* It may seem odd that the form of the Casimir energy used here has a different dependence

energy, the first three terms correspond to a constant energy, a constant force and an effective spring constant, $k_{casimir}$, respectively:

$$E_{casimir} = -\frac{N_m \hbar c \pi}{24L}\left[1 - \underbrace{\frac{\hat{x}}{L}}_{\text{constant force}} + \underbrace{2\left(\frac{\hat{x}}{L}\right)^2}_{\text{effective spring}} + \cdots\right] \tag{2.15}$$

$$k_{casimir} = -\frac{N_m \hbar c \pi}{6L^3} \tag{2.16}$$

$$= 1.6 \times 10^{-6}\left(\frac{N_m}{100}\right)\left(\frac{1\mu\text{m}}{L}\right)^3 \text{N m}^{-1}. \tag{2.17}$$

From calculations of the modes of diffraction limited optical cavities (§6), we expect that a cavity that is the minimum size required for supporting a large optical finesse ($F \sim 10^6$) should support on the order of 10–100 transverse modes. The constant force term changes the equilibrium position of the resonator, but has no other effect. The $\hat{x}^2$ term changes the effective spring constant of the mechanical resonator, but the magnitude is negligibly small for systems where the cavity length is of order centimeters. For wavelength-sized cavities (e.g. gradient force systems), this term is orders of magnitude small than the mechanical spring constant of realistic systems, although it should be observable in a specially designed system (with, for example, oversized mirrors). Higher order terms will have a considerably smaller effect, and should be negligible in realistic systems. In this case, the effect of the Casimir energy is to modify the effective frequency and equilibrium position of the mechanical resonator, but this does not change the system dynamics

than the normal three dimensional result: $E_{casimir} = -A\frac{\hbar c \pi^2}{720L^3}$ [26]. However, we note that the number of modes supported decreases with the separation; from the properties of the light diffraction, we should expect: $N_m \propto L^{-2}$. Substituting this into the 1-D form of the Casimir energy recovers the expected dependence. For a high finesse optomechanical system, it is advantageous to minimize the size/mass of the system as much as possible, so the resonator mirrors are expected to have the minimum size needed for achieving the required optical quality. In this case the number of modes becomes: $N_m \to N_0\left(1 + \hat{x}/L\right)^2$, where N_0 is the number of modes at the equilibrium length of the cavity. Assuming we are in the regime where $\hat{x} \ll L$, we can take N_m to be nearly constant.

in any meaningful way.

There is one more assumption that we have ignored: that the mirrors are perfectly reflecting. Removing this assumption requires one to add terms corresponding to coupling to modes outside the cavity – in many cases these terms give rise to interesting physics. There are several well established formalisms for dealing with this coupling (e.g. §2.2.4 or §2.3.1), but they do not require modification of the base system Hamiltonian so long as the coupling is weak, in the so-called "good-cavity limit." (This means that the damping rate for both the mechanical and optical degrees of freedom is much less than the respective frequencies; when this is not the case the system can no longer be truly considered a resonator.)

2.1.2 Generalization to Related Systems

Although the Hamiltonian (eqn. 2.9) was derived for a simple cavity with one moving end mirror, it is also used for all types of optomechanical systems. In general, the coupling constant g is given by the energy detuning of the optical mode in response to the mechanical motion of the system, which is assumed to be linear:

$$g = -\frac{d\omega_a}{dx}\sqrt{\frac{\hbar}{2m\omega_c}}, \tag{2.18}$$

where the derivative is taken at the equilibrium point of the mechanical mode.

The method used to calculate the detuning depends on the type of system in question. In gradient-force systems, the optical mode frequency is typically computed at a range of different mechanical displacements via numerical finite-difference time-domain (FDTD) simulations [27].

Alternatively, for a membrane-in-the-middle optomechanical system, the detuning can be calculated by considering the interference of a 1-D dielectric membrane in an optical cavity [15], which could be done, for example, with a thin film interference matrix method (as described by [28], for example). If the reflectivity of the membrane alone is of order $R \sim \frac{1}{2}$ and it is placed at an anti-node of

the cavity mode, the shift is roughly equivalent to moving the entire end mirror. Conversely, placing the membrane at a node of the cavity produces no shift to first order. In this case the leading optomechanical interaction term is quadratic in $\hat{x}$, producing entirely different system dynamics. This is potentially useful for a different class of experiments, e.g. directly measuring phonon quantization.

2.2 The Superposition Experiment

There are a number of proposals for the creation of massive quantum superpositions or so-called "Schrödinger's cat" states using optomechanical systems [2–4]. We now examine in detail this class of experiments, in particular the one described in Marshall et al. [4]. This section is adapted from *The New Journal of Physics* **10**, 095020, "Creating and verifying a quantum superposition in a micro-optomechanical system," by D. Kleckner et al. [29]. Copyright ©2008 by Deutsche Physikalische Gesellschaft & Institute of Physics.

The heart of this experiment is a Michelson interferometer with high finesse optical cavities in each of its arms (fig. 2.2). In one arm the traditional end mirror is replaced with a tiny mirror on a micromechanical cantilever. Under the right conditions, the radiation pressure of a single photon in this arm of the experiment will be strong enough to excite the cantilever into a distinguishable quantum state. A single photon incident on the 50-50 beam splitter will form an optical superposition of being in either of the two arms; the coupling between the photon and the cantilever will then entangle their states, putting the cantilever into a superposition of vibrational states. If the photon leaves the interferometer with the cantilever in a distinguishable state, an outside observer could in principle determine which arm the photon took, and so the interference visibility is destroyed. After a full mechanical period of the cantilever, however, it returns to its original position: if the photon leaves the interferometer at this time, the

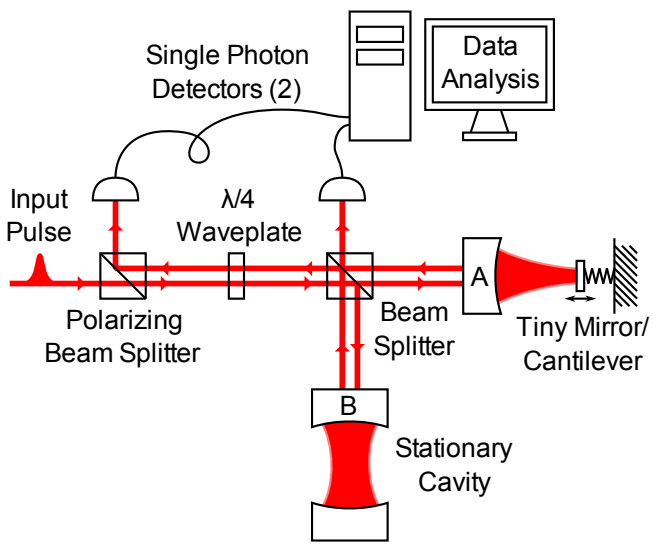

Figure 2.2: A diagram of the experimental setup for measuring a macroscopic quantum superposition. An input pulse is split between the two arms of a Michelson interferometer, labeled A and B, both of which contain high finesse cavities. One end of the cavity in arm A is a tiny mirror on a micromechanical cantilever, whose motion is affected by the radiation pressure of light in the cavity. Each output port of the interferometer is monitored by a single photon detector, and results are analyzed by a computer to calculate the interference visibility.

interference visibility should return provided the cantilever was able to remain in a quantum superposition in the intermediate period. Alternatively, if the state of the cantilever collapses during this period due to environmentally induced decoherence, measurement by an outside observer or perhaps an exotic mechanism (e.g. [30–32]), the visibility will not return. In this sense the interference revival constitutes evidence that the cantilever was able to exist in a quantum superposition, and a measurement of its magnitude constitutes a measurement of the quantum decoherence in this time interval. In a real experiment, however, one must be careful about drawing conclusions from the visibility dynamics; as we shall see, similar results can be obtained from a fully classical argument.

2.2.1 Quantum Mechanical Description

To calculate the quantum evolution of this experiment, we begin with the basic Hamiltonian for an optomechanical system, eqn. 2.9, to which we add a term corresponding to the stationary optical cavity, labeled B:

$$H = \hbar\omega_a \left[\hat{a}^\dagger \hat{a} + \hat{b}^\dagger \hat{b}\right] + \hbar\omega_c \left[\hat{c}^\dagger \hat{c} - \kappa \hat{a}^\dagger \hat{a} \left(\hat{c} + \hat{c}^\dagger\right)\right], \tag{2.19}$$

where $\hat{b}^{(\dagger)}$ are the the photon annihilation (creation) operators for the stationary optical cavity, which we will assume is resonant with the optical cavity that includes the micromechanical element ($\omega_b = \omega_a$). As before, $\hat{a}^{(\dagger)}$ and ω_a refer to the optical degree of freedom of the optomechanical system, and $\hat{c}^{(\dagger)}$, ω_c and m refer to the mechanical motion. For convenience, we have also defined a dimensionless optomechanical coupling constant κ:

$$\kappa = \frac{g}{\omega_c} \tag{2.20}$$

$$= \frac{2x_0 N}{\lambda}, \tag{2.21}$$

where $N = \pi c/\omega_c L$ is the number of cavity round trips per mechanical period and $\lambda = 2\pi c/\omega_a$ is the wavelength of the optical cavity resonance.

From the Hamiltonian we can derive the unitary evolution operator [2]:

$$U(t) = \exp\Big[- i\omega_a t \left(\hat{a}^\dagger \hat{a} + \hat{b}^\dagger \hat{b}\right) - i \left(\kappa \hat{a}^\dagger \hat{a}\right)^2 (\omega_c t - \sin \omega_c t) \Big] \times \\ \exp\Big[\kappa \hat{a}^\dagger \hat{a} \left[\left(1 - e^{-i\omega_c t}\right) \hat{c}^\dagger - \left(1 - e^{i\omega_c t}\right) \hat{c}\right] \Big] \exp\Big[- i\omega_c \hat{c}^\dagger \hat{c} t\Big]. \tag{2.22}$$

If we consider a cantilever initially in a coherent state with complex amplitude β, the total initial state is given by $|\,\Psi(0)\rangle = \frac{1}{\sqrt{2}} \left(|\,0,1\rangle_{n_a,n_b} + |\,1,0\rangle_{n_a,n_b}\right) \otimes |\,\beta\rangle_c$. Under the action of the unitary operator, eqn. 2.22, this unentangled state evolves to:

$$\begin{aligned} |\,\Psi(t)\rangle &= \frac{1}{\sqrt{2}} e^{-i\omega_a t} \Big(|\,0,1\rangle \otimes |\,\beta e^{-i\omega_c t}\rangle + \\ &\quad e^{i\kappa^2(\omega_c t - sin(\omega_c t)) + i\kappa \mathrm{Im}[\beta(1-e^{-i\omega_c t})]} |\,1,0\rangle \otimes |\,\kappa(1 - e^{-i\omega_c t}) + \beta e^{-i\omega_c t}\rangle \Big) && (2.23) \\ &= \frac{1}{\sqrt{2}} e^{-i\omega_a t} \Big(|\,0,1\rangle \otimes |\,\Phi_0(t)\rangle + \\ &\quad e^{i\kappa^2(\omega_c t - sin(\omega_c t)) - i\mathrm{Im}[\Phi_0(t)\Phi_1(t)^*]} |\,1,0\rangle \otimes |\,\Phi_1(t)\rangle \Big). && (2.24) \end{aligned}$$

Because the cantilever is only displaced if the photon is in arm A, the state of the photon and the state of the cantilever become entangled. The cantilever then enters a superposition of two different coherent states, with time dependent amplitude $\Phi_0(t)$ when no photon is present in arm A and $\Phi_1(t)$ if there is a photon. After half a mechanical period, the spatial distance between the two cantilever states $|\,\Phi_0\rangle$ and $|\,\Phi_1\rangle$ is given by $\Delta x = 2\kappa x_0$, and the two cantilever states have the minimum overlap, $|\langle \Phi_0 \,|\, \Phi_1\rangle| = e^{-2\kappa^2}$. After a full mechanical period, $|\,\Phi_0\rangle$ and $|\,\Phi_1\rangle$ are identical again, and so the photon and cantilever are disentangled. For a proper demonstration of a superposition, we require the overlap between the states to be relatively small during part of the experiment, implying $\kappa \gtrsim 1/\sqrt{2}$. This is equivalent to stipulating that a measurement of the cantilever state alone is sufficient to determine which path a photon took with reasonable fidelity. As will be discussed in §3.1, obtaining a sufficiently large value of κ is the a significant experimental challenge.

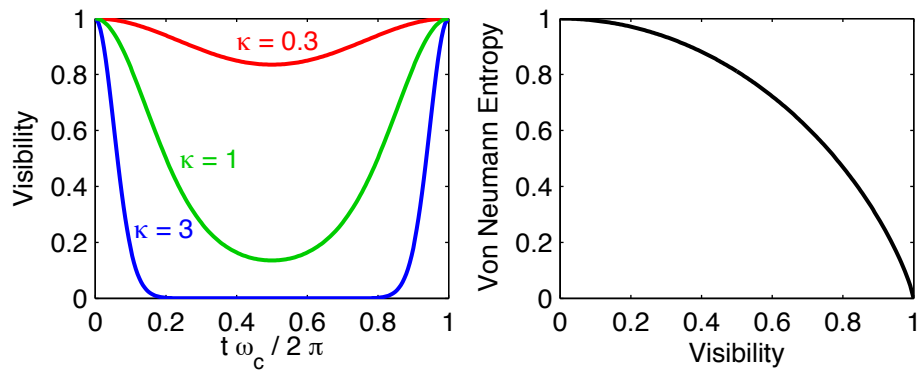

Figure 2.3: Left: The visibility $v(t)$ as a function of time for different values of the opto-mechanical coupling constant, κ. Right: The Von Neumann entropy $S(t)$ versus the visibility, $v(t)$.

In practice, the actual quantity measured is the interferometric visibility as seen by the two single photon detectors. This visibility is given by twice the absolute value of the off-diagonal elements of the reduced photon density matrix:

$$v(t) = e^{-\kappa^2[1-\cos(\omega_c t)]}. \tag{2.25}$$

As expected, it exhibits a periodic behavior characterized by a suppression of the interference visibility after half a mechanical period and a revival of perfect visibility after a full period (fig. 2.3) provided there is no decoherence in the state of the cantilever. The visibility can be mapped directly to the entanglement between the photon and the cantilever. For a pure bipartite state, we can express the entanglement as the von Neumann entropy of the photon $S(t)$ in terms of the visibility $v(t)$ (fig. 2.3):

$$S(t) = -\mathrm{Tr}_{\mathrm{ph}}\left(\rho_{\mathrm{ph}} \log_2 \rho_{\mathrm{ph}}\right) \tag{2.26}$$

$$= 1 + \frac{v(t)}{2}\log_2\left(\frac{1-v(t)}{1+v(t)}\right) - \frac{1}{2}\log_2\left(1-v(t)^2\right), \tag{2.27}$$

where ρ_{ph} is the reduced density matrix for the photon. Since for a pure bipartite system a high Von Neumann entropy of one subsystem corresponds to high entanglement between the two subsystems, we conclude that when the initial state

is pure, the visibility alone is a good measure of the non-classical behavior of the cantilever. This is true even in the presence of an arbitrary decoherence mechanism, which will destroy the off diagonal elements of the density matrix and thus produce a corresponding loss of interference visibility.

2.2.2 Finite temperatures

At finite temperatures the exact wavefunction of the cantilever is unknown, so the state is instead described by a density matrix:

$$\rho_c(0) = \frac{\sum_n e^{-E_n/k_BT} |\, n\rangle\langle n\,|}{\sum_n e^{-E_n/k_BT}} \tag{2.28}$$

$$= \frac{1}{\pi\bar{n}_c}\int d^2\beta e^{-|\beta|^2/\bar{n}_c} |\,\beta\rangle\langle\beta\,|, \tag{2.29}$$

where $\bar{n}_c = 1/(e^{\hbar\omega_c/k_BT} - 1)$ is the average thermal occupation number of the cantilever's mechanical mode, $|\,n\rangle$ are energy eigenstates and $|\,\beta\rangle$ are coherent states of the cantilever. The evolution of this thermal mixture under the action of eqn. 2.22 yields the visibility:

$$v(t) = e^{-\kappa^2(2\bar{n}_c+1)[1-\cos(\omega_c t)]}. \tag{2.30}$$

At finite temperatures the density matrix represents an average over coherent states with different phases which destroys the interference visibility. Although there is also a phase shift from the coherent state discussed earlier, in principle this shift is known and repeatable, while the same is not true for the thermal state. A good indicator that the visibility no longer captures the quantum behavior is that it becomes independent of $\hbar$ if the initial temperature of the cantilever is high [33]. This can be seen most easily by noting that in the limit $k_bT \gg \hbar\omega_c$, the mean phonon number is given by $\bar{n}_c \approx k_bT/\hbar\omega_c - 1/2$. Thus the visibility (eqn. 2.30) can be rewritten as:

$$v(t) \approx e^{-\frac{k_bT}{m\omega_c^2}\left(\frac{2N}{\lambda}\right)^2[1-\cos(\omega_c t)]}, \tag{2.31}$$

which is independent of $\hbar$. This is the classically expected result, which differs primarily from the quantum result in that the visibility is always one at zero temperature because the distinguishability of the cantilever state is irrelevant. At higher temperatures it is difficult to determine when the cantilever was in a superposition state because the loss of visibility due to classical phase scrambling dominates over that due to distinguishability. The relationship between von Neumann entropy and the visibility, eqn. 2.27, still holds, but at $T > 0$ the system is in a mixed state. Thus the entropy is only an upper bound for the entanglement of formation [34].

The net phase shift from any coherent state goes to zero after a full mechanical period, and so full visibility should still return in a narrow window whose width scales like $\bar{n}_c^{-1/2}$. This leaves open the possibility for measuring quantum collapse mechanisms at finite temperatures if one creates the appropriate conditions to put the cantilever into a superposition state. Provided that the opto-mechanical coupling strength κ is relatively well known (e.g., by independently measuring m, ω_c, L, etc.) and the instantaneous quantum state of the cantilever is regarded as some random coherent state (as should be the case for the weakly mechanically damped systems discussed here) it can be easily determined when a superposition must have been created.

Although eqn. 2.31 suggests that the visibility should always return in the classical case, we note that this can only be true if both the photon *and* the cantilever are behaving classically. On the other hand, if we regard only the photon as a quantum object we should always expect full visibility loss because we can measure the cantilever state with arbitrary precision and hence always determine which path the photon took. Thus the return of visibility at higher temperatures can be used to strongly imply the existence of a quantum superposition when $\kappa \gtrsim 1/\sqrt{2}$, even though the superposition can not be directly measured by the

visibility loss† at $t \sim \pi/\omega_c$.

2.2.3 The Wigner Function and the Classical Limit

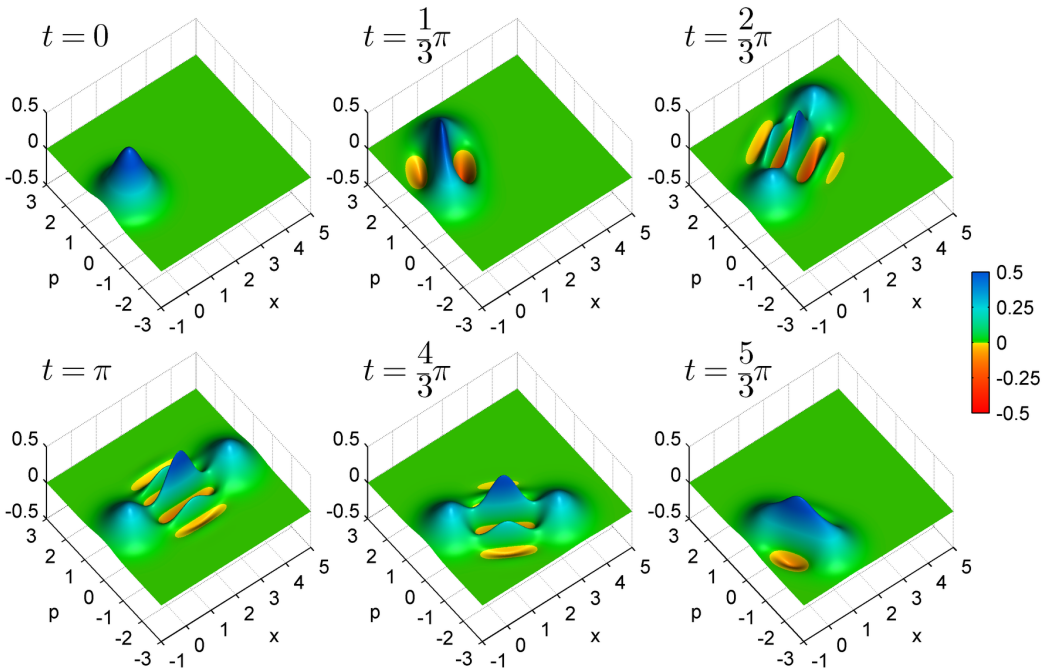

Figure 2.4: The time evolution of the cantilever's projected Wigner function for $\beta = 0$, $\kappa = 2$ and $\hbar = \omega_c = m = 1$. Regions where the Wigner function is negative, shown in yellow and red, have no classical analogue.

To study transitions between the quantum and the classical regimes, it is often convenient to refer to quasi-probability distributions, with which quantum mechanics can be formulated in the common classical phase space. One such

†The presence of a loop hole in such a demonstration could be regarded as analogous to experimental tests of Bell's inequalities, where even though it is generally regarded that hidden variable theories have been ruled out, an unambiguous proof has remained elusive. In our case, the loop hole is caused by the unknown intermediate state; even though a weakly damped system should produce something that is very nearly a coherent state at any given instant in time, there is no way to directly show the cantilever is in this state.

distribution was proposed in 1932 by Wigner [35] and can be obtained from the density matrix ρ:

$$W(x,p) = \frac{1}{\pi\hbar}\int_{-\infty}^{+\infty} dy \langle x-y\,|\rho|\,x+y\rangle e^{2ipy/\hbar}. \tag{2.32}$$

It is well known that in the classical limit, $\hbar \to 0$, the Wigner function tends to a classical probability distribution describing a microstate in phase space [36]. This can most easily be seen in the case of a single particle moving in a potential $V(x)$. The time evolution of the Wigner function for this closed system is described by the quantum Liouville equation [35, 37]:

$$\begin{aligned}(\frac{\partial}{\partial t} + \frac{p}{m}\frac{\partial}{\partial x} - \frac{dV(x)}{dx}\frac{\partial}{\partial p})\, W(x,p,t) = \\ \sum_{k=1}^{\infty} \hbar^{2k} \frac{(-1)^k}{4^k(2k+1)!}\frac{d^{2k+1}V(x)}{dx^{2k+1}}\frac{\partial^{2k+1}}{\partial p^{2k+1}} W(x,p,t).\end{aligned} \tag{2.33}$$

For $\hbar \to 0$, the right hand side goes to 0, as long as no derivatives diverge. In this limit the Wigner function $W(x,p,t)$ thus evolves according to the classical Liouville equation. However, the quantum nature of $W(x,p,t)$ is also contained in its initial conditions. In fact, in the special case of a harmonic potential, all non-classical behavior is encoded in the initial conditions of the Wigner function only since the right hand side of eqn. 2.33 is always 0. For $\hbar \to 0$ the initial conditions also become classical and $W(x,p,t)$ can be fully identified with some classical probability density.

If, on the other hand, the Wigner function is negative then no classical interpretation is possible, making it a useful tool to indicate the non-classicality of an arbitrary state. It is thus convenient to quantify the total negativity of the Wigner function [38]:

$$\begin{aligned} N &= \int_{-\infty}^{+\infty} dx \int_{-\infty}^{+\infty} dp \Big\{ |W(x,p)| - W(x,p) \Big\} \\ &= \int dx \int dp\, |W(x,p)| - 1. \end{aligned} \tag{2.34}$$

For the experiment at hand, we compute the cantilever's Wigner function for dimensionless x and p, with the photon projected into the superposition state $|\,0,1\rangle + e^{i\theta}|\,1,0\rangle$ to avoid destroying the quantum state of the cantilever to which it is entangled. This projection is equivalent to detecting a single photon at one output of the interferometer, where the phase term in the projection accounts for path length differences in the arms. Generally speaking, varying θ shifts the interference peaks but does not modify the Wigner function in a significant way; hereafter we will set it to 0. The resulting Wigner function of the cantilever indeed shows that the system periodically exists in a highly non-classical state (fig. 2.4).

A calculation of the thermally averaged Wigner function shows that the non-classical features are quickly washed out with increasing initial temperature (fig. 2.5). However, as long as part of the Wigner function is negative, the cantilever is clearly in a non-classical superposition state. The negativity of the Wigner function at half a mechanical round trip time decreases rapidly with $\bar{n}_c$ and is also dependent on κ (fig. 2.6). In practice, this implies that $\bar{n}_c$ must be of order 1 for $\kappa \approx 1$, with somewhat higher values being tolerable for higher κ. This analysis confirms our earlier assertion that a *direct proof* that the superposition existed requires low mean phonon number. Paradoxically, if one is willing to accept that a superposition was created, a low thermal excitation is not required to test if this superposition survives after one mechanical period of the cantilever.

2.2.4 Environmentally Induced Decoherence

In addition to "classical" phase scrambling caused by the initial thermal motion of the cantilever as discussed above, there are other effects which cause "quantum" decoherence of the cantilever. The signature of this type of decoherence is a reduction of the amplitude of the visibility of the revival peak, whereas the signature of thermal decoherence is a narrowing of the revival peaks. To be able to detect a signature of a macroscopic superposition, the timescale on which quantum

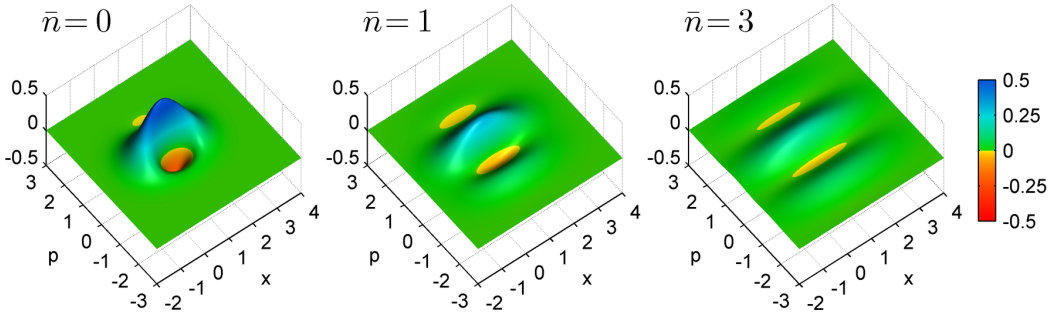

Figure 2.5: The thermally averaged projected Wigner function of the cantilever at time $t = \pi$ for $\kappa = 1/\sqrt{2}$ and different mean thermal phonon numbers, $\bar{n}_c$. ($\hbar = \omega_c = m = 1$) The negative regions of the Wigner function, shown in yellow and red, can be seen to quickly wash out with increasing temperature.

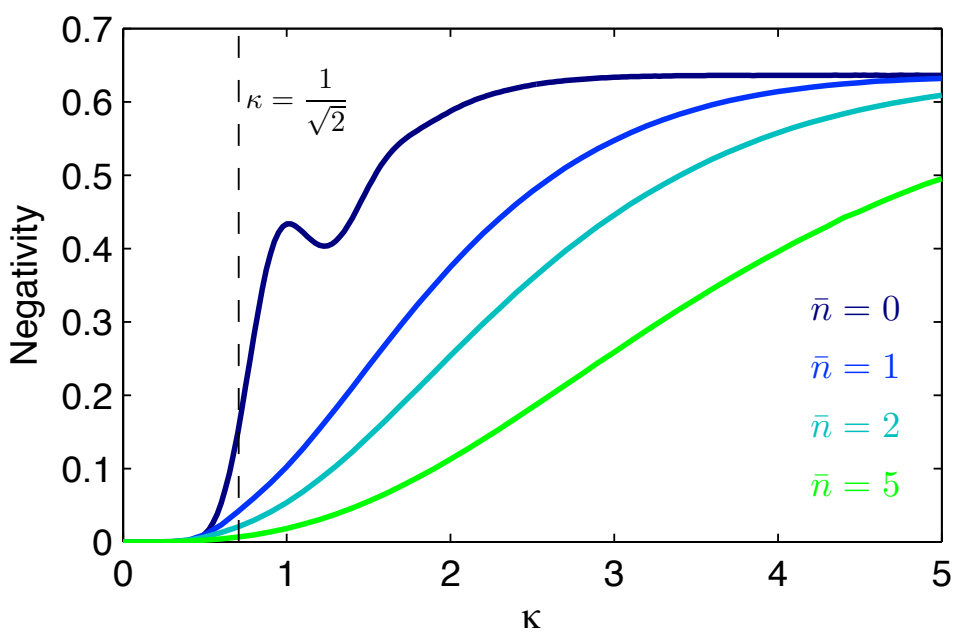

Figure 2.6: Negativity of the projected cantilever state as a function of coupling constant κ for several different mean phonon numbers, $\bar{n}$. The oscillations present when $\bar{n} = 0$ are due to a phase shift in the interference terms, which are washed out at higher temperatures.

decoherence occurs should be larger than a single mechanical period.

Environmentally induced decoherence is due to the coupling of the system to a finite temperature bath. Decoherence happens when the thermal bath measures the state of the cantilever while the photon is in the cavity, introducing a phase shift that can not be compensated for, even in principle. To find the time scale for this mechanism we need to solve the open quantum representation of the system. This is generally done by coupling the cantilever to an infinite bath of harmonic oscillators and integrating out the environmental degrees of freedom. In doing so, one obtains a time-local master equation for the density matrix of the system incorporating the influence of the environment.

We start with the Hamiltonian:

$$H = H_{sys} + H_{bath} + H_{int}, \tag{2.35}$$

where:

$$\begin{aligned} H_{sys} &= \hbar\omega_a \left[\hat{a}^\dagger \hat{a} + \hat{b}^\dagger \hat{b}\right] + \hbar\omega_c \left[\hat{c}^\dagger \hat{c} - \kappa \hat{a}^\dagger \hat{a} \left(\hat{c} + \hat{c}^\dagger\right)\right] \\ H_{bath} &= \sum_i \hbar\omega_i \hat{d}_i^\dagger \hat{d}_i \\ H_{int} &= (\hat{c} + \hat{c}^\dagger) \sum_i \lambda_i (\hat{d}_i + \hat{d}_i^\dagger). \end{aligned} \tag{2.36}$$

Here $\hat{d}_i^\dagger$ ($\hat{d}_i$) are the creation (annihilation) operators of the bath modes, ω_i is the frequency of each mode and λ_i are coupling constants. Using the Feynman-Vernon Influence Functional Method [39] we can eliminate the bath degrees of freedom. When the thermal energy of the bath sets the highest energy scale we can use the Born-Markov approximation to obtain a master equation for the density matrix of our system [40]:

$$\dot{\rho}(t) = \frac{1}{i\hbar}\left[\tilde{H}_{sys}, \rho(t)\right] - \frac{i\gamma}{\hbar}\left[x, \{p, \rho(t)\}\right] - \frac{D}{\hbar^2}\left[x, [x, \rho(t)]\right], \tag{2.37}$$

where $\tilde{H}_{sys}$ is the system Hamiltonian in eqn. 2.19, renormalized by the interaction of the cantilever with the bath, $\gamma = \omega_c/Q$ is the damping coefficient as

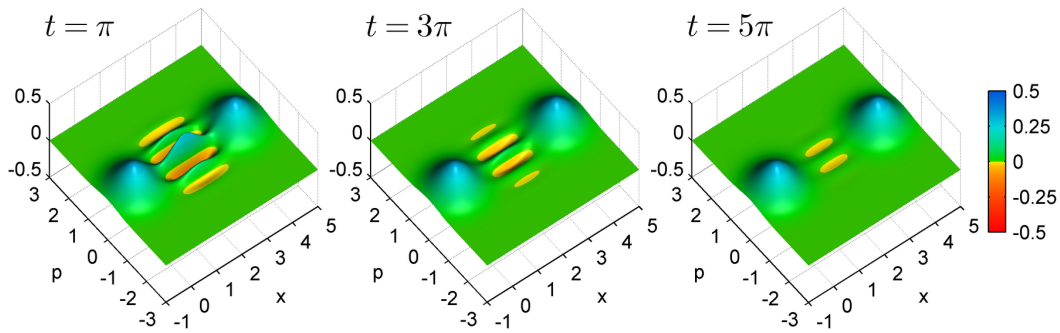

Figure 2.7: Wigner function of the system in the presence of environmentally induced decoherence for $T_b = T_{EID}/16$, $\kappa = 2$ and $\hbar = \omega_c = m = 1$ (eqn. 2.39).

determined from the mechanical Q factor and $D = 2m\gamma k_B T_b$ is the diffusion coefficient where T_b is the temperature of the bath. The first term on the right hand side of eqn. 2.37 is the unitary part of the evolution with a renormalized frequency. The other terms are due to the interaction with the environment only and incorporate the dissipation and diffusion of the cantilever. The equation is valid in the Markovian regime, or when memory effects in the bath can be neglected; this is the appropriate regime when the coupling to the bath is weak ($Q \gg 1$) and the thermal energy is much higher than the phonon energy ($k_B T_b \gg \hbar\omega_c$). Both conditions are easily satisfied for realistic devices.

Following Zurek [41], we note that in the macroscopic regime (to highest order in $\hbar^{-1}$), the master equation is dominated by the diffusion term proportional to $D/\hbar^2$. Evaluating it in the position basis, one finds the time scale:

$$\tau_{\text{dec}} = \frac{\hbar^2}{D(\Delta x)^2} = \frac{\hbar Q}{4k_B T_b \kappa^2}, \tag{2.38}$$

where $\Delta x = 2\kappa x_0$, as before. A calculation of the Wigner function which includes decoherence of the off-diagonal elements with the above dependence shows how the non-classicality of the state dissipates with time (fig. 2.7).

An exact open quantum system analysis of the experimental setup based on eqn. 2.37 has been performed by Bassi et al. [42] and Bernád et al. [33]. Bassi et

al. neglect the term proportional to p in eqn. 2.37 and solve the resulting equation for the off-diagonal matrix elements of the reduced photon density matrix. Bernád et al. use the full equation. The results for the decoherence of the revival peaks in both papers are remarkably close to the above estimate, differing only by a factor of 2/3. The order of magnitude is thus well captured by eqn. 2.38.

For an optomechanical system the important parameter is the mechanical quality factor, Q. It is convenient to define a characteristic environmentally induced decoherence temperature:

$$T_{EID} = \frac{\hbar\omega_c Q}{k_b}. \tag{2.39}$$

With this definition, the decoherence time (eqn. 2.38) can be written as $\tau_{\text{dec}}^{-1} = 4\kappa^2\omega_c\left(\frac{T_b}{T_{EID}}\right)$. If we require that $\tau_{dec} > 2\pi/\omega_c$, this results in a minimum quality factor as a function of temperature and optomechanical coupling strength:

$$Q > 8\pi\kappa^2\bar{n}_c. \tag{2.40}$$

At higher temperatures the interference revival peak will be drastically reduced in magnitude. We note that the environmentally induced decoherence rate is dependent only on the bath temperature, T_b, not on the effective temperature of the cantilever mode, T, which can be made different from the bath temperature by optical cooling (see §2.3).

2.2.5 Anomalous Decoherence Mechanisms

To explain the apparent classicality of the macroscopic world, it has been suggested that there may be an undiscovered quantum state collapse mechanism for large objects, perhaps induced by gravity. Several proposals have been made for a mechanism which would lead to such a collapse, among them reformulations of quantum mechanics [43, 44] and the use of the intrinsic incompatibility between general relativity and quantum mechanics [30–32]. Unlike environmentally induced decoherence, which is largely a nuisance in the realization of a massive

superposition experiment, measurement of a mass induced collapse would be evidence of new physics and is hence of considerable interest.

To give an order of magnitude estimate for proposed mass-induced state collapse mechanisms, we will follow Penrose [31]. He argues that a superposition of a massive object will result in the co-existence of two different space-time geometries which cannot be reconciled, eventually causing the superposition to collapse. To estimate the timescale of this collapse, Penrose calculates the difference of free falls (geodesics) throughout the two space-times, which turns out to correspond to the gravitational self energy ΔE of the superposed system, defined the following way:

$$E_{i,j} = -G \iint d\vec{r_1} d\vec{r_2} \, \frac{\rho_i(\vec{r_1})\rho_j(\vec{r_2})}{|\vec{r_1} - \vec{r_2}|} \tag{2.41}$$

$$\Delta E = 2E_{1,2} - E_{1,1} - E_{2,2}, \tag{2.42}$$

where ρ_1 and ρ_2 are the mass distributions for the two states in question. This energy yields a timescale for the decay of a superposition given by $\tau_G \approx \hbar/\Delta E$.

When attempting to apply this to the proposed superposition experiment, it is unclear precisely what form the mass distributions should take. For simplicity we will consider the mass to be evenly distributed over a number of spheres, corresponding to atomic nuclei, each with mass m_1 and radius a. The superposition states are separated by a distance Δx and the total mass is given by m, as before. If the atomic spacing is much larger than the effective mass radius, the energy due to the interaction between different atomic sites is negligible and the gravitational self-energy is given by:

$$\Delta E = 2Gmm_1 \left(\frac{6}{5a} - \frac{1}{\Delta x} \right) \quad \text{(given: } \Delta x \geq 2a\text{)}. \tag{2.43}$$

If we set the sphere radius to be the approximate size of a nucleus ($a = 10^{-15}$ m) and use the parameters of an ideal optomechanical device (eqn. 3.1 with $\kappa = 1/\sqrt{2}$ and $m_1 = 4.7 \times 10^{-26}$ kg, the silicon nuclear mass), this results in a timescale of

order milliseconds. Alternatively, one could argue that the effective diameter of the spheres should be the ground-state wavepacket size ($a = x_0$). With the same device parameters as before, this results in a timescale on the order of 1 second.

In order to practically measure such a collapse mechanism, we require the timescale to be not much larger than a mechanical period so that a significant visibility reduction is present in the first revival peak. Thus it may be possible to measure a mass-induced collapse effect with the proposed experiment, but only if the size of the atomic nucleus gives the appropriate mass distribution scale. As we are speculating on unknown physics, we note also that the collapse timescale given above is only intended to be an order of magnitude estimate. To contrast with previous large superposition experiments, the collapse timescale for interferometry of large molecules like C_{60} [5] is calculated to be 10^{10} s (using the nuclear radius, $a = 10^{-15}$ m, and assuming comparatively larger separation). Other demonstrated experiments have similar or larger timescales, meaning a collapse mechanism of this type would have certainly been undetectable in all experiments to date.

2.3 Optical Cooling

Optical feedback cooling of micromechanical resonators is caused by an effective damping force produced by the optomechanical interaction. It can be seen how this produces cooling by considering the spectral density of the resonator displacement in the presence of a virtual viscous force. We will initially assume the ideal case where the virtual viscous force introduces no noise into the system. Let us first consider the thermal noise spectrum of a fully classical mechanical resonator, resulting from white noise thermal fluctuations (sometimes referred to as the Langevin force) acting on the mechanical response of a harmonic oscillator [45]:

$$S_x(\Omega) = \frac{2\gamma_c k_b T_0}{m} \frac{1}{(\Omega^2 - \omega_c^2)^2 + \gamma_c^2 \omega_c^2}, \tag{2.44}$$

where Ω is the observation frequency, γ_c is the mechanical damping constant, k_b is Boltzmann's constant and T_0 is the ambient temperature.

Now let us assume that we can increase the damping constant, γ_c, via some external feedback without modifying the thermal input noise:

$$S_{x,fb}(\Omega) = \frac{2\gamma_c k_b T_0}{m} \frac{1}{(\Omega^2 - \omega_c^2)^2 + (1+\eta)^2 \gamma_c^2 \omega_c^2}, \tag{2.45}$$

where η is the strength of the feedback, relative to the intrinsic mechanical damping: $\eta = 0$ corresponds to no feedback, while $\eta > 0$ corresponds to feedback damping. Eqn. 2.45 is equivalent to eqn. 2.44, with a modified temperature and damping constant:

$$T_{eff} = \frac{T_0}{1+\eta} \tag{2.46}$$

$$\gamma_{eff} = (1+\eta)\gamma_c, \tag{2.47}$$

where the reduction in temperature is referred to as feedback cooling. This is equivalent to coupling the system to two thermal baths, one at temperature T_0 (with coupling constant γ_c), and another with zero temperature and coupling constant $\eta\gamma_c$. Although the introduction of damping without noise appears to violate the fluctuation-dissipation theorem, this need not be the case if the feedback mechanism is driven far out of equilibrium. For example, the feedback can be provided by the radiation pressure of an intensity modulated laser, in which case the effective temperature of the laser light is well below the ambient temperature. In any real experiment, the feedback will have some finite noise temperature, which will in general limit the degree of optical cooling that can be achieved.

The fact that the effective damping constant is increased to compensate for the decrease in temperature means that the Langevin force, the effective force caused by thermally induced fluctuations, remains unchanged in the presence of optical cooling. Unfortunately this means that optical cooling does not improve the sensitivity of many experiments that can be aided by conventional cooling;

in particular this applies to atomic force microscopy, scanning probe microscopy, and other related continuous force measurements[‡]. Despite this, optical cooling in combination with conventional cooling may be the only practical method to access the ground state of mechanical resonators in the range of kHz to MHz, which have equivalent temperatures of order nK to μK. As well as being an interesting demonstration of the quantum nature of mechanical resonators, reaching low quantum number states is crucial to realizing many proposed experiments to observe quantum effects in optomechanical systems (e.g. the superposition experiment).

Several methods have been employed for producing the required low noise feedback. Perhaps the most straightforward method is to read out the position of the resonator using an optical cavity as an interferometer and then produce a force proportional to the resonator's velocity via an externally controllable source and an electronic feedback loop. We will refer to this as active optical cooling and it has been demonstrated using both radiation pressure [45, 47] and a piezoelectric element [48] as the source of feedback force. Our own demonstration of active optical cooling, using a prototype optomechanical system, is discussed in detail in §5. For micro-optomechanical systems, this method is typically limited by the noise in the readout system, the effects of which will overwhelm the thermally induced fluctuations once the gain is made high enough. If this noise could be reduced to the quantum level, it has been shown that it is theoretically possible to reach the "ground state" [49], which we will take to mean that the average phonon occupation number of the mechanical resonator is much less than one.

A different type of optical feedback cooling uses the optical field inside the cavity to produce an intrinsic damping force, which we will refer to as passive optical cooling. This happens when a force resulting from the cavity optical field

[‡] Although in practice many of these experiments actually use a feedback mechanism that is equivalent to feedback cooling (for example, [46]). Reducing the effective Q increases the detection bandwidth and provides some practical advantages, even if the noise density is constant or even increased by the feedback.

has a sufficiently delayed response to changes in the length of the cavity. In most experiments [15, 50–59] the force comes from the radiation pressure of the field in the optical cavity, which has a delayed response relative to the resonator position because of the finite cavity ring down time. Another possibility is to use thermally induced bending caused by absorption heating of the cavity field [50, 60, 61], known as the photothermal force, which has a response time on the order of milliseconds for micromechanical resonators [47]. The intensity of the field inside the optical cavity, which is responsible for the force in either case, can be made dependent on the resonator's position by detuning the pump laser with respect to the central cavity resonance, where the sign of the response is dependent on the direction of detuning. If we assume the equilibrium force on the resonator is linearly dependent on resonator position (which is generally true on the length scales of the thermal fluctuations) and decays exponentially with some rate Γ, the effective restoring force at a given frequency is:

$$\tilde{k}_{eff}(\Omega) = k_0 \int_{-\infty}^{\infty} \mathrm{d}t \left(\Gamma e^{-\Gamma t}\right) e^{-i\Omega t} = k_0 \left[1 + \left(\frac{\Omega}{\Gamma}\right)^2\right]^{-1/2} e^{i\phi}, \tag{2.48}$$

$$\phi = \tan^{-1}\left(\frac{\Omega}{\Gamma}\right) \tag{2.49}$$

where $k_0 = \frac{\mathrm{d}F}{\mathrm{d}x}$ for the optically induced delayed force at low frequencies. For a resonator at frequency ω, we can see that as the force decay time becomes of the same order as or longer than a mechanical period, or $\Gamma \lesssim \omega$, the induced restoring force becomes primarily imaginary. This means it will be dissipative, assuming the sign of k_0 is right. For $\Gamma \gtrsim \omega$ there is also a significant component of the optically induced force proportional to the position of the resonator, typically referred to as the optical spring. This will modify the resonance frequency of the resonator, although this effect is usually of secondary importance for micromechanical systems. However, in the case that the optical spring constant becomes larger than (and has the same sign as) the mechanical spring constant this will provide an-

other type of optical cooling by increasing the frequency without changing the thermally induced force; this effect has been observed in gram scale mirrors suspended from thin wires [53, 56]. Unfortunately this effect only happens when the detuning is opposite of that required for the more common form of optical cooling, so the two effects can only be combined with a system involving multiple pump lasers.

Although either type of optical cooling is theoretically capable of reaching the ground state, passive optical cooling is the most promising for reaching the quantum limit of micro-optomechanical systems. This is primarily because the detection and feedback is intrinsic to the cavity; the absence of an external feedback loop eliminates many sources of noise (even with a noiseless feedback loop, active cooling to the ground state requires almost perfect detection efficiency and mode coupling to avoid unwanted shot noise). As we shall show, measurement of the Stokes sidebands in the outgoing cavity light also provides a robust method to determine when the ground state has been reached, which can only be indirectly inferred in an active scheme. We now develop a quantum theory of optical cooling, following Wilson-Rae et al. [20] and Marquardt et al. [21].

2.3.1 Aside: Input-Output Formalism for Damped Quantum Systems

To consider feedback cooling in the quantum limit, we need a formalism for dealing with damped systems. Input-output formalism, developed by C. W. Gardiner and M. J. Collett [62], is a convenient choice which will also allow clear identification of the effects of the different sources of noise. As before, to consider an open system we must add a thermal bath and an interaction term to the Hamiltonian. We will assume the bath is comprised of an infinite set of harmonic oscillators and that the coupling is linear:

$$\hat{H} = \hat{H}_{sys} + \hat{H}_B + \hat{H}_{int} \tag{2.50}$$

$$\hat{H}_B = \hbar \int_{-\infty}^{\infty} \mathrm{d}\omega\, \omega \hat{b}^\dagger(\omega)\hat{b}(\omega) \tag{2.51}$$

$$\hat{H}_{int} = i\hbar \int_{-\infty}^{\infty} \mathrm{d}\omega\, \kappa(\omega) \left[\hat{b}^\dagger(\omega)\hat{c} - \hat{c}^\dagger \hat{b}(\omega)\right], \tag{2.52}$$

where $\hat{b}^{(\dagger)}$ is the bath annihilation (creation) operator, $\hat{c}^{(\dagger)}$ is some arbitrary operator on $\hat{H}_{sys}$ and $\kappa(\omega)$ is the coupling strength between the bath and the system. The integration limits of $(-\infty, \infty)$ are an approximation which simplifies the calculation; in the limit that the system is weakly damped ($Q \gg 1$) it does not affect the results.

As before, we will assume the system is Markovian, and so take the coupling constant to be independent of frequency:

$$\kappa(\omega) = \sqrt{\gamma/2\pi} \tag{2.53}$$

The equation of motion for the system can be calculated by working out the Heisenberg equations of motion for the bath operators and then tracing over the bath modes. For an arbitrary system operator, $\hat{a}$:

$$\dot{\hat{a}} = -\frac{i}{\hbar}\left[\hat{a}, \hat{H}_{sys}\right] - \left[\hat{a}, \hat{c}^\dagger\right]\left[\frac{\gamma}{2}\hat{c} + \sqrt{\gamma}\hat{b}_{in}(t)\right] + \left[\frac{\gamma}{2}\hat{c}^\dagger + \sqrt{\gamma}\hat{b}^\dagger_{in}(t)\right]\left[\hat{a}, \hat{c}\right], \tag{2.54}$$

where we have defined the input noise as:

$$\hat{b}_{in}(t) = \frac{1}{\sqrt{2\pi}} \int_{-\infty}^{\infty} \mathrm{d}\omega\, e^{-i\omega(t-t_0)} \hat{b}_0(\omega). \tag{2.55}$$

This satisfies the following commutation relation:

$$\left[\hat{b}_{in}(t), \hat{b}^\dagger_{in}(t')\right] = \delta(t - t'). \tag{2.56}$$

For the case that the system is a harmonic oscillator with $\hat{c} = \hat{a}$, this takes the simple form:

$$\dot{\hat{a}} = -i\omega_0 \hat{a} - \frac{\gamma}{2}\hat{a} - \sqrt{\gamma}\hat{b}_{in}(t) \tag{2.57}$$

Finally, we note the form of $\hat{b}_{in}$:

$$\mathrm{Tr}\left[\rho_{in}\hat{b}^\dagger_{in}(t)\hat{b}_{in}(t')\right] = \left\langle \hat{b}^\dagger_{in}(t)\hat{b}_{in}(t')\right\rangle = \bar{N}\delta(t - t') \tag{2.58}$$

$$\mathrm{Tr}\left[\rho_{in}\hat{b}_{in}(t)\hat{b}^{\dagger}_{in}(t')\right] = \left\langle \hat{b}^{\dagger}_{in}(t)\hat{b}_{in}(t')\right\rangle = \left(\bar{N}+1\right)\delta(t-t') \tag{2.59}$$

Or, in the frequency basis:

$$\left\langle \hat{b}^{\dagger}_{in}(\omega)\hat{b}_{in}(\omega')\right\rangle = \bar{N}\delta(\omega-\omega') \tag{2.60}$$

$$\left\langle \hat{b}_{in}(\omega)\hat{b}_{in}(\omega')^{\dagger}\right\rangle = \left(\bar{N}+1\right)\delta(\omega-\omega'), \tag{2.61}$$

where we have assumed $\bar{N}$ is a constant, which should be an acceptable approximation for a weakly damped system[§].

2.3.2 Passive Optical Cooling in the Quantum Limit

To develop a quantum theory of feedback cooling, we begin by adding two baths (one optical and one mechanical) to eqn. 2.9, as well as an optical driving term which corresponds to a laser at frequency ω with arbitrary amplitude A, which puts the optical field into a coherent state.

$$\begin{aligned}\hat{H} =& \hbar w_a \hat{a}^{\dagger}\hat{a}\left[1-g\left(\hat{c}+\hat{c}^{\dagger}\right)\right] + \hbar w_c \hat{c}^{\dagger}\hat{c} + \hbar A e^{-i\omega t}\left(\hat{a}+\hat{a}^{\dagger}\right) + \\ & \hat{H}_{B,a} + \hat{H}_{int,a} + \hat{H}_{B,c} + \hat{H}_{int,c}\end{aligned} \tag{2.62}$$

We now calculate the time evolution of the operators using the input-output formalism:

$$\dot{\hat{a}} = -i\omega_a\hat{a}\left[1-g\left(\hat{c}+\hat{c}^{\dagger}\right)\right] - iAe^{-i\omega t} - \frac{\gamma_a}{2}\hat{a} - \sqrt{\gamma_a}\hat{a}_{in} \tag{2.63}$$

$$\dot{\hat{c}} = -i\omega_c\hat{c} + ig\hat{a}^{\dagger}\hat{a} - \frac{\gamma_c}{2}\hat{c} - \sqrt{\gamma_c}\hat{c}_{in}, \tag{2.64}$$

where $\hat{a}_{in} \equiv \hat{b}_{a,in}$ and $\hat{c}_{in} \equiv \hat{b}_{c,in}$. While it would be possible to numerically simulate these equations, we can solve them analytically by assuming that the state of the optical field differs only slightly from a coherent state. Thus we make

[§] In principle, $\bar{N}$ should depend on frequency, i.e.: $\bar{N}(w) = \frac{1}{\exp(\hbar\omega/kT)-1}$. If the system only responds to a narrow bandwidth, as is usually the case, we can ignore the frequency dependence.

the substitution $\hat{a} \rightarrow e^{-iwt}\left(\bar{a}+\hat{d}\right)$, where $\bar{a}$ is a constant and $\hat{d}$ represents the quantum fluctuations of the system. This is a reasonable substitution provided $\left\langle \hat{d}^\dagger \hat{d} \right\rangle \ll |\bar{a}|^2$. Thus the equation of motion for $\hat{d}$ is:

$$\dot{\hat{d}} = i\Delta\left(\bar{a}+\hat{d}\right) + ig\underbrace{\left(\bar{a}+\hat{d}\right)}_{\approx\bar{a}}\left(\hat{c}^\dagger+\hat{c}\right) - iA - \frac{\gamma}{2}\left(\bar{a}+\hat{d}\right) - \underbrace{e^{+iwt}\sqrt{\gamma_a}\hat{a}_{in}}_{\rightarrow\sqrt{\gamma_a}\hat{d}_{in}}, \quad (2.65)$$

where $\Delta = \omega - \omega_a$ is the optical detuning from the cavity resonance. We will now assume $\hat{a}_{in}$ is white noise, which is nearly exact for optical frequencies given $\hbar\omega_a \gg k_b T$. Thus, we can make the substitution $e^{+iwt}\hat{a}_{in} \rightarrow \hat{d}_{in}$, and $\hat{d}_{in}$ will represent the ground state fluctuations in the optical field (this approximation is exact if the optical field remains in a coherent state, but in practice it will be slightly modified). Furthermore we will choose A such that the constant terms are removed from the equation of motion, resulting in a linear equation for the motion of $\hat{d}$:

$$A \rightarrow -\left(i\frac{\gamma_a}{2}+\Delta\right)\bar{a} \quad (2.66)$$

$$\dot{\hat{d}} \approx i\Delta\hat{d} + i\alpha(\hat{c}+\hat{c}^\dagger) - \frac{\gamma_a}{2}\hat{d} - \sqrt{\gamma_a}\hat{d}_{in} \quad (2.67)$$

$$\alpha \equiv \bar{a}g \quad (2.68)$$

Furthermore we can write the equation of motion for $\hat{c}$:

$$\dot{\hat{c}} = -i\omega_c\hat{c} + ig\underbrace{\left(\bar{a}^*\bar{a} + \bar{a}^*\hat{d} + \hat{d}^\dagger\bar{a} + \hat{d}^\dagger\hat{d}\right)}_{\approx|\bar{a}|^2+\bar{a}^*\hat{d}+\bar{a}\hat{d}^\dagger} - \frac{\gamma_c}{2}\hat{c} - \sqrt{\gamma_c}\hat{c}_{in} \quad (2.69)$$

We will ignore the constant $|\bar{a}|^2$ term, which corresponds only to a displacement of the equilibrium position due to the mean optical field and does not otherwise affect the physics (the corresponding shift in eqn. 2.67 could be trivially corrected by an adjustment in A). This results in a linear equation of motion for $\hat{c}$:

$$\dot{\hat{c}} \approx -i\omega_c\hat{c} + i\left(\alpha^*\hat{d} + \alpha\hat{d}^\dagger\right) - \frac{\gamma_c}{2}\hat{c} - \sqrt{\gamma_c}\hat{c}_{in}. \quad (2.70)$$

Because they are both linear, eqn. 2.67 and eqn. 2.70 can now be solved in the frequency basis. We start by writing the equations of motion in matrix form:

$$\dot{\mathbb{Z}} = \begin{pmatrix} i\Delta - \frac{\gamma_a}{2} & 0 & i\alpha & i\alpha \\ 0 & -i\Delta - \frac{\gamma_a}{2} & -i\alpha & -i\alpha \\ i\alpha^* & i\alpha & -i\omega_c - \frac{\gamma_c}{2} & 0 \\ -i\alpha^* & -i\alpha & 0 & i\omega_c + \frac{\gamma_c}{2} \end{pmatrix} \mathbb{Z}' - \begin{pmatrix} \sqrt{\gamma_a}\hat{d}_{in} \\ \sqrt{\gamma_a}\hat{d}^\dagger_{in} \\ \sqrt{\gamma_c}\hat{c}_{in} \\ \sqrt{\gamma_c}\hat{c}^\dagger_{in} \end{pmatrix} \tag{2.71}$$

where we have defined the "system operator", $\mathbb{Z}$:

$$\mathbb{Z} \equiv \begin{pmatrix} \hat{d} \\ \hat{d}^\dagger \\ \hat{c} \\ \hat{c}^\dagger \end{pmatrix} \tag{2.72}$$

and $\mathbb{Z}'$ is the transpose (row form) of $\mathbb{Z}$. We use the following convention for the Fourier transform, to comply with eqn. 2.55:

$$\tilde{\hat{a}}(\Omega) = \frac{1}{\sqrt{2\pi}} \int_{-\infty}^{\infty} \mathrm{d}t\, e^{+i\Omega t} \hat{a}(t); \quad \tilde{\hat{a}}^\dagger(\Omega) = \frac{1}{\sqrt{2\pi}} \int_{-\infty}^{\infty} \mathrm{d}t\, e^{-i\Omega t} \hat{a}^\dagger(t) \tag{2.73}$$

$$\hat{a}(t) = \frac{1}{\sqrt{2\pi}} \int_{-\infty}^{\infty} \mathrm{d}\Omega\, e^{-i\Omega t} \tilde{\hat{a}}(\Omega); \quad \hat{a}^\dagger(t) = \frac{1}{\sqrt{2\pi}} \int_{-\infty}^{\infty} \mathrm{d}\Omega\, e^{+i\Omega t} \tilde{\hat{a}}^\dagger(\Omega) \tag{2.74}$$

$$\tilde{\mathbb{Z}}(\Omega) = \int_{-\infty}^{\infty} \mathrm{d}t\, e^{+i\Omega t} \mathbb{Z}(t) = \begin{pmatrix} \tilde{\hat{d}}(\Omega) \\ \tilde{\hat{d}}^\dagger(-\Omega) \\ \tilde{\hat{c}}(\Omega) \\ \tilde{\hat{c}}^\dagger(-\Omega) \end{pmatrix} \tag{2.75}$$

We can now make the substitution $\mathbb{Z} \to \tilde{\mathbb{Z}}$ and $\dot{\mathbb{Z}} \to -i\Omega\tilde{\mathbb{Z}}$, resulting in an equation that can be solved by simple linear algebra:

$$\begin{pmatrix} -\chi_c^*(\Omega) & 0 & i\alpha & i\alpha \\ 0 & -\chi_c(-\Omega) & -i\alpha^* & -i\alpha^* \\ i\alpha^* & i\alpha & -\chi_a^*(\Omega) & 0 \\ -i\alpha^* & -i\alpha & 0 & -\chi_a(-\Omega) \end{pmatrix} \tilde{\mathbb{Z}}' = \begin{pmatrix} \sqrt{\gamma_a}\tilde{\hat{d}}_{in}(\Omega) \\ \sqrt{\gamma_a}\tilde{\hat{d}}^\dagger_{in}(-\Omega) \\ \sqrt{\gamma_c}\tilde{\hat{c}}_{in}(\Omega) \\ \sqrt{\gamma_c}\tilde{\hat{c}}^\dagger_{in}(-\Omega) \end{pmatrix}, \tag{2.76}$$

where we have defined the response functions of the mechanical and optical resonance:

$$\chi_a^{-1}(\Omega) = \frac{\gamma_a}{2} - i\,(\Omega + \Delta) \tag{2.77}$$

$$\chi_c^{-1}(\Omega) = \frac{\gamma_c}{2} - i\,(\Omega - \omega_c) \tag{2.78}$$

$$\chi \equiv \chi(\Omega); \quad \chi' \equiv \chi(-\Omega) \tag{2.79}$$

The solution is given by:

$$\tilde{\mathbb{Z}} = \tilde{\mathbb{H}} \cdot \tilde{\mathbb{Z}}'_{in} \tag{2.80}$$

$$\begin{aligned} \tilde{\mathbb{H}} \;=\; & \frac{1}{1+\alpha^2\Xi_a\Xi_c} \times \\ & \begin{pmatrix} \sqrt{\gamma_a}\chi_a^*\left(|\alpha|^2\chi'_a\Xi_c - 1\right) & \alpha^2\sqrt{\gamma_a}\chi_a^*\chi'_a\Xi_c & \dots & \dots & -i\alpha\sqrt{\gamma_c}\chi_a^*\chi_c^* & -i\alpha\sqrt{\gamma_c}\chi_a^*\chi'_c \\ -\alpha^{*2}\sqrt{\gamma_a}\chi_a^*\chi'_a\Xi_c & -\sqrt{\gamma_a}\chi'_a\left(|\alpha|^2\chi_a^*\Xi_c + 1\right) & \dots & \dots & i\alpha^*\sqrt{\gamma_c}\chi_a^*\chi'_c & i\alpha^*\sqrt{\gamma_c}\chi'_a\chi'_c \\ -i\alpha^*\sqrt{\gamma_c}\chi_a^*\chi_c^* & -i\alpha\sqrt{\gamma_c}\chi_a^*\chi'_c & \dots & \dots & \sqrt{\gamma_c}\chi_c^*\left(|\alpha|^2\chi'_c\Xi_a - 1\right) & |\alpha|^2\sqrt{\gamma_c}\chi_c^*\chi'_c\Xi_a \\ i\alpha^*\sqrt{\gamma_c}\chi_a^*\chi'_c & i\alpha\sqrt{\gamma_c}\chi'_a\chi'_c & \dots & \dots & -|\alpha|^2\sqrt{\gamma_c}\chi_c^*\chi'_c\Xi_a & -\sqrt{\gamma_c}\chi'_c\left(|\alpha|^2\chi_c^*\Xi_a + 1\right) \end{pmatrix}, \end{aligned} \tag{2.81}$$

where we have defined Ξ:

$$\Xi_i(\Omega) = \Xi_i \equiv \chi_i^*(\Omega) - \chi_i(-\Omega) \tag{2.82}$$

and i refers to a or c. We can calculate the thermal spectrum of the cantilever's motion from the frequency spectrum of the system operators.

$$S_{cc}(\Omega) = \int_{-\infty}^{\infty} \mathrm{d}t\, e^{-i\Omega t} \left\langle \hat{c}^\dagger(t)\hat{c}(0)\right\rangle \tag{2.83}$$

$$= \frac{1}{2\pi}\iiint_{-\infty}^{\infty} \mathrm{d}t\;\; \mathrm{d}\omega'\;\; \mathrm{d}\omega''\, e^{i(\omega'-\Omega)t}\tilde{\hat{c}}^\dagger(\omega')\tilde{\hat{c}}(\omega'') \tag{2.84}$$

$$= \int_{-\infty}^{\infty} \mathrm{d}\omega''\, \tilde{\hat{c}}^\dagger(\Omega)\tilde{\hat{c}}(-\omega''), \tag{2.85}$$

where we note that the mean phonon number of the system is given by:

$$\bar{n}_c = \int_{-\infty}^{\infty} \mathrm{d}\Omega \, S_{cc}(\Omega). \tag{2.86}$$

We can now plug in our solution in terms of the matrix elements of $\mathbb{H}$.

$$\begin{aligned} S_{cc}(\Omega) &= \left\langle \sum_{\hat{z}=\mathbb{Z}(-\Omega)} \tilde{\mathbb{H}}_{\hat{c}^\dagger,\hat{z}}(-\Omega)\tilde{\hat{z}}_{in} \int_{-\infty}^{\infty} \mathrm{d}\omega'' \sum_{\hat{z}'=\mathbb{Z}(\omega'')} \tilde{\mathbb{H}}_{\hat{c},\hat{z}}(\omega'')\tilde{\hat{z}}'_{in} \right\rangle & (2.87) \\ &= \sum_{\hat{z}=\mathbb{Z}} \tilde{\mathbb{H}}^{-}_{\hat{c}^\dagger,\hat{z}} \tilde{\mathbb{H}}_{\hat{c},\hat{z}^\dagger} \left\langle \tilde{\hat{z}}_{in}\tilde{\hat{z}}^\dagger_{in} \right\rangle \\ &= \tilde{\mathbb{H}}^{-}_{\hat{c}^\dagger,\hat{d}} \tilde{\mathbb{H}}_{\hat{c},\hat{d}^\dagger} + \bar{n}_{th}\, \tilde{\mathbb{H}}^{-}_{\hat{c}^\dagger,\hat{c}^\dagger} \tilde{\mathbb{H}}_{\hat{c},\hat{c}} + (\bar{n}_{th}+1)\tilde{\mathbb{H}}^{-}_{\hat{c}^\dagger,\hat{c}} \tilde{\mathbb{H}}_{\hat{c},\hat{c}^\dagger}, & (2.88) \end{aligned}$$

where we have assumed that the optical field is coupled to a ground state bath, $\left\langle \tilde{\hat{d}}^\dagger_{in}\tilde{\hat{d}}_{in} \right\rangle = 0$, and the mechanical motion is coupled to a thermal bath, $\left\langle \tilde{\hat{c}}^\dagger_{in}\tilde{\hat{c}}_{in} \right\rangle = \bar{n}_{th}$. In the interest of notational compactness we have defined:

$$\tilde{\mathbb{H}} \equiv \tilde{\mathbb{H}}(+\Omega); \quad \tilde{\mathbb{H}}^{-} \equiv \tilde{\mathbb{H}}(-\Omega). \tag{2.89}$$

Using the solutions of the operators above, we find:

$$\begin{aligned} S_{cc}(\Omega) &= \underbrace{\frac{|\chi_c|^2}{\left|1+|\alpha|^2\,\Xi_a(\Omega)\Xi_c(\Omega)\right|^2}}_{\text{modified mechanical response}} \times \Bigg[\underbrace{\gamma_a\,|\alpha\chi'_a|^2}_{\text{photon shot noise}} + & (2.90) \\ &\underbrace{\bar{n}_{th}\gamma_c\left|1-|\alpha|^2\,\chi'_c\Xi_a(\Omega)\right|^2}_{\text{main thermal excitation}} + \underbrace{(\bar{n}_{th}+1)\,\gamma_c\left||\alpha|^2\,\chi'_c\Xi_a(\Omega)\right|^2}_{\text{mechanical zero point fluctuations}} \Bigg], \end{aligned}$$

where the original of the different terms can be clearly identified from their origin in eqn. 2.90. A plot of the integrated spectral density is shown in fig. 2.8. Despite the apparent complexity, this result is functionally similar to eqn. 2.45 for weak feedback. As the input pump power (α) is increased the shot noise back action becomes larger than the thermal input noise of the mechanical mode, limiting the maximum degree of feedback cooling. By computing the total spectral density, it

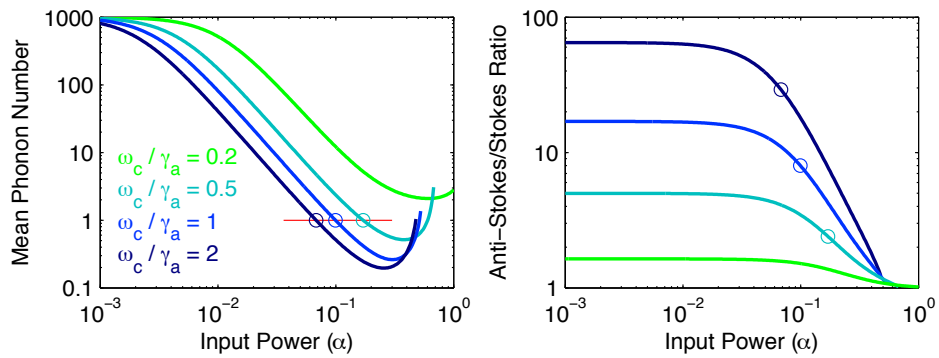

Figure 2.8: The effects of optical cooling as a function of input pump power and the ratio between the mechanical frequency, ω_c, and the cavity decay rate, γ_a. The input optical field strength is given in terms of a dimensionless power, $\alpha = \sqrt{\bar{n}_a} g$ where $\bar{n}_a$ is the mean number of photons in the optical cavity. The pump laser is detuned from the cavity resonance by $\Delta = -\omega_c$ and the initial thermal excitation of the mechanical resonator is given by $n_{th} = 1000$. **Left:** Mean phonon number, $\bar{n}_c$. **Right:** Anti-Stokes/Stokes ratio.

can be seen that it is possible to achieve ground state cooling, $\bar{n}_c \lesssim 1$, only when the cavity is in the sideband resolved regime, $\gamma_a \lesssim \omega_c$.

In a similar fashion we can look at the optical output spectrum from the cavity:

$$\hat{a}_{out} = a_{in} + \sqrt{\gamma_a}\hat{a} \tag{2.91}$$

$$S_{aa,out}(\Omega) = \int_{-\infty}^{\infty} \mathrm{d}t e^{-i\Omega t} \left\langle \hat{a}_{out}^{\dagger}(t)\hat{a}_{out}(0) \right\rangle \tag{2.92}$$

$$\begin{aligned} S_{aa,out} &= \gamma_a \Big[2\pi \left|\bar{a}\right|^2 \delta(\Omega) + \tilde{\mathbb{H}}^{-}_{\hat{d}^\dagger,\hat{d}} \tilde{\mathbb{H}}_{\hat{d},\hat{d}^\dagger} + \\ &\quad \bar{n}_{th} \tilde{\mathbb{H}}^{-}_{\hat{d}^\dagger,\hat{c}^\dagger} \tilde{\mathbb{H}}_{\hat{d},\hat{c}} + (\bar{n}_{th}+1) \tilde{\mathbb{H}}^{-}_{\hat{d}^\dagger,\hat{c}} \tilde{\mathbb{H}}_{\hat{d},\hat{c}^\dagger} \Big] \end{aligned} \tag{2.93}$$

$$\begin{aligned} \frac{S_{aa,out}(\Omega+\omega_a)}{\gamma_a} &= 2\pi \left|\bar{a}\right|^2 \delta(\Omega) + \\ &\quad \frac{1}{\left|1+\left|\alpha\right|^2 \Xi_a \Xi_c\right|^2} \times \Big[\underbrace{\gamma_a \left|\alpha^2 \chi_a \chi_a' \Xi_c\right|^2}_{\text{intensity fluctuations}} + \\ &\quad \underbrace{\bar{n}_{th}\gamma_c \left|\alpha \chi_a \chi_c\right|^2}_{\text{anti-Stokes (cooling)}} + \underbrace{(\bar{n}_{th}+1)\,\gamma_c \left|\alpha \chi_a \chi_c'\right|^2}_{\text{Stokes (heating)}} \Big] \end{aligned} \tag{2.94}$$

The Stokes sidebands are caused by the energy exchange between the optical field and the mechanical resonator. When there are more photons in the anti-Stokes band than the Stokes band, there is a net transfer of energy from the mechanical to the optical degree of freedom. This will happen if the system is detuned so that the anti-Stokes band is resonant with the optical cavity ($\Delta = -\omega_c$), resulting in optical cooling. For opposite detuning, there is a net transfer of energy to the mechanical mode, resulting in heating.

In the case that the system is cooled near the ground state, it becomes impossible to remove more energy from the system. This will suppress the anti-Stokes band relative to the Stokes band, resulting in a clear signal that the system is cooled near the ground state (fig. 2.8). It can be seen that when the mean phonon number is of order 1, the ratio of the Stokes sidebands is reduced to half of the low field ($\alpha \ll 1$) value. This is a truly quantum signature; for a classical system reducing the amplitude of the thermal fluctuations reduces both sidebands equally. Furthermore, it should be possible to measure the sideband amplitudes in a real experiment using a heterodyne detection scheme. This gives passive optical cooling a significant advantage over active optical cooling, which does not provide

a clear method for determining when the ground state has been reached.

Although eqn. 2.90 and eqn. 2.94 are exact solutions of eqn. 2.67 and eqn. 2.70, we must be aware that they are based on an approximation that may not be appropriate for realistic devices. In particular, if $g \sim \omega_c$ and the mean photon number, $\bar{a}$, is of order 1, the approximations required to linearize the system break down. Although current devices are far from approaching this regime, an optomechanical system appropriate for a superposition-type experiment has exactly these requirements. In this case, the system is highly nonlinear, and a numerical simulation is required to consider the full quantum dynamics of the system.

Chapter 3

Experimental Requirements

All proposals for observing quantum effects in micro-optomechanical systems have extremely challenging experimental requirements. Here we briefly review these requirements with respect to real experimental limitations. Although we will use the superposition experiment as a specific example, these requirements generally apply to any experiment in which one wants to observe quantum effects in a optomechanical system.

To evaluate the practicality of the requirements, we will consider an ideal micro-optomechanical system with one big curved mirror and one tiny mirror on a micromechanical element:

$$\begin{aligned} L &\gtrsim 1\text{cm} \\ r_{big} &= \tfrac{L}{5} \\ r_{tiny} &= 5\ \mu\text{m} \\ \lambda &= 500\ \text{nm} \\ m &= 10^{-12}\ \text{kg} \\ \omega_c &= 2\pi \times 500\ \text{Hz} \\ x_0 &= 130\ \text{fm}, \end{aligned} \tag{3.1}$$

where L is the cavity length, r_{big} and r_{tiny} are the radii of the cavity end mirrors and all other quantities are as previously defined. The exact length of the cavity

is not important, although we assume it is in the far-field regime. The size of the tiny mirror is chosen so that the diffraction limited optical quality is sufficiently high (see §6 for details; for this system $\alpha = 2.5$, giving a diffraction limited finesse of more than 10^6). As we will show, it is theoretically possible to construct a system with these parameters from a dielectric mirror on a thin silicon cantilever.

3.1 Optical Quality

For a single photon experiment, the optomechanical interaction must be strong enough that a single photon can create or destroy a single phonon in the mechanical mode. It follows that the decay rate of the optical cavity must be less than the optomechanical interaction constant (which is also expressed as a rate):

$$\gamma_a < |g|. \tag{3.2}$$

We will most commonly use optical finesse, F, as a measure of optical cavity quality. The finesse is the ratio of the cavity linewidth to the free spectral range of the cavity; in the high finesse ($F \gg 1$) limit, it is 2π times the mean number of round trips a photon makes in the cavity. For a simple optical cavity with one movable mirror, the required finesse is given by:

$$F > \frac{\lambda}{2x_0}, \tag{3.3}$$

where $x_0 = \sqrt{\frac{\hbar}{2m\omega_c}}$ is the ground state wavepacket size, as before, and we have made use of the fact that the optical decay rate is given by $\gamma_a = \pi c/LF$. Similarly for a gradient force system:

$$Q_{opt} = \frac{\gamma_a}{\omega_a} > \frac{\omega_a}{x_0}\left|\frac{d\omega_a}{dx}\right|^{-1} = \frac{\lambda}{x_0}\left|\frac{d\lambda}{dx}\right|^{-1}, \tag{3.4}$$

where we note that typically $\left|\frac{d\lambda}{dx}\right| \sim 1$ for nano-photonic cavities (for example: [27]). Intuitively, these conditions are equivalent to the requirement that a single

photon is able to resolve the ground state of the mechanical mode. For experiments like optical cooling, in which the optical cavity is pumped by a coherent state with $\bar{n}$ photons, the requirement is reduced to:

$$F \geq \frac{\lambda}{2x_0\sqrt{\bar{n}}}, \tag{3.5}$$

which can be seen either from §2.3.2 or by observing that the sensitivity of an interferometer increases like $\sqrt{\bar{n}}$. Unfortunately this enhancement can only be used for a limited class of experiments, not including the superposition experiment as originally proposed. Due to the strict optical requirements, there is a great deal of interest in deriving equivalent experiments capable of taking advantage of this enhanced sensitivity. Although there has been some progress recently [63, 64], the interpretation of these proposals as demonstrating quantum effects has not received the same degree of scrutiny.

The required finesse for our ideal system, assuming the single photon requirement, is $F > 2\times10^6$. This is at the limit of what can be obtained in conventionally sized optical cavities [65, 66], even with these cavities operating at slightly longer wavelengths, $\lambda \gtrsim 800$ nm. Unfortunately, the required finesse scales like $\lambda^{5/2}$ with all other parameters kept constant (assuming the mirror mass dominates the mechanical resonator, m scales like λ^3, as we shall show below), so the experiment would likely need to be operated at somewhat shorter wavelengths.

A gradient force or "membrane in the middle" approach could reduce the mass of the mechanical system by perhaps an order of magnitude, but in any case a λ^3 mass scaling can not be avoided. Additionally, obtaining a sufficiently low mechanical frequency without a large mass is problematic in these alternative systems.

Improving any of the parameters listed in eqn. 3.1 in order to reduce the optical requirements poses complications:

- The mechanical mass cannot be reduced below the mass of the mirror, although this could be reduced by increasing the numerical aperture of the

optical system.

- The numerical aperture of the system, $\varphi = r_{big}/L$, is limited by the practicalities of super-polishing mirrors with relatively small radii of curvature*. If improvement in mirror polishing was made beyond $\varphi > 1/5$, the penetration depth of the mirror would start to limit the optical quality.

- The frequency of the mechanical resonator could be reduced, although at 500 Hz isolation from background vibration is already a serious concern. Additionally it is difficult to do this without increasing the mass (and consequently x_0) of the system.

A plot of equivalent optical finesse versus ground state wavepacket size is shown for a variety of experimental devices in fig. 3.1. In general, no devices have yet been demonstrated for which $g \gtrsim \gamma_a$, although in one case the strong coupling regime $\sqrt{\bar{n}}g \gtrsim \gamma_a$ has been observed at room temperature by using a relatively strong optical field [72].

3.1.1 DBR Mirrors

To achieve finesses on the order of 10^6, the loss of each mirror needs to be at most several parts per million. Metal mirrors have losses typically in the range of 1%, making distributed Bragg reflectors (DBR or dielectric mirrors) the only practical option. These mirrors are composed of alternating layers of high and low index of refraction materials; the most commonly used materials for very high reflectivity mirrors are Ta_2O_5 and SiO_2. If each layer is $\lambda/4n$ thick, the light reflected from the material interfaces in the dielectric stack interferes constructively, enhancing the reflectivity. For a DBR stack with N layers each of the high and low index material, the peak reflectivity can be determined from the

* In particular, the wavefront error of the mirror becomes a serious concern. See §6.3.3 for the theory of wavefront error and §7.2.2 for measurements of real mirrors.

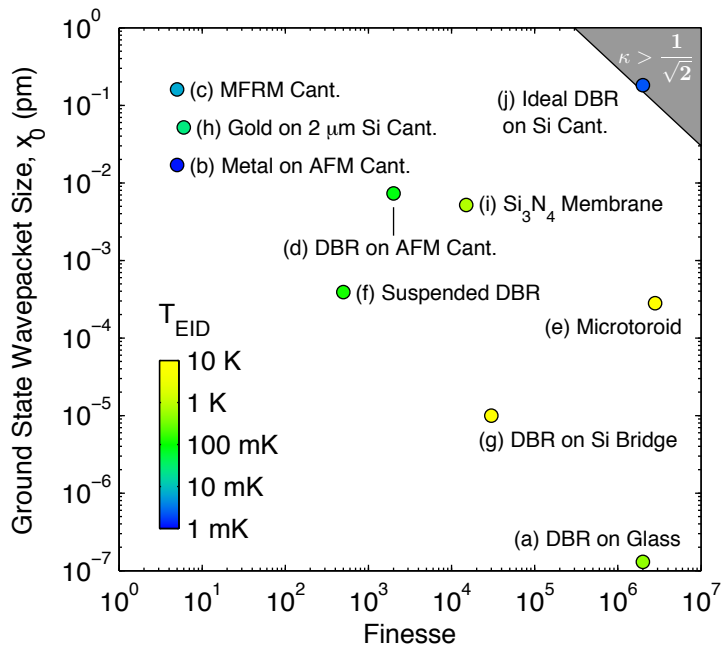

Figure 3.1: A comparison of optomechanical devices, showing the finesse and size of the ground state wavepacket, $x_0 = \sqrt{\hbar/m\omega_c}$. All points apart from (j) are based on published results. The shaded area in the upper right corresponds to $\kappa = 1/\sqrt{2}$ for visible light ($\lambda = 600$ nm). The color of each point corresponds to the characteristic environmentally induced decoherence temperature, $T_{EID} = \hbar\omega_c Q/k_b$.

(a) A dielectric with $F = 2 \times 10^6$ deposited on a cm size mirror.
(b) Metal deposited on a conventional AFM cantilever (e.g. [60]).
(c) A thin silicon cantilever used in magnetic force resonance microscopy[67].
(d) A focused ion beam milled DBR mirror glued to a commercial AFM cantilever [68] (see also §4).
(e) Microtoroidal resonator [57].
(f) Resonator made of a suspended DBR bridge [69].
(g) DBR deposited on a silicon bridge resonator [51].
(h) A 2 μm silicon resonator with gold deposited on it [70].
(i) Commercial Si_3N_4 membrane in a high finesse optical cavity [71].
(j) Our ideal device, eqn. 3.1, with $F = 2 \times 10^6$. This is essentially a combination of the mechanical properties of (c) with the optical properties of (a).

thin film matrix method [28]:

$$R = \left[\frac{1 - n_s \left(\frac{n1}{n2}\right)^{2N}}{1 + n_s \left(\frac{n1}{n2}\right)^{2N}}\right]^2, \tag{3.6}$$

where n_s, n_1 and n_2 are the indices of refraction of the substrate, high index material and low index material, respectively, and the mirror is assumed to be in vacuum ($n_0 = 1$). This can be reformulated in terms of a mirror transmission:

$$\begin{aligned} T &= \frac{4n_s \left(\frac{n1}{n2}\right)^{2N}}{\left(1 + n_s \left(\frac{n1}{n2}\right)^{2N}\right)^2} \\ &\cong \frac{4}{ns}\left(\frac{n2}{n1}\right)^{2N} \qquad (\text{for } T \ll 1). \end{aligned} \tag{3.7}$$

If an optical cavity is made of two identical mirrors, and limited only by the transmission of these mirrors, the finesse is given by $F_r = \pi/T$, assuming $T \ll 1$. In terms of the DBR mirror properties, this is:

$$F_r \cong \frac{\pi ns}{4}\left(\frac{n1}{n2}\right)^{2N} \tag{3.8}$$

$$\sim 2.10^N, \tag{3.9}$$

where in the last equation we have assumed $n_1 = 2.10$ and $n_2 = 1.45$, corresponding to Ta_2O_5 and SiO_2, and ignored the effect of the substrate (or if you prefer, $n_s \sim 4/\pi$). An ultra-high reflectivity mirror will generally have around 20 layers of each of SiO_2 and Ta_2O_5, giving a maximum finesse of $F_R \sim 3 \times 10^6$. For even the best real mirrors, the loss intrinsic to the mirror materials and the scattering due to substrate roughness are on the order of parts per million, so adding more layers to the DBR does not increase the finesse significantly beyond this point.

The total mass of a DBR mirror can be calculated from the properties of the

dielectric layers it is made out of:

$$m_{mirror} = \pi N \lambda^3 \left(\frac{r_a}{\lambda}\right)^2 \left[\frac{\rho_1}{4n_1} + \frac{\rho_2}{4n_2}\right] \tag{3.10}$$

$$= \frac{N\lambda^3\alpha^4}{4\pi\varphi^2}\left[\frac{\rho_1}{n_1} + \frac{\rho_2}{n_2}\right], \tag{3.11}$$

where on the second line we have used the formalism of §6 to rewrite the mirror size in terms of the numerical aperture of the large mirror; α is the ratio of mode to mirror size, for ultra-high finesse cavities ($F \gtrsim 10^6$) we require: $\alpha \gtrsim 2.2$. The density of SiO_2 and Ta_2O_5 is $\rho = 2.6$ and 8.2 g m^{-3} respectively[†]. This results in $m \cong 10^{-12}$ kg for the parameters given in eqn. 3.1 with $N = 20$.

3.1.2 Cavity Alignment

Because most optomechanical systems are composed of an optical cavity with one microscopic end, alignment is far more critical than in cavities with two conventional mirrors. If we consider the location of big mirror to be fixed, the cavity alignment has six degrees of freedom, corresponding to translation and rotation of the tiny mirror. Assuming both mirrors are circular (or at least have radial symmetry), there are five non-trivial degrees of freedom; two are pictured in fig. 3.2 and another two are essentially the same but along a different axis.

First, consider transverse (perpendicular to the cavity axis) displacements of the tiny mirror. At the location of the tiny mirror, the intensity profile of a cavity mode should always have 180° rotational symmetry about the center of radius of

[†] In practice, Ta_2O_5 may not be the ideal high index material, due to its extremely high density and relatively moderate index. For example, TiO_2 has higher index ($n \sim 2.5$) and lower density ($\rho = 4.2$ g m^{-3}) than Ta_2O_5, but it is not generally used in ultra high reflectivity mirrors as it tends to have higher optical loss. As a compromise, a mirror could be manufactured with the top several layers composed of Ta_2O_5 and the rest made of TiO_2, potentially reducing the mass by about half. Further reduction in mass can be achieved using amorphous silicon ($n \sim 3.5$, $\rho = 2.4$ g m^{-3}), but the optical loss is only acceptably low if the optical energy is below the band gap, or $\lambda \gtrsim 1.2\mu$m. Although we have not attempted to fabricate systems with this type of mirror, it may be worthwhile to do so in the future.

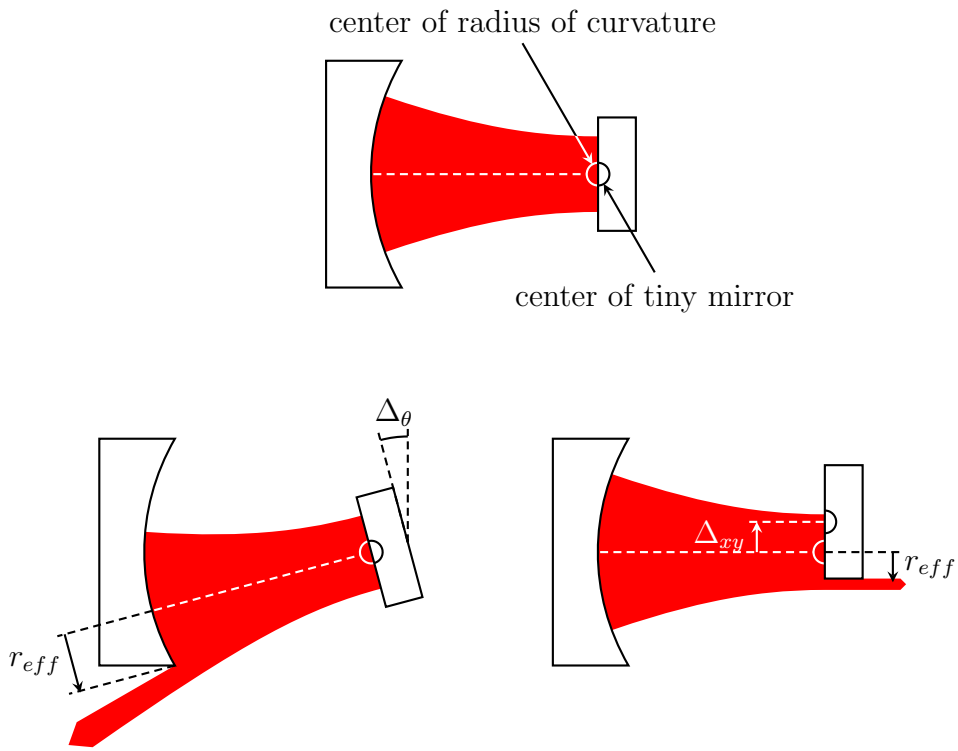

Figure 3.2: Possible cavity misalignments, and the respective modification of the cavity mode. Length (defocusing) errors are not shown. **Top:** A perfectly aligned cavity. For clarity the tiny mirror is shown at a much larger scale than would be the case for a real cavity. **Bottom-left:** Angular misalignment of the tiny mirror, with the reduced effective radius of the big mirror indicated. **Bottom-left:** Translational misalignment of the tiny mirror, showing the reduced effective radius of the tiny mirror.

curvature[‡], meaning that the cavity mode can not adjust to translations of the tiny mirror. In this case it is clear that we require:

$$\Delta_{xy} \ll r_{tiny}, \tag{3.12}$$

where we have assumed the cavity is diffraction limited (if it is not, there is some extra "slop" built into the mirror, but this is undesirable from the perspective of minimizing mirror mass). The required accuracy is on the order of a micron, which is well within the range of conventional nano-positioning systems.

Error in the longitudinal position of the tiny mirror, or length of the cavity, causes the light to defocus as it circulates in the cavity. Although there is no simple way to estimate the resulting loss, it is possible to calculate with a mode mixing approach (see §6.3.1). If we wish to reach a finesse of 10^6, the cavity length error must be less than:

$$\Delta_z \lesssim 10^{-4} z_0, \tag{3.13}$$

where $z_0 = \pi w_0^2/\lambda$ is the Rayleigh range. For the system described by eqn. 3.1, the Rayleigh range is $z_0 = 25\ \mu$m, requiring a length accuracy of $\Delta_z \lesssim 2.5$ nm. This is requirement is quite strict, especially if the cavity length is several cm, although it should be possible with careful system design; possible methods for achieving this are discussed in §7.2.3.

Finally, the accuracy requirements for rotations of the tiny mirror can be estimated in a similar manner to the transverse displacements above. At the location of the big mirror, the field intensity must be symmetric about a line normal to the surface of the tiny mirror and so:

$$\Delta_\theta \ll \frac{r_{big}}{L} = \varphi. \tag{3.14}$$

[‡] From the principles of classical optics, the mode profile on the small mirror is mirrored about the center of radius of curvature of the large mirror on each reflection. As a result, all cavity eigenmodes must have a intensity ($|E|^2$) profile that has 180° rotational symmetry at the location of the small mirror, and hence the mode center can not move to adapt to translations of the small mirror. Following the formalism in §6, this effect can equivalently be seen as a consequence of the different Gouy shift for even and odd modes of a long cavity.

Due to the large size of the big mirror, this required accuracy is only on the order of several degrees and is considerably easier to meet than the other degrees of freedom.

3.1.3 Rare Events and the Superposition Experiment

The requirement for the optical quality above, eqn. 3.3, is related but not identical to the requirement for putting a cantilever in a distinguishable state. As shown in §2.2.1, putting the cantilever in a distinguishable quantum state requires $g \sim \omega_c$; using eqn. 2.20 this can be rewritten as:

$$N \gtrsim \frac{\lambda}{2x_0}, \tag{3.15}$$

where N is the number of photon round trips per mechanical period. Although this form is closely related to eqn. 3.3, we note that the number of round trips per mechanical period is not necessarily related to the finesse.

For the superposition experiment, we are primarily concerned with the number of photons that leave the cavity during the interference revival window. If we inject a single photon, it can easily be shown that the probability that it leaves during the interference revival window is:

$$P_{rw} = \frac{\gamma_a e^{-2\pi \frac{\gamma_a}{\omega_c}}}{\omega_c \sqrt{2\bar{n}+1}}, \tag{3.16}$$

where we have assumed that the width of the revival window is:
$t_{rw} = \left(\omega_c \sqrt{2\bar{n}+1}\right)^{-1}$.

In a real experiment, one would choose the cavity length, L, to obtain the required value of the optomechanical coupling, κ. Accordingly, we can rewrite the revival window probability as:

$$P_{rw} = \kappa \frac{F_0}{F} \frac{e^{-2\pi\kappa \frac{F_0}{F}}}{\sqrt{2\bar{n}+1}}, \tag{3.17}$$

where we have defined $F_0 = 2x_0/\lambda$ to illustrate the connection between eqn. 3.3 and eqn. 3.15. For $\kappa = 1$, the most photons are observed in the revival window when $F = 2\pi F_0$, in which case the mean time a photon spends in the cavity is equal to the mechanical period. It is possible to operate the experiment at a lower finesse, but in this case one will only rarely observe a photon in the revival window. Despite this, the difficulty of achieving the required high finesse may make this unavoidable. In this case, one needs to ensure that the count rate in the revival window is kept above the dark count rate of the photon detectors (see §3.4).

3.2 Quantum Coherence and Mechanical Loss

To measure quantum effects, the mechanical resonator must have a quantum coherence time comparable to the length of the desired measurement. (Or at least, the coherence time of known mechanisms should be comparable to the measurement time; potential decoherence mechanisms of the type discussed in §2.2.5 would ideally be *shorter* than the measurement time, so that they could be probed.) From an experimental point of view, this is most easily expressed in terms of the mechanical quality factor, Q:

$$Q \gtrsim \bar{n}_{th} \cong \frac{k_b T_B}{\hbar \omega_c}, \tag{3.18}$$

where T_B is the temperature of the thermal bath to which the resonator is connected. Optical cooling does *not* ease this constraint (see §2.3); the easiest way to see this is that optical cooling effectively reduces both Q_{eff} and T_{eff} by the same amount[§]. In practice, cooling actually introduces back action noise, which

[§] To circumvent this, you could imagine doing an experiment where you cool to the ground state and then quickly turn off the cooling during the superposition measurement period. Unfortunately, the decoherence is caused by new phonons coupling in from the thermal bath; the rate at which this happens is unaffected by optical cooling and the same decoherence rate should be observed in this case.

can become comparable to or larger than the thermal noise if the effective gain is too high (e.g. §2.3.2), actually reducing the coherence time.

For our ideal system, we find the ground state equivalent temperature is $\hbar\omega_c/k_b = 25$ nK. For single crystal silicon resonators at around 1 kHz, the mechanical quality factor is about 10^5 at sufficiently low pressures [67], requiring a base temperature of $T_{EID} = 2.5$ mK. This value could potentially be increased by as much as two orders of magnitude using tensed Si_3N_4 resonators [71], although as we shall see later, it is difficult to reduce the frequency without increasing the mass (T_{EID} is shown for a number of optomechanical devices in fig. 3.1). Temperatures of less than 1 mK are experimentally achievable with a nuclear adiabatic demagnetization stage, although the use of such a stage to cool a mechanical resonator has yet to be attempted. Much lower temperatures are theoretically possible, but thermally anchoring the sample to the stage will likely limit the cooling – see §7.2.4.

If the quality factor or base frequency can be increased by an order of magnitude, the required temperature increases to 25 mK, which can be realized with a standard dilution refrigerator. Effective temperatures of 100 mK have already been measured in MFRM experiments, limited by optical absorption from the interferometric readout [67]. Absorption is likely to be less of a problem for ultra-high finesse micro-optomechanical systems, which already require lower levels of light and intrinsic absorption.

3.3 Background Pressure

Background gasses in the experiment cause damping (and hence information loss) of the resonator, affecting the quantum coherence of the system. Because of the extremely high intrinsic quality factors of many optomechanical systems, this damping can be relevant even in vacuum conditions.

To calculate the effect of this damping, we need to know the relevant flow regime for the gas molecules. This is usually characterized with the Knudsen number, or the ratio of mean free path of gas molecules to characteristic object dimensions:

$$Kn = \frac{\ell}{L_{char}} \tag{3.19}$$

$$\ell = \frac{k_b T}{\sqrt{2}\pi a^2 P}, \tag{3.20}$$

where ℓ is the mean free path, a is the effective molecule diameter, P is the gas pressure, and L_{char} is the characteristic length of the optomechanical system. For a relatively poor vacuum of $P = 1$ mBar, the mean free path at room temperature is $\ell \sim 100\mu$m if we assume $a \sim 3$ Å; this mean free path is comparable to the typical dimensions of our mechanical resonators. Because we are typically working at much lower pressures, we will henceforth assume we are always in the free-molecular regime, $Kn \gg 1$. This allows us to calculate damping without a full fluid dynamics simulation.

In this regime, the pressure difference between two sides of a flat object moving at a velocity v normal to its surface is given by [73]:

$$\Delta P = 4\sqrt{\frac{2}{\pi}} v P \sqrt{\frac{m_m}{k_b T}} \tag{3.21}$$

$$= \frac{v}{v_d} P$$

$$v_d = \frac{1}{4}\sqrt{\frac{\pi k_b T}{2 m_m}}, \tag{3.22}$$

where m_m is the mass of a single gas molecule and v_d is an effective damping velocity, which is the RMS (root mean squared) velocity of the gas molecules times a geometric factor. (At room temperature, $v_d = 94$ m s^{-1} for N_2.)

We now assume our resonator is nearly planar and only consider deformation normal to the planar surface[¶]. In the absence of external forces, we can repre-

[¶] In practice, most optomechanical devices have a small thickness to length ratio, and so the "thin beam" approximation we are making should be acceptably accurate.

sent the deformation at some point along the plane r as a summation over the vibrational modes of the resonator:

$$z(\vec{r},t) = \sum_j \mathrm{Re}\left[X_j \Phi_j(\vec{r}) e^{i\omega_j t}\right], \tag{3.23}$$

where X_j, ω_j and Φ_j are the corresponding complex excitation amplitude, frequency and dimensionless mode profile of mode j (see §A for specific geometries). From eqn. 3.21, we find the total energy loss:

$$\dot{E}(t) = \frac{P}{v_d} \int \dot{z}^2 \, d\vec{r} \tag{3.24}$$

$$\Rightarrow \bar{\dot{E}}_j = \frac{\omega_j^2 X_j^2 P}{2 v_d} \underbrace{\int \Phi_j^2 \, d\vec{r}}_{A_j}, \tag{3.25}$$

where the integral is assumed to be taken over the resonator surface and A_j is the effective surface area of mode j (typically A_j is one fourth to one half the actual surface area). In the second equation we have made use of the fact that the modes are orthogonal to consider only the energy loss from a single mode. From the total energy in a given mode we can calculate the mechanical Q factor:

$$E_j = \frac{1}{2} m_j \omega_j^2 X_j^2 \tag{3.26}$$

$$Q_{P,j} = \frac{\omega_j E_j}{\bar{\dot{E}}_j} = \frac{v_d}{P} \frac{m_j \omega_j}{A_j}, \tag{3.27}$$

where we have assumed we are in the good resonator limit ($Q \gg 1$). If our resonator has a uniform thickness, t, and density, ρ:

$$Q_{P,j} = \frac{v_d}{P} \omega_j t \rho, \tag{3.28}$$

which agrees with the theoretical calculations of Li et al. [74], who also found it to be in good agreement with numerical simulations and experimental results in the regime $Kn \gg 1$. This also agrees with our results for resonators which are in the free-molecular regime and with a Q lower than the intrinsic (material

limited) value, e.g. §4.3. Note that in the regime $Kn \lesssim 1$, damping calculations require a full fluid dynamics simulation, although in general the Q is expected to be higher than found in eqn. 3.27 (we also observe this in real experiments). To consider amount of damping for our ideal resonator, we need to choose a resonator geometry. Consider a cantilever of 200 nm thickness, 5 μm width and 500 μm length. From eqn. A.9, we find this resonator has the right frequency ($\omega = 2\pi \times 500$ Hz) if it is made of single crystal silicon ($E = 250$ GPa) and a mirror of mass 10^{-12} kg is placed on the tip. Cantilevers of appropriate geometries have been fabricated for MFRM experiments [75]. From eqn. 3.27 and eqn. A.10, we find:

$$Q_p \cong 5\sqrt{\frac{T}{300\text{K}}}\left(\frac{1\text{ mbar}}{P}\right). \tag{3.29}$$

Assuming we wish to reach the intrinsic quality factor of $Q \sim 10^5$, the required pressure at room temperature is $P < 5 \times 10^{-5}$ mBar, which is easily achievable with conventional vacuum technology. Although the requirement appears more difficult at low temperatures, in general the ambient pressure is reduced in cryogenic systems. If we assume that the number of gas molecules in the system is constant, it follows from the ideal gas law that $P \propto T$; thus it should actually be much easier to minimize the gas damping in cryogenic systems.

3.4 Single Photon Detectors

The superposition experiment is a single photon experiment, and hence requires single photon detectors. Unfortunately, the most commonly used single photon detectors, silicon avalanche photodiodes (APDs), are not well suited for this type of experiment. The most important requirement is low dark-counts; although one might naively suspect the output arms have a maximum count rate of order $\omega_c/2\pi \sim 500$ Hz, under realistic conditions it is at least a factor of 30 lower, possibly much more.

Due to the difficulty of creating a true single-photon state, many "single-photon" experiments are done using a classical light state attenuated so the mean number of photons per run, $\langle n \rangle$, is much less than 1[‖]. In this way most experimental runs either have 0 or 1 photon, and since the 0-photon state produces no counts it is automatically excluded from the results. This leaves one with an effective 1-photon state via "post-selection." The maximum photon rate we can use is then limited by the 2-photon probability, which we need to be small to avoid corrupting the results. Although in principle one could exclude these effects using photon-number resolving detectors and more sophisticated post-selection, this is only effective if the system has very low loss. Otherwise lossy 2-photon events will appear as 1-photon events, contaminating the data. Assuming the input light is in a coherent state, the photon number probability is Poissonian:

$$P(n) = \frac{\langle n \rangle^n e^{-\langle n \rangle}}{n!}. \tag{3.30}$$

Typically one works in the regime $P(1) \sim 10\%$, in which case $P(2) \sim 0.5\%$, which is good enough for the experiments considered here.

We must also consider the fraction of photons remaining in the revival window, as discussed in §3.1. At the peak of the first interference revival ($t = 2\pi/\omega_c$), the total count rate is then given by:

$$C_r w = \frac{\omega_c}{2\pi} \times P(1) \times \kappa \frac{F_0}{F} e^{-2\pi\kappa \frac{F_0}{F}}. \tag{3.31}$$

For the ideal system with $P(1) = 0.1$, $F = 2\pi F_0$ and $\kappa = 1$, this count rate is only 50 Hz, which is comparable to or even less than the dark count rate in the best silicon APDs. With a somewhat more realistic finesse value

‖ In fact, for a superposition type experiment, it would be no help even if you could start with a perfect single photon state on the input. This is because the input state must be in the form of a short pulse (required for the visibility timing) and hence will always be bandwidth mismatched from the cavity. As a result most of the photons bounce off the input mirror and only a small fraction ($\sim 1/F$) enter one of the two optical cavities. For this type of experiment it is this small fraction that must be of order 1, not the total number of input photons.

of $F = F_0$ this gives a peak count rate of only 0.1 Hz, ruling out conventional APDs completely. Fortunately several alternative single photon detectors based on superconducting transitions have been recently developed. For our purposes, the best type of detector is called a transition edge sensor (TES), which is essentially a tiny bolometer capable of measuring the heating caused by single photons [76]. The dark counts in a TES are caused only by background thermal radiation at the detector. The primary limitations of these detectors are their relatively low maximum count rate ($\lesssim$ 100 kHz), poor timing resolution (of order 10 μs) and requirement that they be operated at sub-Kelvin temperatures. Fortunately, none of these limitations affect the superposition experiment, which already requires mK temperatures, making this type of detector perfectly suited to our needs. Although these detectors are not commercially available at present, they have been fabricated by a number of groups.

3.5 Other Requirements

For the visibility fringes of a superposition-type experiment to remain constant, the cavity length must be stable to within the ground state wavepacket size, x_0, which is only a fraction of a picometer for an ideal device. Creating an optical cavity with this level of stability that can also be adjusted with micron precision in a vacuum and cryogenic environment is a significant challenge, although it seems to be within the reach of available technology (see also §7.2.3).

Although optical cooling does not apparently ease any of the requirements above, it is the only practical way to put the system in a known quantum state. As noted in §2.2.4, this may be required for an unambiguous demonstration of quantum behavior, although this issue remains contentious. Issues of interpretation aside, optical cooling is also useful in a superposition type experiment because it increases the width of the revival window, thus increasing the rate of experi-

mentally relevant photon counts. For the ideal device at a temperature of 1 mK, a photon is only expected to be detected in the revival window several times per day, assuming the experiment is run continuously (given $P(1) = 0.1$, $F = F_0$ and $\kappa = 1$). Cooling this system to the ground state gives an improvement of two orders of magnitude, or approximately a photon every minute. This would dramatically reduce the requirements on cavity stability and run-time of the cryogenic system, although it does not affect the dark count requirement for the single photon detectors.

Chapter 4

A Prototype Micro-Optomechanical System

This chapter is partially adapted from *Physical Review Letters* **96**, 173901, "High Finesse Opto-Mechanical Cavity with a Movable Thirty-Micron-Size Mirror," by D. Kleckner et al. [68], copyright ©2006 by The American Physical Society.

We now discuss the fabrication of an optomechanical system composed of a macroscopic spherical mirror and a microscopic plane mirror on the end of an atomic force microscope (AFM) cantilever (fig. 4.1). Prior to the realization of this system, the only significant radiation pressure induced optomechanical interactions had been observed in microtoroidal resonators [13], which operate at much higher mechanical frequencies (many MHz, as opposed to the 10 kHz systems described here).

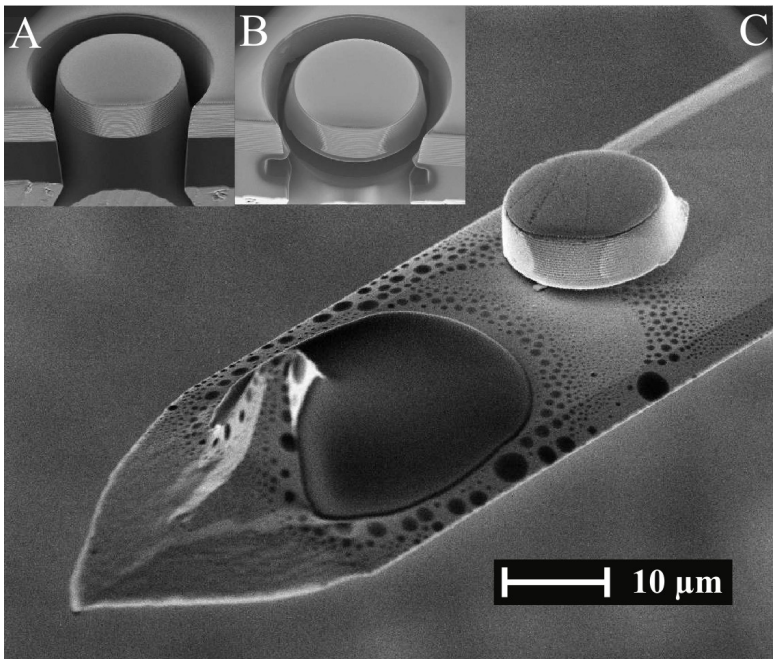

Figure 4.1: SEM images of a 15 μm prototype mirror during the cutting process (A, B) and after attachment to a cantilever (C).

4.1 Cavity Fabrication

4.1.1 Tiny Mirror and Resonator Fabrication

To make the tiny mirrors, we begin with a multilayer SiO_2/Ta_2O_5 DBR stack deposited on a conductive silicon substrate. The film deposition was done commercially by Advanced Thin Films, Inc., and designed to have a high enough reflectivity to allow cavities with $F \gtrsim 10^4$ (15 double SiO_2/Ta_2O_5 layers) at a center wavelength of 780 nm.

Using a focused ion beam (FIB), we first cut away a ring of material on the edge of the wafer to define the mirror shape (fig. 4.1A). We use a gallium ion current of 7 nA to cut a ring of width 3–4 μm, with the inner edge of the ring being the desired mirror size. The cut depth is several microns greater than the thickness of the mirror ($\sim 5\mu$m), which makes the mirror less likely to get stuck to the substrate after the side cutting.

We then rotate the sample 96° in order to cut out the bottom of the mirror from the side (fig. 4.1B). The additional 6° is used to compensate for the tapered edges of a FIB cut produced at high ion currents. The bottom cut is stopped before it completely frees the mirror, leaving it connected by 1–2 μm of silicon. We have successfully cut mirrors of between 15 and 30 μm diameter; larger mirrors should be possible but the total time required to cut them at this beam current would be on the order of 1 hour.

After cutting several mirrors in this fashion, we remove the mirror piece from the FIB system and prepare several AFM cantilevers. We place a small drop of low-viscosity optical epoxy near the tip of each cantilever using a several micron thick pulled glass rod on a manipulation arm. Then, using a fresh glass tip, we gently break a mirror free from the substrate. To avoid scratching the mirror, we use the side of the glass rod instead of the sharp tip. It has been found useful to use a larger ($\gtrsim 30$ μm) glass rod for this purpose, as it is less prone to breakage.

A snapped glass rod typically results in the mirror launching violently from the substrate where it is unlikely to be recovered by the bewildered researchers. Once freed, the detached mirror is carefully lifted from the substrate via electrostatic interaction with the glass rod. It is then transferred to the cantilever and placed on the drop of epoxy (fig. 4.1C). The cantilever is then placed in a designated holder and gently heated to cure the epoxy.

4.1.2 Cavity Alignment System

Because one end of our optical cavity is of microscopic dimensions, mirror alignment is extremely critical. In general, we find that placing the cavity in a vacuum chamber, required to reduce background gas damping of the mechanical resonator, results in non-negligible misalignment of the system. To allow alignment of the system in vacuum, we use three slip-stick piezo screw motors (New Focus Picomotors) which push against the plate which holds the macroscopic end mirror (fig. 4.2). This configuration is similar to that used in a common laboratory optical mount, and allows us to tip and tilt the big end mirror about its center, as well as change the length of the cavity. The other two degrees of freedom in the cavity alignment are the tip and tilt of the cantilever, for which we use a conventional gimbal optical mount. Although this mount can only be adjusted manually, we find that it can be pre-aligned, outside the vacuum chamber, to an adequate degree of precision. A diagram of the complete optical system can be found in fig. 4.3.

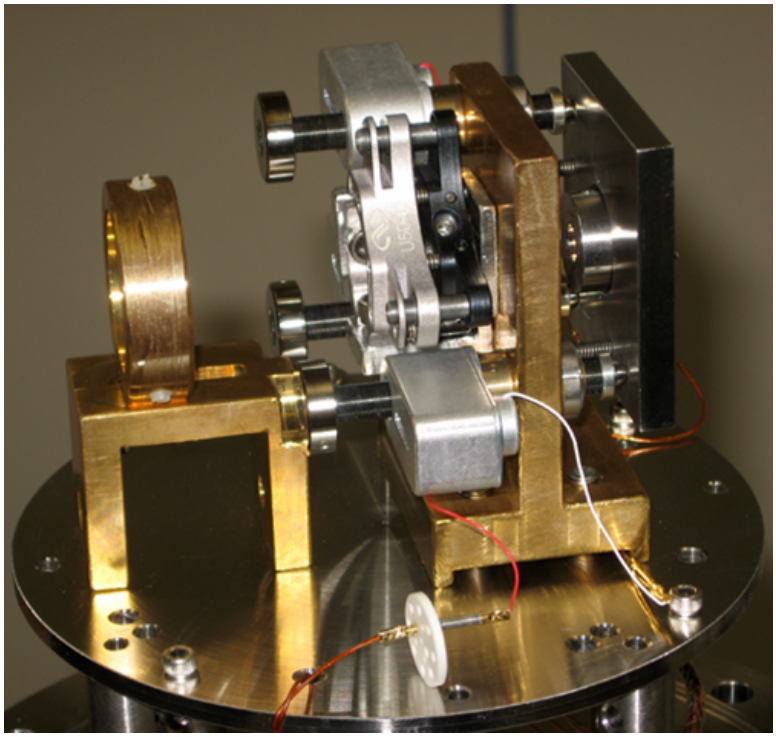

Figure 4.2: An image of the cavity-alignment vacuum insert. The macroscopic cavity mirror and the input mode matching lens is mounted on the plate at the far right, which is adjustable using three remotely controlled motors. The tiny mirror/AFM cantilever is held in the gimbal optical mount in the center of the image, located between the three motors. Because it is less critical than the other degrees of freedom, the angle of the cantilever can be adjusted only while the system is outside the vacuum chamber. An imaging lens, shown on the left, is used to focus the light leaving the optical cavity.

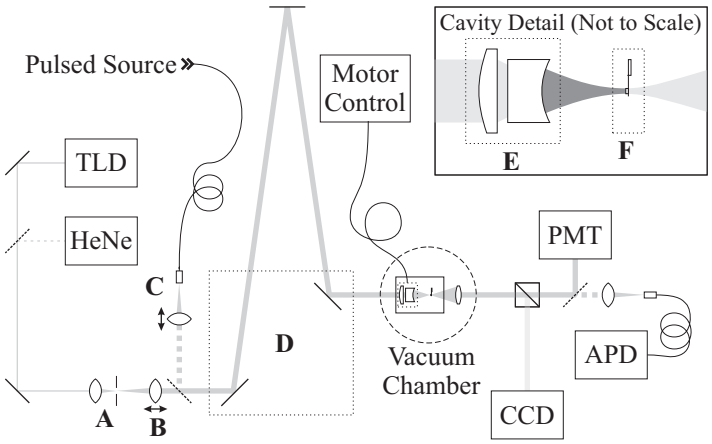

Figure 4.3: A diagram of the experimental setup. A 780 nm tunable diode laser (TDL) is used for frequency scanned measurements. A 633 nm HeNe laser is used for alignment as it is out of the peak reflectivity region of the mirrors. The light from either laser is then passed through a spatial filter (A) and collimated using a lens on a translation stage (B). The lens is chosen to match the cavity mode. For the ring-down measurements a 780 nm 200 fs pulsed laser is coupled in via a fiber (C). A periscope (D) aligns light to the cavity. The large mirror and an incoupling lens (E) are mounted on a motorized stage allowing control of tip/tilt as well as the overall length of the cavity inside the vacuum chamber. The cantilever/small mirror (F) are mounted on a gimbal mount which is pre-aligned outside of the vacuum chamber. A fraction of the light leaving the cavity is used for imaging on a CCD, while the remainder is sent either to a photomultiplier tube (PMT) or avalanche photodiode (APD).

4.2 Results

4.2.1 Optical Quality

To characterize the optical cavity, we measure its spectral response using a tunable diode laser (TDL). The transmission of a Fabry-Pérot cavity as a function of frequency, f, and changes in cavity length, Δx, is:

$$T \propto \frac{1}{1 + \frac{4F^2}{\pi^2}\sin^2[\pi(\frac{f}{\Delta f} + \frac{2\Delta x}{\lambda})]} \tag{4.1}$$

where λ is the laser wavelength, and $\Delta f = \frac{c}{2L}$ is the free spectral range, which is 6 GHz for our cavity. The proportionality factor is 1 for cavities with mirrors of equal reflectivity and less than 1 otherwise. The optical finesse, F, a useful measure of the cavity quality, is the ratio of peak width to free spectral range for the periodic peaks of eqn. 4.1. Using the TDL we sweep the frequency by slightly more than a free spectral range and monitor the cavity transmission on a photomultiplier tube (PMT) (fig. 4.4). The power incident on the cavity is roughly 1 mW. In practice a series of several reoccurring peaks is observed due to higher order modes and imperfect mode matching. The peak of the fundamental mode can easily be identified by its higher finesse and location in the spectrum. If the laser is scanned slowly enough, thermal vibrations of the cantilever at the primary mechanical resonance frequency of 12.5 kHz are clearly visible (fig. 4.4B). This is because the time it takes the TDL to scan over the peak is several mechanical oscillations long. Scanning at a rate $\gtrsim$ 10 Hz reduces the effect of the vibrations and enables a measurement of the linewidth of the cavity optical resonance. The maximum finesse measurable by this method is 1020 $\pm$ 50 and is limited by the 6 MHz TDL linewidth.

Cavity ring-down provides an alternative method for determining the finesse. The mean number of round trips of a photon in a Fabry-Pérot cavity is given by $N = \frac{F}{2\pi}$. The corresponding exponential decay time is $\tau = \frac{LF}{\pi c}$. To measure this

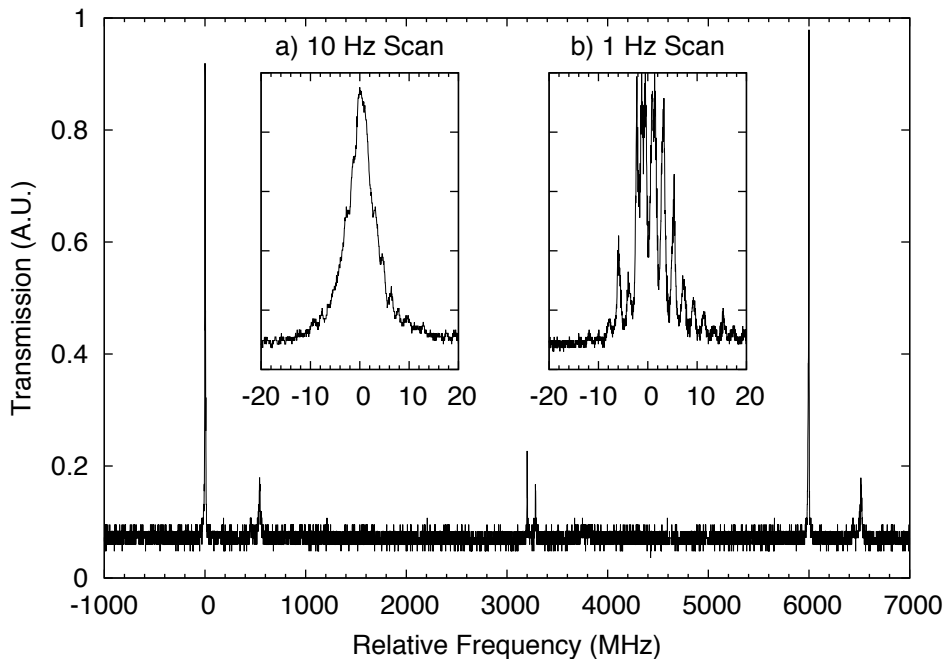

Figure 4.4: Fabry-Pérot scan (peaks inset). Higher order modes are visible; adjustment of the incoupling reveals that the cavity supports several more. **A)** The Lorentzian peak has FWHM 5.9 ± 0.2 MHz, resulting in an equivalent finesse (limited by the laser linewidth) of 1020 ± 50. **B)** If the laser is scanned at a lower rate, thermal vibrations of the cantilever become visible.

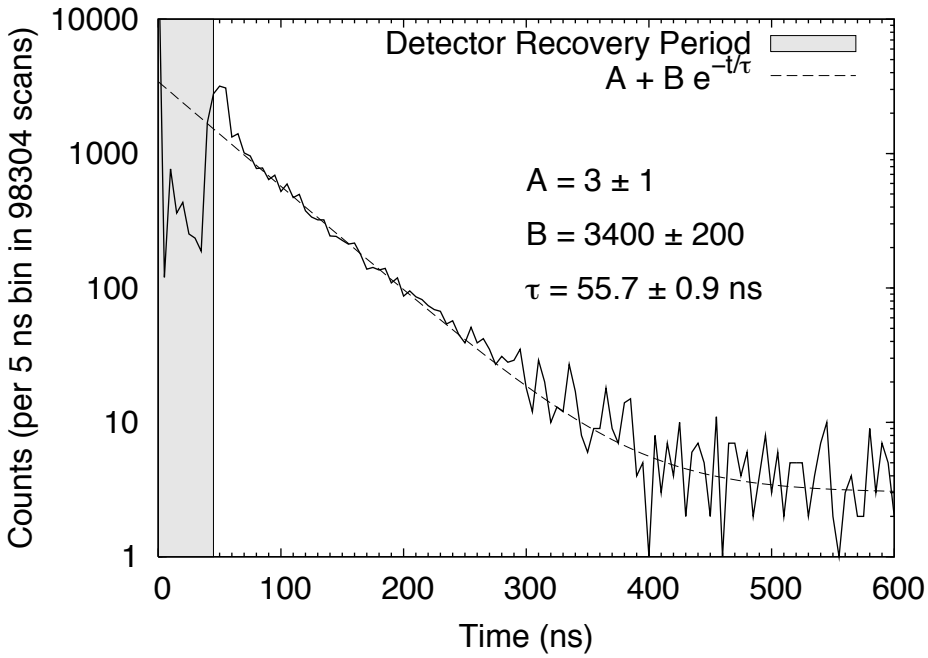

Figure 4.5: Cavity ring-down measurement. A laser pulse enters the cavity at a time $t = 0$. The scattered light is bright enough to saturate the APD, resulting in a 50 ns dead time. The light intensity is low enough after the recovery that saturation effects can be ignored. A fit of the data from 100–2000 ns demonstrates a finesse of 2100 ± 50. The slightly faster decay at 50 ns is due to light leaking from higher order modes.

decay we pumped the cavity with 200 fs laser pulses at 780 nm with a repetition rate of 40 kHz. Light leaving the cavity was sent to an avalanche photodiode (APD) capable of detecting individual photons. The APD pulses were monitored on a multichannel scaler triggered by the laser electronics. The summed results of 10^5 pulses are shown in fig. 4.5. The cavity alignment was unchanged from the earlier measurements using the TDL. The measured finesse by this method is 2100 ± 50. The finesse could not be significantly increased beyond this point by adjusting the alignment.

We now discuss limitations on the optical finesse set by the finite size of the cavity mirrors. Because of diffraction losses, the concept of eigenmodes of the

Mirror Sizes	Fundamental Mode Finesse	Finesse of Higher Order Modes (with $F > 10$)
6 mm, 15 μm	3.9×10^4	83
6 mm, 20 μm	3.5×10^6	3500, 24
w/ 2 μm defect	6000	39
6 mm, 30 μm	3.6×10^{10}	1.4×10^7, 2.7×10^4, 190
w/ 2 μm defect	4.5×10^5	3.0×10^4, 240, 13
8 mm, 20 μm	1.6×10^9	8.0×10^5, 2200, 24

Table 4.1: Maximum optical finesse for finite-sized mirror cavities of the type presented here ($\lambda = 780$ nm).

cavity breaks down and is replaced by modes that decay at a constant rate. The calculation of these modes can be reduced to a round-trip matrix problem by expanding the optical field in the cavity in terms of the cylindrically symmetric ($m = 0$) Laguerre-Gaussian modes which are the propagation eigenmodes of the paraxial wave equation for a cavity with infinitely large mirrors. The clipping due to each mirror is represented by a mode mixing matrix whose elements are the mode overlap integrals calculated only over the surface of the mirror. The effect of one round trip propagation is the product of the mixing matrices for each mirror. The eigenvalues and eigenvectors of this matrix correspond to the cavity modes and can be used to calculate the finesse (table 4.1) of each. A more sophisticated version of this method is discussed in §6.

Many of the obtained finesses exceed those limited by realistic mirror reflectivities [66]. Since the finesse is limited by multiple independent loss mechanisms, the total finesse can be calculated from the limiting finesses for each loss mechanism considered separately: $\frac{1}{F} = \frac{1}{F_{\text{diff.}}} + \frac{1}{F_{\text{refl.}}} + \ldots$ To determine the diffractive losses of single point defects in the mirror, calculations were carried out with the center 2 μm of the small mirror removed. As can be seen in table 4.1, this results in a decrease in the overall finesse as well as a reduction in the number of efficiently propagating modes. Conversely the number of prominent modes is not affected

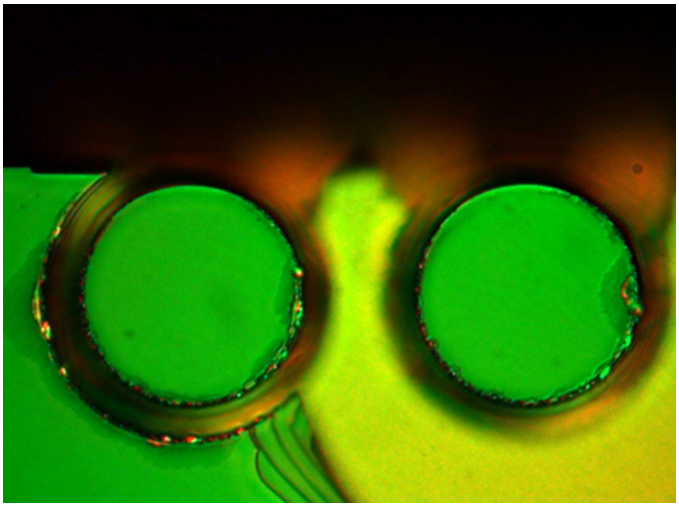

Figure 4.6: An optical microscope image of two 30 μm diameter mirrors cut on the FIB. Contamination from the FIB cutting is clearly visible near the edges of the mirror.

by a decrease in overall reflectivity. The frequency scanned measurements show that the number of prominent higher order modes for 20 and 30 μm mirrors is approximately consistent with the calculations for defect-less mirrors. Despite this, we always observed considerably lower finesse with 20 μm mirrors in comparison to 30 μm mirrors, which would not be expected from an overall reduction in reflectivity (or increase in surface scattering). We thus suspect that the finesse limitation is due to scattering off of small surface contaminants concentrated near the mirror edges, effectively reducing the reflectivity.

The most likely source of contaminants is the FIB cutting procedure, and so we developed methods to protect it during this step. We experimented with coating the mirror surface with materials that could easily be removed later, in particular several types of photoresist and electron beam evaporated germanium. Apparently due to the high temperatures experienced by the material during the cutting, we found it virtually impossible to remove the photoresist near the cut regions. Germanium, which can be quickly removed in a heated H_2O_2 solution,

proved to be a better coating material. Unfortunately, the conductive nature of this coating means that it has to be removed before the mirror is placed on the cantilever, as it will not stick to the glass rod used for positioning. We observed 20 μm mirrors prepared in this manner that had a finesse comparable to that obtained previously with 30 μm mirrors, although no measurable improvement was observed in the 30 μm mirrors.

Despite the relative success of Ge coated mirrors, we still observed contamination from the FIB cutting near the edges of the mirror after the Ge was stripped (fig. 4.6). In addition to this, the failure of the protection method to increase the optical quality of the larger mirrors suggests that there are other problems with the fabrication method – considerably higher finesses should be possible with the coatings and mirror sizes used here. We believe that the limited optical quality is caused in some way by the FIB, due either to the high local temperatures obtained during the ion beam exposure or by some contamination of the mirror layers that occurs even when a protective coating is present.

4.2.2 Mechanical Quality

To measure the mechanical quality of the system, we observe the thermal vibration spectrum of the cantilever. This is done by locking the frequency of the TDL to the side of a cavity transmission peak with a slow (10 Hz) feedback loop. The thermal vibrations of the cantilever, with an RMS amplitude of 1.2 Å, are immediately visible as fluctuations in the output intensity. The finesse is intentionally reduced to $\sim$150 by slight cavity misalignment to prevent transient vibrations from unlocking the feedback loop. By monitoring the transmission fluctuations on a spectrum analyzer, we can determine the spectral width of the fundamental cantilever vibrational mode, centered at 12.5 kHz (fig. 4.7). The

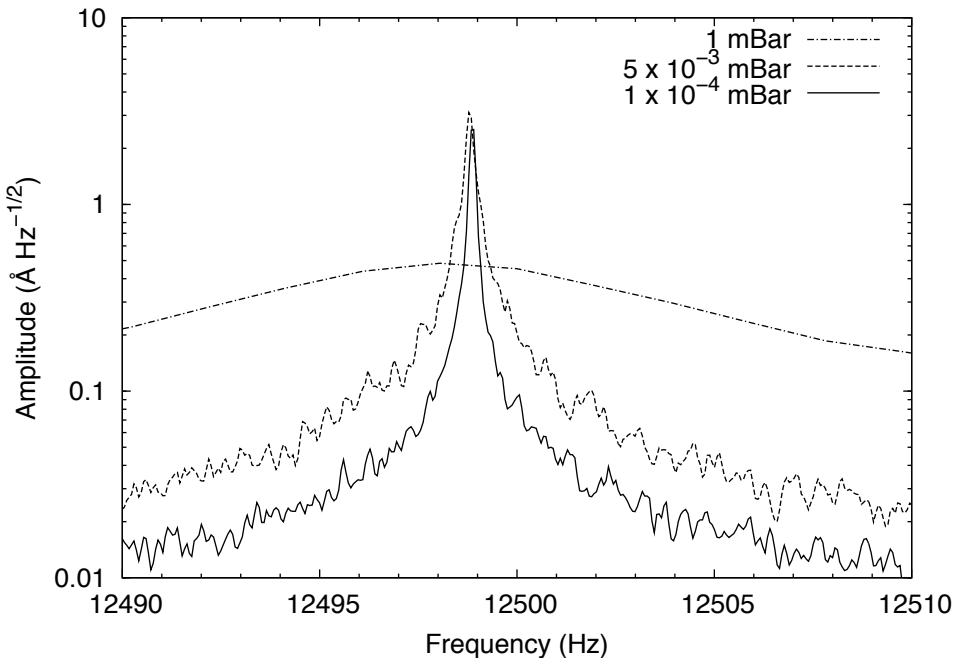

Figure 4.7: The spectral density of the mechanical resonance for a range of vacuum pressures. As the background pressure is reduced, the mechanical quality factor increases until it saturates at $(1.37 \pm 0.03) \times 10^5$ for pressures below 10^{-4} mbar.

mechanical quality factor is then given by:

$$Q = \frac{\omega_0}{\Delta\omega_{\mathrm{FWHM}}}. \tag{4.2}$$

As expected, Q is found to be dramatically reduced in low vacuum or atmospheric conditions. As the pressure is decreased, Q increases until it becomes intrinsically limited by cantilever material/construction (table 4.2). For our system, this happens at pressures below 10^{-3} mbar and gives a mechanical quality factor of $Q \sim 10^5$, with some slight variation between individual devices. At slightly higher pressures, we observe a quality factor in good agreement with the value predicted by gas damping in the free molecular regime (eqn. 3.21). The intrinsically limited value is consistent with the expected value for our cantilever

Pressure	Measured Q	RMS Amplitude	ℓ	Q_P
1 Atm.	79.7 ± 0.3	1.6 ± 0.2 Å	100 nm	< 1
1 mbar	1479 ± 8	1.8 ± 0.3	100 μm	350
5×10^{-3} mbar	(7.91 ± 0.08) $\times10^4$	1.6 ± 0.2	20 mm	7×10^4
1×10^{-4} mbar	(1.37 ± 0.03) $\times10^5$	1.2 ± 0.2	1 m	3.5×10^6

Table 4.2: Measured mechanical resonance properties of the cantilever at different pressures. The approximate mean free path of the background gas, ℓ (eqn. 3.19), and gas damped mechanical quality factor, Q_P, for the free molecular regime (eqn. 3.21) are also shown. The effective gas molecule diameter is assumed to be $d \sim 3$ Å and the background temperature is taken as 300 K.

dimensions (450 × 50 × 2 μm) [77]. It appears therefore that the mechanical Q of the cantilever is not significantly affected by the mirror attachment process.

4.3 Prospects

The thermal vibrations of this system are visible with a signal-to-noise ratio of greater than 10^5, implying that optical feedback cooling [78] of the center of mass motion of the cantilever to sub-Kelvin equivalent temperature is possible from room temperature. This will be demonstrated experimentally in §5.

It should also be possible to observe nonlinear effects due to optomechanical coupling with the current system by modest increases in either finesse or input power. Alternatively, if the reflectivity of the larger mirror in our current cavity were reduced to match the effective reflectivity of the tiny mirror, nonlinear effects would become significant with input powers of order 100 μW [23].

Concerning further improvement of our system, we have shown numerically that a finesse several orders of magnitude higher should be possible with improved mirror fabrication techniques. In order to use the system to realize a macroscopic superposition, it also needs to be shown that mirrors can be attached to significantly thinner and lighter cantilevers and that high mechanical quality factors can be maintained in such cases. If this can be achieved, the most significant barriers

to creating a massive "Schrödinger's cat" state, as proposed in [4], will have been overcome.

Chapter 5

Experimental Demonstration of Feedback Cooling

This chapter is adapted from *Nature* **444**, 75, "Sub-kelvin optical cooling of a micromechanical resonator," by D. Kleckner and D. Bouwmeester [47], copyright ©2006 by the Nature Publishing Group.

Micromechanical resonators, when cooled down to near their ground state, can be used to explore quantum effects such as superposition and entanglement at a macroscopic scale [3, 4, 17]. Prior to the publication of this experiment, it had been proposed to use electronic feedback to cool a high frequency (10 MHz) resonator to near its ground state [79]. In other work, a low frequency resonator was cooled from room temperature to 18 K by passive optical feedback [60]. Additionally, active optical feedback of atomic force microscope cantilevers had been used to modify their response characteristics [80], and cooling to approximately 2 K has been measured [81]. In even earlier work, electric feedback was used to reduce the Brownian motion of an electrometer to an equivalent temperature of only 3 K[82]. The work here was published simultaneously with two other articles demonstrating feedback cooling in similar systems [50, 51]. Subsequent to this publication, optical feedback cooling was realized in a large number of optomechanical systems (e.g.

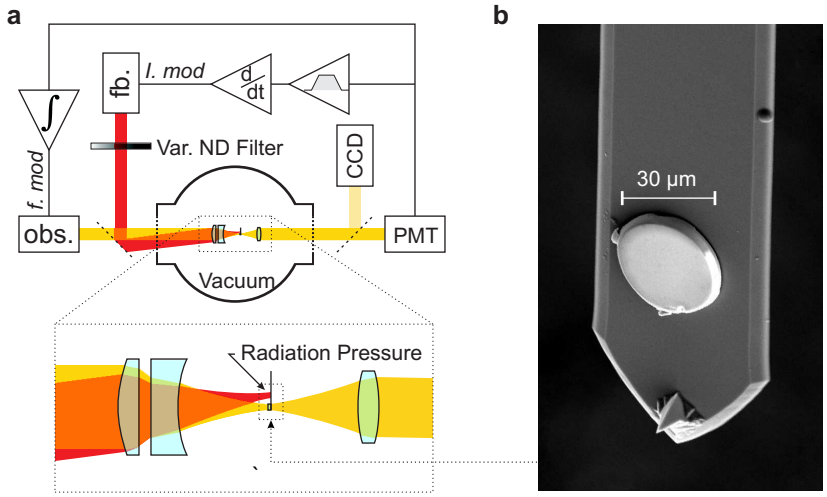

Figure 5.1: The experimental system. **Left:** A diagram of the feedback mechanism: a 780 nm observation laser (Obs.) is frequency locked to the optical cavity (shown magnified at bottom) with an integrating circuit (via the laser frequency modulation input, f. mod), using the signal from a photomultiplier tube (PMT). This signal is also sent through a 1.25 kHz bandpass filter at 12.5 kHz and a derivative circuit (d/dt) to provide an intensity-modulating signal (I. mod.) for the 980 nm feedback laser (Fb.). The feedback laser is attenuated with a variable neutral density (ND) filter to adjust the gain of the feedback. The feedback force is exerted on the cantilever via this laser's radiation pressure. **Right:** Scanning electron microscope image of the tip of the cantilever with attached mirror.

[15, 48, 52–59]).

We demonstrate active optical feedback cooling to 135±15 mK of a micromechanical resonator integrated with a high-quality optical resonator. Additionally, we show that the scheme should be applicable at cryogenic base temperatures, allowing cooling to near the ground state that is required for quantum experiments - near 100 nK for a kHz oscillator.

5.1 Method

Using a laser tuned to the resonance fringe of a high finesse optical cavity, it is possible to observe very small fluctuations in the length of the cavity due to Brownian motion of one or both of the end mirrors. Here we use the optomechanical system described in §4. The motion of the tiny mirror/cantilever is monitored by measuring the transmission of the cavity at a frequency on the side of an optical resonance peak. To do this, we use about 1 mW from a 780 nm tunable diode laser which is locked to the resonance fringe using the integrated signal from a photo-multiplier tube which monitors the light transmitted through the cavity (fig. 5.1a). The time derivative of this signal is proportional to the velocity of the cantilever tip and is used to modulate the intensity of a second, 980 nm, diode laser focused on the cantilever approximately 100 μm away from the tiny mirror. The radiation pressure exerted by this feedback laser counteracts the motion of the mirror and effectively provides cooling of the fundamental mode.

The effective feedback gain can be varied over several orders of magnitude by sending the feedback laser through a variable neutral density filter. The average power in the feedback beam when it reaches the cantilever is of the order of 1 mW at the highest gain settings and proportionally lower otherwise. The mean modulation depth of the feedback beam varies from nearly 100% to less than 5% as the gain is increased. The vibration spectrum of the cantilever as a function of gain is shown in fig. 5.2. The RMS thermal amplitude of the cantilever without feedback is 1.2 ± 0.1 Å. From this value, one can calculate that the spring constant of the cantilever is 0.15 ± 0.01 N m^{-1}, in agreement with the manufacturer-specified range, and the effective mass of the cantilever fundamental mode is $(2.4 \pm 0.2) \times 10^{-11}$ kg.

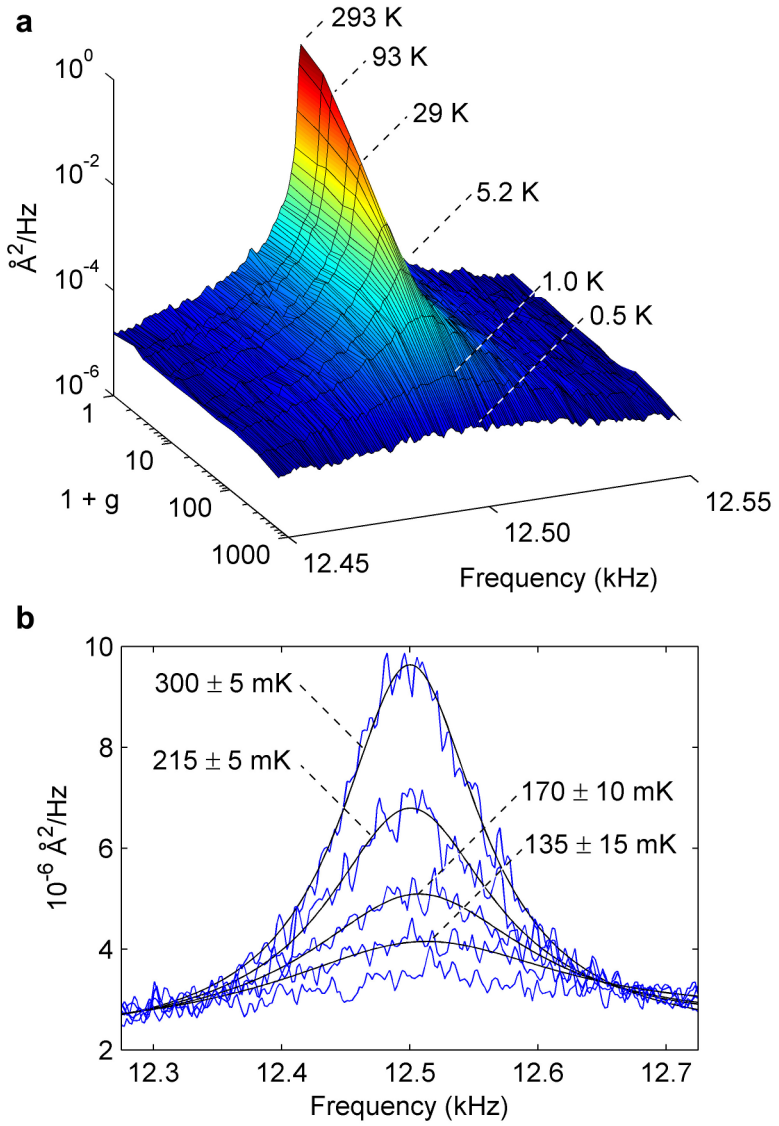

Figure 5.2: Single-sided thermal vibration spectrum of the cantilever as it is cooled. g is the dimensionless gain factor, which is the ratio of feedback to mechanical damping. **a)** Spectrum at low to moderate gains. **b)** Spectrum near the background noise level for large gains. The blue curves correspond to experimental data, and the black curves to fits of a Gaussian function plus a background. The lowest trace cannot be reliably fitted.

5.2 Results

To determine the effective gain of the feedback loop and the temperature of the fundamental mode, we fit a Lorentzian plus a constant background to the vibration spectrum of the cantilever for each value of feedback gain. The temperature is determined from the area under the Lorentzian without the background, while the gain is determined by the width of the resonance. The linewidth provides a good measure of gain because it is directly determined by the damping rate whereas the cantilever amplitude may be affected by other sources of noise in the feedback loop. Cooling is observed over more than three orders of magnitude. The lowest temperature we are able to measure is 135 ± 15 mK, or a cantilever RMS amplitude of 0.023 ± 0.002 Å, with a gain (the ratio of feedback to mechanical damping) of $g = 2490 \pm 90$. The lowest trace in fig. 5.2, indicating an even lower temperature, cannot be reliably fitted owing to the laser noise floor. Since the optical finesse is not the current limiting factor, we operate the opto-mechanical system at a finesse of only 200, produced by slight cavity misalignment, which makes the system less sensitive to transient vibrations.

The amplitude of the mirror motion can be calculated in the presence of feedback by assuming that the Langevin force (the effective thermal force that maintains Brownian motion) remains constant while the mechanical susceptibility of the mirror is reduced by the dissipation due to the radiation feedback pressure. It suffices to consider only the fundamental mode of the mirror motion, represented by a damped harmonic oscillator. In this approximation, the power spectrum of the mirror's motion in the presence of feedback is given by [45]:

$$S_{x,fb}(\Omega) = \frac{2\Gamma_0 k_b T_0}{m} \frac{1}{(\Omega^2 - \omega^2)^2 + (1+g)^2 \Gamma_0^2 \omega^2}, \tag{5.1}$$

where Ω is the observation frequency, Γ_0 is the intrinsic mechanical damping constant, m is the mass of the resonator mode, ω is the resonator frequency, k_b is Boltzmann's constant, T_0 is the bulk temperature of the resonator and g is

the feedback gain constant. As discussed in §2.3, increasing the gain effectively decreases the resonator temperature and increases the damping rate by a factor $1 + g$.

The optical feedback scheme, when analyzed in terms of noiseless classical light fields, can be seen as a virtual viscous force, which, unlike a real viscous force, creates dissipation without introducing fluctuations. As discussed below, the cooling temperature as demonstrated here is limited by laser frequency fluctuations. Ultimately, optical cooling should be limited by the balance of residual heating and quantum noise in the observation and feedback laser signals.

For a signal-to-noise ratio of one in spectral density at the peak of the mechanical resonance, the temperature of the cantilever resonance would be (as can be derived from eqn. 5.1):

$$T_{min} \cong \sqrt{\frac{T_0 m \omega^3 S_{meas}}{2 k_b Q}}, \tag{5.2}$$

where S_{meas} is the equivalent position noise in the interferometer measurement and $Q = \omega/\Gamma_0$ is the mechanical quality factor. For higher values of gain, the feedback signal is mostly noise and lower temperatures can not be conclusively demonstrated. For our experiment, the equivalent noise level is $S_{meas} \approx 10^{-3}$ ÅHz$^{1/2}$. This corresponds to the expected noise due to the frequency fluctuations of a free running tunable laser diode, which are of order 10^3 Hz Hz$^{-1/2}$ at the resonance frequency of 12.5 kHz [83]. With the system in vacuum at pressures of 10^{-6} mbar, so as to maximize the mechanical quality factor of the cantilever, this noise level corresponds to a minimum temperature of the order of 100 mK, in good agreement with the experimental data.

5.2.1 Temporal Response

An alternative approach to study the cooling is to analyze the temporal response of the system by gating the signal to the feedback laser. The characteristic

time constant for the system to reach equilibrium after the cooling is turned on is given by:

$$\tau_{fb} = \Gamma_{fb}^{-1} = (1+g)^{-1}\Gamma_0^{-1}. \tag{5.3}$$

To observe this behavior, we monitor the cantilever over many 10 s periods during each of which the cooling is on for 3 s. Data for cooling to 1.8 ± 0.2, 4.0 ± 0.2 and 6.4 ± 0.1 K and returning to thermal equilibrium are shown in fig. 5.3. The cooling times are measured to be 9.0 ± 0.5, 19 ± 1 and 27 ± 1 ms, respectively. The reheating time is found to be indistinguishable for all three gains with an average of $t_0 = 1.30 \pm 0.05$ s. This is in agreement with the linewidth of the cantilever measured without feedback, $\Gamma_0 = 680 \pm 50$ mHz. In accordance with theory, the ratio of the reheating to the cooling times, τ_0/τ_{fb}, and the corresponding ratio of the spectral linewidths from the earlier measurements, Γ_{fb}/Γ_0, are found to be the same as the cooling factor, T_0/T_{fb}, within statistical uncertainties.

5.2.2 Radiation Pressure and the Photothermal Force

In experiments where optical feedback is used on cantilevers with non-uniform composition, radiation pressure is typically overwhelmed by the photothermal force, which is an effective force due to thermally induced bending [60, 80]. Although this is not the case for single-crystal silicon cantilevers, the addition of a tiny mirror on the tip of our cantilever should produce a weak photothermal force. This force can be distinguished from radiation pressure by its dependence on the intensity modulation frequency of the feedback laser. Whereas radiation pressure is independent of modulation frequency, the photothermal force is not, because it has a characteristic response time, τ, related to the thermal relaxation time of the cantilever. A simple model for the frequency dependence of the photothermal force, $F_{pt}(\Omega)$, gives:

$$F_{pt} \cong \int_0^\infty \frac{F_{pt}(0)}{\tau} e^{-\frac{t}{\tau}} e^{-i\Omega t} dt = \frac{F_{pt}(0)}{1+i\Omega t} \tag{5.4}$$

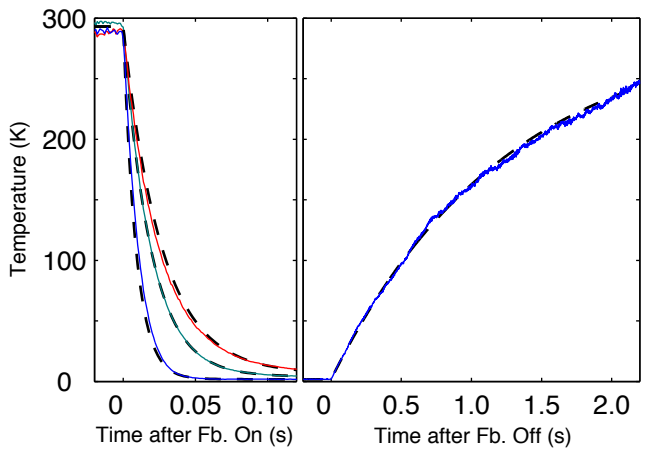

Figure 5.3: Temporal response of the cantilever to cooling pulses. The temperature is determined by calculating the total vibrational amplitude of the cantilever between 12 and 13 kHz in 1 ms bins and subtracting the background. Each data set is the average of 1,000 samples. The three sets in the left panel correspond to cooling to 6.4, 4.0 and 1.8 K (solid lines, top to bottom). Heating is shown (right panel) for only one data set (1.8 K), as all three are nearly coincident. The dashed lines are fits to exponential decays, used to determine the cooled temperature and the cooling and reheating times. Fb. refers to the feedback system.

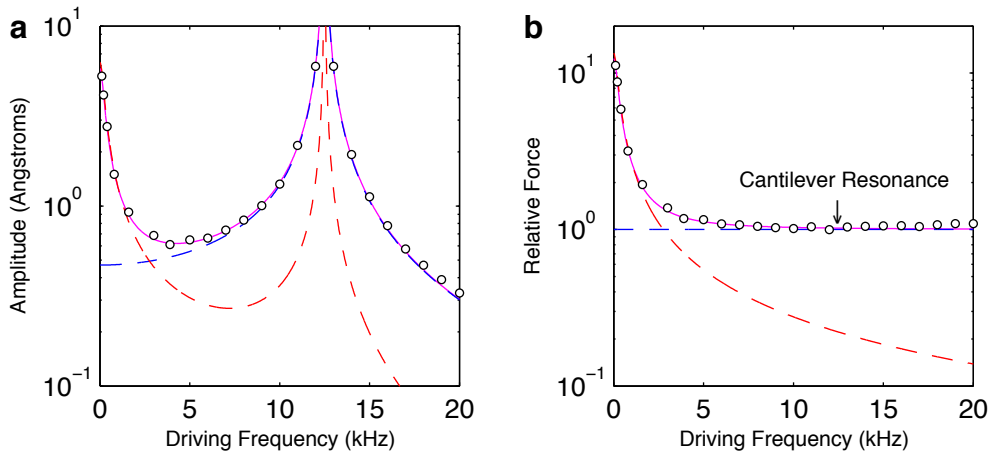

Figure 5.4: Response of the cantilever to an external intensity-modulated laser. **a)** The amplitude of the cantilever's motion at the driving frequency. **b)** The force on the cantilever, calculated by dividing the amplitude by the mechanical amplification of the cantilever. In both graphs the magnitude of the contributions (ignoring phase differences) of the photothermal force and radiation pressure are shown as red and blue lines, respectively. The slight deviation of the fit from the data at higher frequencies is due to higher order flexural modes.

where $e^{-i\omega t}$ corresponds to the input power modulation, and $e^{-\frac{t}{\tau}}$ is due to the thermal relaxation. This is consistent with the frequency dependence of the photothermal force as described in previous work [80]. To test for the presence of photothermal force in our resonator, the feedback laser was modulated at a range of frequencies from 100 Hz to 20 kHz and the mechanical response of the cantilever was measured as before (fig. 5.4). The power in the feedback laser reflected from the cantilever was determined to have a mean of 2.7±0.5 mW and a modulation amplitude of 1.0 ± 0.2 mW, independent of the modulation frequency. This results in a radiation pressure force of $F_{rad} = 2P_{mod}/c = 6.7 \pm 1.3$ pN (where P_{mod} is the amplitude of the power modulation and c is the speed of light) at the modulation frequency.

If the driving frequency is sufficiently far from the cantilever resonance, the mechanical damping constant can be ignored and the amplitude of the cantilever's

motion should be of the form:

$$A(\Omega) = \left| \frac{\frac{A_{pt}}{1+i\Omega t} + A_{rad}}{1 - (\Omega/\omega)^2} \right| \tag{5.5}$$

where Ω is the driving frequency, and A_{rad} and A_{pt} are the magnitudes of the motion due to the radiation pressure and photothermal force alone, at zero frequency. The term in the denominator is due to mechanical amplification by the cantilever resonance. This equation fits well to the measured response, resulting in $A_{rad} = 0.470 \pm 0.005$ Å, $A_{pt} = 6.3 \pm 0.2$ Å and $\tau = 30 \pm 2$ ms. At frequencies greater than 5 kHz, radiation pressure is observed to be the dominant force mechanism, whereas the photothermal force is relevant only at lower frequencies.

Assuming the constant force background described by A_{rad} is entirely due to radiation pressure, one can calculate the spring constant of the cantilever at the position where the feedback laser is focused to be $k = F_{rad}/A_{rad} = 0.14 \pm 0.03$ N m^{-1}, in agreement with the value for the spring constant obtained earlier. Near the fundamental resonance of the cantilever, the radiation pressure is calculated to be almost 5 times larger than the photothermal force. Additionally, the two forces should be nearly 90° out of phase at this frequency, given that the time constant of the photothermal force is found to be 30 ± 2 ms. Thus we conclude the radiation pressure is responsible for virtually all of the demonstrated feedback cooling.

When optical cooling is active, the cantilever's motion is strongly damped, making it undesirable for many types of measurements. In some cases this problem can be overcome with a stroboscopic cooling scheme, where measurements are only made in the periods when the cooling is off. In addition to being of direct importance for the aforementioned massive superposition experiment, this scheme has already been theoretically shown to be useful for high sensitivity measurements of position and weak impulse forces [84]. Because the cooling is faster than the heating by a factor (1 + g), a low temperature can be maintained even when the

cooling is off the majority of the time. However, maintaining low temperatures requires that the measurement window be short; if it is, for example, one oscillation period long, the temperature of the oscillator will have increased by $\Delta T \sim 2\pi T_0/Q$ by the end of each measurement window, meaning that cooling past this point results in marginal improvement.

5.3 Feasibility of Cooling for Quantum Experiments

We now evaluate the potential for reaching even lower temperatures for the purpose of studying quantum effects in similar systems. For simplicity, we will consider the ideal optomechanical system discussed in §3. A system optimized for a superposition-type experiment is on the edge of the side-band resolved regime, and so either active or passive optical cooling should be theoretically capable of reaching low phonon numbers. (In practice, the choice of optimal cooling scheme will depend on the precise system parameters.)

If the optical finesse is of order $F = 10^6$, the mechanical frequency is $\omega = 2\pi \times 500$ Hz and the mechanical quality factor is $Q = 10^5$, the readout beam for an active cooling scheme requires a readout power on the order of 1 aW, or less than 10^4 photons per second, to reduce shot noise to the appropriate level for ground state cooling. (Similar power levels should be required for passive optical cooling.) Assuming the thermal conductivity of the cantilever is reduced to the one-dimensional quantum limit, the cantilever's thermal resistivity will be on the order of 1 K aW^{-1} at 1 mK base temperature [85]. Although this means that only a very small fraction of the input power can be absorbed by the cantilever, this is not entirely unreasonable for such a high quality optical system. The feedback pressure could be provided by a piezo actuator on the cantilever base or a feedback laser at a much longer wavelength; in either case the absorption

by the cantilever can be made negligible. Furthermore, it is unclear exactly how heating of the bulk resonator affects the temperature of the fundamental mode, as the thermal dynamics of mechanical resonators is nearly unexplored in this temperature regime.

If one is interested in only demonstrating ground state cooling, as opposed to using it as part of a larger experiment, it would be advantageous to use an optomechanical system with a mechanical frequency of order MHz so that it is well into the sideband resolved regime. This would allow one to work at slightly higher base temperatures, as the characteristic environmentally induced decoherence temperature, eqn. 2.39, is proportional to the mechanical frequency. Additionally, working well into the sideband resolved regime would make it easier to separate and identify the Stokes sidebands, which, as noted in §2.3.2, can be used as an unambiguous indication that ground state cooling has been achieved. The disadvantage of this approach is that a larger pump power will be required to offset the reduced optomechanical coupling constant, potentially making heating from optical absorption more of a concern.

Chapter 6

Diffraction Limited Optical Cavities

This chapter is adapted from the manuscript "Diffraction Limited High Finesse Optical Cavities," by D. Kleckner, W. Irvine, S. Oemrawsingh and D. Bouwmeester, currently under review by *Physical Review A*.

The coupling strength of an optomechanical system is maximized when the mass of the mechanical resonator is as small as possible and the optical finesse is as high as possible. As a result, a detailed understanding of diffraction induced cavity loss is required to optimize the system, especially if single photon-single phonon coupling is desired.

We present a new method for calculating the mode structure and losses of diffraction limited high finesse cavities, based on representing the optical mode as a superposition of the optical modes of a cavity with infinitely sized mirrors. This method is a significant improvement over the canonical diffraction kernel approach [86, 87], which is not suited to accurate simulations of very low loss cavities. A rudimentary calculation of this type was used previously by the authors in the context of an optomechanical system [68] and a related method was developed independently by Klaassen et al. to characterize cavities with chaotic mode

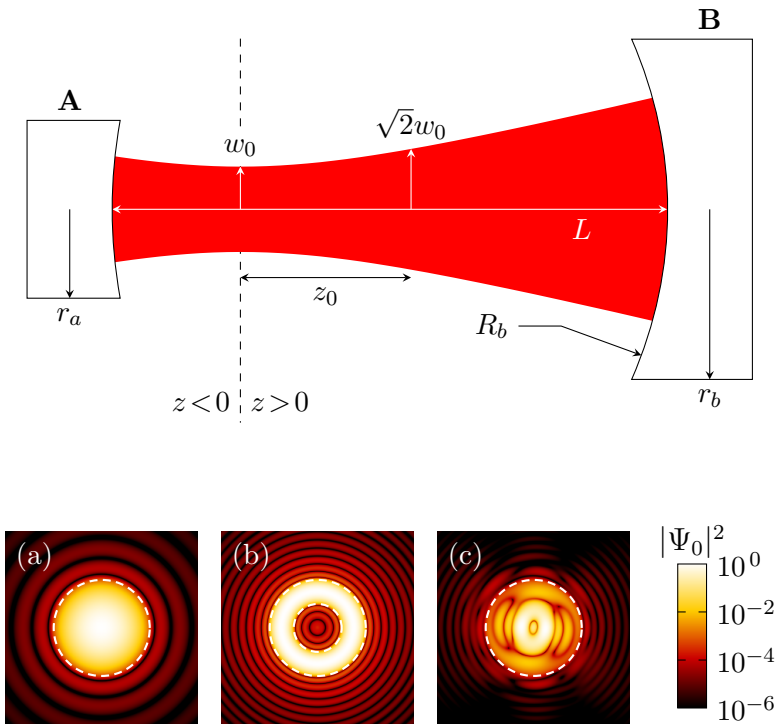

Figure 6.1: **Top:** A diagram of the cavity configuration. **Bottom:** An example of the effect on mode profile for several types of mirror imperfection. The profile of the fundamental mode is shown on mirror **B** for a cavity configuration given by eqn. 6.8 with $\zeta_b \to \infty$ and the dashed lines indicate the mirror edges. In general, the shape of the fundamental mode is found to deviate from a Gaussian in a way that minimizes loss. **(a)** A heavily diffraction limited cavity with $\alpha = 1.75$. **(b)** A region of radius $r_b/2$ is removed from the center of mirror **B** (with $\alpha = 3$). **(c)** Wavefront error is added to mirror **B** ($\alpha = 3$, $\nu_r = 3$ and $\sigma = 10^{-2}\lambda$; see eqn. 6.12).

structures [88]. Using this method, it is possible to calculate the effects of a wide number of imperfections, such as finite mirror size, defocusing, wavefront error or even removal of sections of the mirror (fig. 6.1), and to consider the advantages of different cavity geometries.

6.1 Calculation Method

Making use of Dirac notation, we begin by expressing the optical field, $|\Psi\rangle$, as a superposition of the modes of a cavity with infinitely sized mirrors, $|\psi_s\rangle$, or $|\Psi\rangle = \sum_s C_s |\psi_s\rangle$. We are interested in the eigenmodes of the optical cavity, given by:

$$\gamma_i |\Psi_i\rangle = \mathbb{M} |\Psi_i\rangle , \tag{6.1}$$

where $\mathbb{M}$ is the "mode-mixing operator," which gives the effect on $|\Psi\rangle$ of a round trip in the cavity. For a cavity with perfectly reflecting infinite size mirrors, this matrix would be diagonal. The eigenvalues of the system, γ_i, give the field amplitude change per round trip of the corresponding eigenmode, $|\Psi_i\rangle$.

The problem is now reduced to choosing an convenient set of basis states and calculating the elements of the mixing operator in this basis. Although in principle we need not do so, working in the paraxial approximation greatly simplifies the calculation. This also allows us to characterize many cavity geometries via a small number of easily computed quantities. For optical cavities with radial symmetry, a convenient set of basis states is provided by the Laguerre-Gaussian modes:

$$\psi^{\pm}_{n,m}(\rho,\phi,\zeta) = N\rho^{|m|} L_n^{|m|}\left[2\rho^2\right] e^{-\rho^2 \pm i\theta(\rho,\zeta)+im\phi} \tag{6.2}$$

$$\theta(\rho,\zeta) = -\zeta\rho^2 + (2n+|m|+1)\tan^{-1}\zeta \tag{6.3}$$

where $\rho = r/w(\zeta)$ and $\zeta = z/z_0$ are dimensionless radial and axial position coordinates, $w(\zeta) = w_0\sqrt{1+\zeta^2}$ is the mode radius, $z_0 = kw_0^2/2$ is the Rayleigh range,

n is the radial mode number, m is the helicity ($|m| \leq n$) and $L_n^{|m|}$ is a generalized Laguerre polynomial. The $\pm$ indicates the direction of propagation and $N_{n,m} = \sqrt{\frac{2^{|m|+1}n!}{\pi(n+|m|)!}}$ is the normalization constant that ensures $\iint \rho \; d\rho \; d\phi \, |\psi(\zeta)|^2 = 1$. The longitudinal phase shift of the traveling electromagnetic field, $\exp[\pm ikz]$, has been omitted and will be treated separately. The paraxial approximation should be valid as long as the waist of the cavity mode is larger than a wavelength.

We label the two end mirrors of the cavity **A** and **B**, each of which has a corresponding radius $r_{a/b}$, radius of curvature $R_{a/b}$ and location along the axis of symmetry $z_{a/b}$, which is defined relative to the mode waist (fig. 6.1). We then split the mode-mixing matrix in to two pieces, one for each end mirror. The elements of these matrices are given by mode overlap integrals taken over the finite extent of the mirrors:

$$\mathbb{A}_{s,t} = \int_0^{\rho_a}\int_0^{2\pi} \rho \; \mathrm{d}\rho \; \mathrm{d}\phi \; \psi_s^+ \psi_t^{-*} e^{-2ik\Delta_a(\rho,\phi)}\Big|_{\zeta=\frac{z_a}{z_0}} \tag{6.4}$$

$$\mathbb{B}_{s,t} = \int_0^{\rho_b}\int_0^{2\pi} \rho \; \mathrm{d}\rho \; \mathrm{d}\phi \; \psi_s^- \psi_t^{+*} e^{+2ik\Delta_b(\rho,\phi)}\Big|_{\zeta=\frac{z_b}{z_0}} \tag{6.5}$$

$$\mathbb{M} = \exp\left[2ikL\right] \mathbb{A} \times \mathbb{B}, \tag{6.6}$$

where s and t refer to one of the basis states and the upper bound to the integration over ρ is given by $\rho_{a/b} = r_{a/b}/w(\zeta_{a/b})$. The $\Delta_{a/b}$ term represents the deviation of each end mirror from planar – the deviation of a mirror with radius of curvature R is given by $\Delta(r) \cong \frac{r^2}{2R}$. In the equation for the round trip mixing matrix, $\mathbb{M}$, we have added the overall length induced phase shift which we omitted in the definition of the basis states.

From eqn. 6.2, it can be shown that the radius of curvature of the mode wavefront is given by $R_\psi(\zeta) = z_0\left(\zeta + \zeta^{-1}\right)$. If this curvature is matched to the curvature of the mirror there will be no overall radial phase shift in the mixing integral; we will refer to this case as a cavity which is "in focus." Note that for a radially symmetric cavity, the ϕ integral is trivial, reducing to a Kronecker delta

in m. This means helicity is preserved in these cavities, and modes with different values of m can be calculated independently.

In principle, the mixing matrix $\mathbb{M}$ acts on an infinite-dimensional mode space and its eigenmodes are exact solutions. Using a finite set of modes produces a perturbative solution; in this case the accuracy is dramatically improved if the basis states match the true fundamental modes of the cavity as closely as possible. When using the Laguerre-Gaussian modes, the basis states are determined by the (arbitrary) location of the $z = 0$ plane relative to the mirrors and size of the mode waist, w_0, where any set of values will create an infinite set of orthogonal modes. As a rule of thumb, a sufficiently accurate choice can be made by choosing the basis which maximizes $|\mathbb{M}_{0,0}|$. For simple geometries, the choice of basis states is readily apparent, but for more complicated cases it is often more convenient to optimize them numerically.

The power loss per round trip of each mode is given by $\delta_i = 1 - |\gamma_i|^2$. Although a mode is only in resonance when γ_i is real and positive, the phase shift can be corrected by a small offset to k, which will have negligible impact on the mode provided $kL \gg 1$. In this sense the complex phase of γ_i gives the relative detuning of the different modes, which may be useful in analyzing the modes of real optical cavities.

Since we are interested in the good cavity limit, we will take the optical finesse to be $F_i \cong 2\pi/\delta_i$. We ignore any losses due to the imperfect bulk reflectivity of the mirror, which would simply multiply all the elements of $\mathbb{M}$ by a constant. The resulting reduction in finesse is given by:

$$\frac{1}{F_i} = \frac{1}{F_{M,i}} + \frac{1}{F_R} = \frac{1}{F_{M,i}} + \frac{1-R}{\pi}, \tag{6.7}$$

where $F_{M,i}$ is the finesse calculated by a mode-mixing calculation with perfect mirrors, $F_R = \pi/(1-R)$ is the finesse limited by the bulk reflectivity alone and R is the bulk reflectivity, assumed to be identical for the two mirrors.

Typically, simulating modes up to $n = 15$ is accurate to a few percent. In

practice, we compute the integrals up to $n = 30$ numerically using Romberg's method with a 1025 point array of double precision floating point values. This is good enough to accurately simulate cavities up to $F \lesssim 10^{10}$, limited by the floating point precision. Note that this limit is considerably better than the experimental limit for real cavities imposed by mirror reflectivity, which is of order $F \lesssim 10^6$ in the visible to near infrared regime [66].

6.2 Cavity Length

We now demonstrate the utility of this method by using it on a variety of cavity geometries relevant to real experiments. First, to determine the effect of cavity length, we consider an "in focus" system where we fix one mirror at the mode waist:

$$\begin{aligned} r_a &= \rho_a w_0 & z_a &= 0 & R_a &= \infty \\ r_b &= \rho_b w(\zeta_b) & z_b &= L = \zeta_b z_0 & R_b &= R_\psi(\zeta_b) \end{aligned} \tag{6.8}$$

Setting $\rho_a = \rho_b = \alpha$ implicitly chooses the waist size, w_0, which maximizes $|\mathbb{M}_{0,0}|$, and so corresponds to the optimal basis state choice for the calculation. For such a cavity, the mixing matrices are identical apart from the Gouy phase, $(2n+|m|+1)\tan^{-1}\zeta_b$. This is expected; in this formalism, the Gouy phase completely describes the difference between the near field ($z \ll z_0$) and far field regime ($z \gg z_0$).

The plot of the finesse of the first several modes as a function of dimensionless length, ζ_b, is shown in fig. 6.2 for α =2.5, along with the finesse that would be expected for a unmodified Laguerre Gaussian mode (calculated from the self-overlap of single modes). Whenever a mode becomes resonant with a higher order mode (i.e. γ has the same complex phase for both modes), we find a strong enhancement of the finesse. This effect is analogous to a mode anti-crossing in a coupled oscillator system; it is only when the two modes are in resonance that

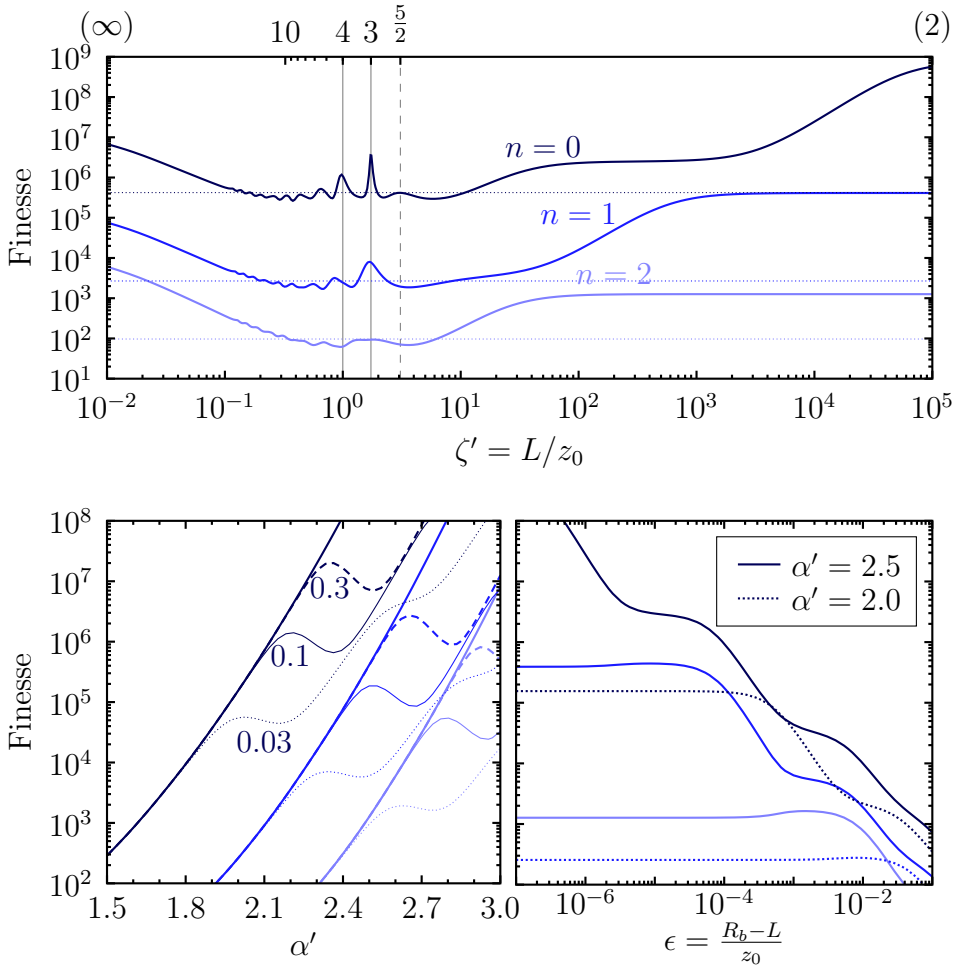

Figure 6.2: **Top:** The finesse of the first several zero helicity modes as a function of cavity length. The dotted lines show the finesse expected for a simple Laguerre Gaussian mode, which does not depend on the cavity length. The cavity geometry is given by eqn. 6.8 with $\alpha = 2.5$. The top axis shows the location of inter-mode resonances as given by $j = \pi/\tan\zeta_b$. **Bottom Left:** The thick lines show the finesse as a function of α for a cavity with $\zeta_b \to \infty$. The dotted, thin and dashed lines correspond to finite length cavities with $L = 10^5\lambda$ and $r_b/L = 0.03$, 0.1 and 0.3, respectively. **Bottom Right:** The finesse of a defocused infinite length cavity as a function of the dimensionless defocusing parameter ϵ.

significant mixing is possible, which will generally increase the finesse of the lower order mode. Conversely, if two modes are just out of resonance the mode-mixing process is frustrated, in some cases reducing the finesse slightly below what would be expected for a simple Laguerre Gaussian mode. For this cavity geometry, a resonance occurs whenever $j \times \tan^{-1} \zeta_b = \pi$, where j is an integer or rational fraction. For very long cavities ($L \gg z_0$), $j \to 2$ and the finesse saturates at a dramatically increased value. Similarly for very short cavities, ($L \ll z_0$), the Gouy shift goes to 0 and *all* the modes become nearly resonant, again increasing the finesse.

6.3 Long Cavities

The cavities used in optomechanical systems are generally composed of one small flat mirror located at the center of radius of curvature of a much larger concave mirror. This cavity, assuming it is in focus, is of the same form as eqn. 6.8, but in the limit $L \gg z_0$ and hence $R_b \to L$. In this case α is given by:

$$\alpha = \sqrt{\frac{\pi r_a r_b}{\lambda L}}, \tag{6.9}$$

which can be determined from eqn. 6.2. The finesse as a function of α for a cavity in the $L \gg z_0$ limit is shown in fig. 6.2.

6.3.1 Defocusing/Length Errors

For a real cavity, it is difficult to ensure that the smaller end mirror is exactly at the center of radius of curvature of the larger end mirror, in which case the mode wavefronts will not be perfectly matched to the end mirrors. We can calculate the effect of this defocusing by fixing R_b while adding a small offset to ζ_b:

$$\epsilon = \Delta\zeta_b = \frac{R_b - L}{z_0}, \tag{6.10}$$

which results in a quadratic phase shift in ρ for the overlap integrals of $\mathbb{B}$. The finesse as a function of α and ϵ is shown in fig. 6.2. We find that high finesse cavities are extremely sensitive to length errors; for realistic cavity geometries z_0 is $10 - 10^3$ μm, requiring the cavity length to be adjusted with an accuracy of $1-100$ nm to obtain $F > 10^6$. In practice, the loss depends only on the magnitude of ϵ and not on the sign.

6.3.2 Dielectric Mirror Penetration Depth

Because the ultra-high reflectivity dielectric mirrors used in low loss cavities have a penetration depth of order wavelength, this suggests these cavities might experience loss due to an effective defocusing. Although it would be difficult to calculate this effect in the formalism presented here, we can estimate the order of magnitude of this effect by calculating the angle-dependent phase shift of this type of mirror. The lowest loss mirrors are generally composed of alternating layers of Ta_2O_5 ($n = 2.1$) and SiO_2 ($n = 1.45$), with each layer $\lambda/4n$ thick. Consider a dielectric mirror composed of 20 layers of each material; a cavity made from these mirrors would have a reflectivity limited finesse of slightly over 10^6. The phase shift of the reflected light, $\Delta\theta$ as a function of angle of incidence, φ, can be calculated using the thin film matrix method [28], and to fourth order is given by:

$$\Delta\theta \cong -0.794\ \varphi^2 + \begin{cases} 0.736\ \varphi^4 & \text{(s polarization)} \\ -0.355\ \varphi^4 & \text{(p polarization)} \end{cases} \tag{6.11}$$

Apart from an overall phase shift, to order φ^2 the penetration depth only causes an effective change of the z position of the mirror, which can be trivially compensated for. The φ^4 term provides an uncorrectable phase shift, but the maximum practical numerical aperture (r_b/L) for a high quality optical cavity corresponds to $\varphi \lesssim \frac{1}{10}$. Thus the magnitude of this phase shift is less than 10^{-4} at the edge of the mirror. We note that in the analysis of defocusing above,

the parameter ϵ corresponds to the phase shift at the characteristic radius of the fundamental mode ($\rho = 1$). By comparison, we conclude that any effect from penetration depth should be negligible for realistic cavities ($F \lesssim 10^6$, $\frac{r_b}{L} \lesssim \frac{1}{10}$).

6.3.3 Roughness and Wavefront Error

We now consider the effects of mirror surface imperfections. Micro-roughness, which here we will take to mean roughness on scales much smaller than the mode, can be treated as an overall reduction in the mirror reflectivity. If the surface roughness has an RMS amplitude σ, the scattering loss is given by $\delta_R = 1 - e^{-(4\pi\sigma/\lambda)^2}$ [89]. The best commercially available mirrors are super-polished to a micro-roughness of better than 1 Å(on transverse scales between microns and millimeters), allowing finesses of 10^6 to be realized in the visible regime [66]. On the other hand, these mirrors may have long scale surface height imperfections, known as "wavefront error", ranging in amplitude from of order 10 nm for conventional optics to 1 Å for use in the extreme UV.

For a micro-optomechanical system, the wavefront error of the conventionally sized mirror, **B**, is the most relevant. The mirror on the optomechanical system, **A**, is typically fabricated on a semiconductor substrate, which is sufficiently flat over scales of tens of microns. We simulate wavefront error by adding random fluctuations to the Δ_b, in a cavity where we again assume $L \gg z_0$. To examine the effect of scale, we generate normally distributed random noise with a Gaussian transverse scaling function given by:

$$\tilde{A}_{k_r} = \exp\left[-8\left(1 - \frac{k_r r_b}{\pi \nu_r}\right)^2\right], \tag{6.12}$$

where k_r is the wave vector of a roughness transverse frequency component, ν_r is the mean roughness frequency relative to the mirror diameter and the factor 8 in the exponent gives the relative width of the noise in k-space – a smaller value gives randomness with a large variation in scale, while a larger value gives

a result which does not possess the desired randomness. The resulting profile is normalized to the desired RMS amplitude, σ. Some example computed wavefront maps are shown in fig. 6.3.

With roughness on only one mirror, the optimal basis states are no longer given by $\rho_a = \rho_b$. However, for $L \gg z_0$, $\rho_a \rho_b = \alpha^2$, where as before α is given by eqn. 6.9 and the individual values can be numerically optimized to maximize $|\mathbb{M}_{0,0}|$. Because random roughness breaks cylindrical symmetry it is necessary to do the overlap integral in two dimensions and calculate mixing between differing values of m. This greatly increases the computational complexity of the calculation, and so we only simulate modes for which $n, m < 20$. We also note that long scale roughness may slightly defocus the cavity; presumably in practice an experimenter would adjust the cavity length to maximize finesse. We account for this by numerically maximizing the finesse as a function of the position of mirror $\mathbf{A}$, which can be done without recalculating $\mathbb{B}$.

Results of calculations as a function of ν_r, α and σ are shown in fig. 6.3. When the roughness scale is comparable to the mode size the finesse approaches a value consistent with micro-roughness; this is because the mode mixing couples the fundamental to much higher order modes, which are not supported by the cavity. As α is increased or ν_r is decreased, the effect of wavefront distortion is dramatically reduced. In this limit the wavefront error only induces mixing in the lower order modes, which are all relatively low loss. For this reason, the effects of wavefront error are largely irrelevant in cavities with two conventionally sized mirrors (where typically $\alpha \gg 1$). Unfortunately having a large mode size on one end of the cavity is essential to allow the smallest possible mirror on the other, posing a challenge for achieving high finesse with conventional micro-optomechanical systems.

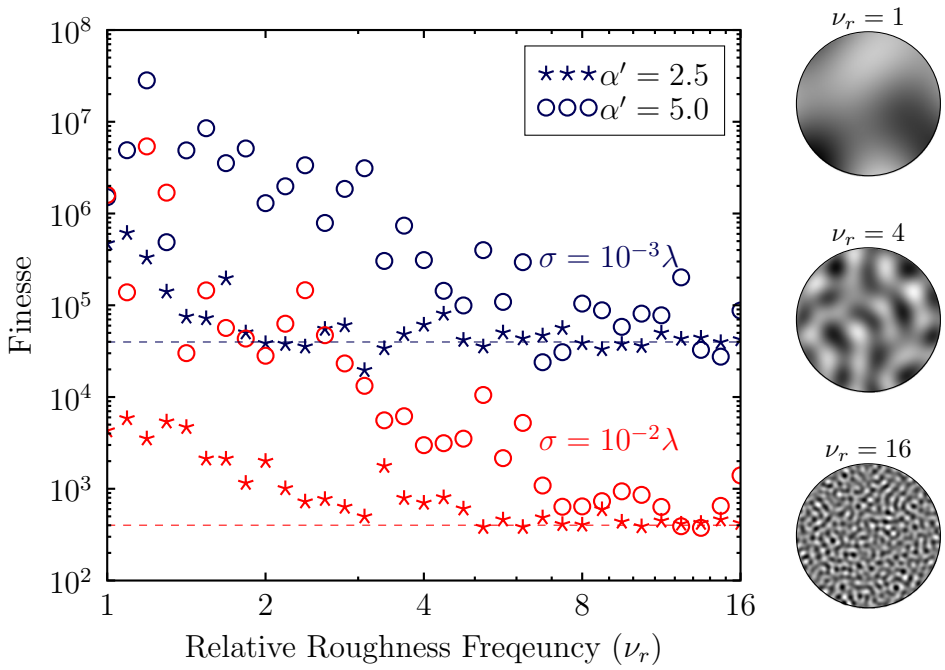

Figure 6.3: Simulated cavity finesse for the fundamental mode for rough mirrors as a function of relative roughness frequency. The large fluctuations in F are due to the random nature of the roughness profile. The expected results for micro-roughness of the same RMS amplitude are shown as dotted lines. Example roughness profiles are shown at right. As the roughness scale becomes sufficiently small (large ν_r), the roughness converges on the value expected for micro-roughness.

6.4 Short Cavities

As noted previously, a finesse enhancement is also observed for very short cavities, $L \ll z_0$, making them an attractive candidate for optomechanical systems. For simplicity we will consider a symmetric cavity, given by:

$$r_{a/b} = r \qquad z_{a/b} = \pm L/2 \qquad R_{a/b} = \pm\eta\frac{r^2}{\lambda} \tag{6.13}$$

Because of the complicated interaction between mode waist w_0 and wavefront curvature in the near-field regime, there is no clear definition of an "in focus" cavity. As a result, we characterize the mirror curvature with the dimensionless parameter $\eta = \frac{R\lambda}{r^2}$. If we fix the $z = 0$ plane at the center of the cavity, the ratio of mirror to mode size (as determined from the definition of the Laguerre Gaussian modes) is given by:

$$\frac{r_{a/b}}{w(z_{a/b})} = \rho_{a/b} = \frac{r}{\sqrt{\lambda L}}\sqrt{\frac{4\pi L z_0}{L^2 + 4z_0^2}}. \tag{6.14}$$

The optimal basis state is then determined by numerically optimizing $|\mathbb{M}_{0,0}|$ as a function of z_0. (Unlike in the long cavity case, increasing z_0, or equivalently decreasing w_0, reduces the size of the mode size on *both* mirrors but increases the wavefront mismatch; the resulting $|\mathbb{M}_{0,0}|$ overlap integral is complex enough that the optimum does not possess a closed form solution to the best of our knowledge.) For this cavity geometry, we find that the fundamental mode shape deviates more from a simple Gaussian than was previously the case, requiring calculation of modes up to $n = 100$ to get accurate results. This deviation is the result of many higher order modes being nearly in resonance simultaneously – this is only possible when the cavity is in the near field regime.

The results (fig. 6.4) show that even a small amount of curvature on the mirrors can dramatically increase the finesse in comparison to flat mirrors. In practice, the required radius of curvature for this effect is of order 1 mm for $L \sim \lambda \sim 1\mu$m,

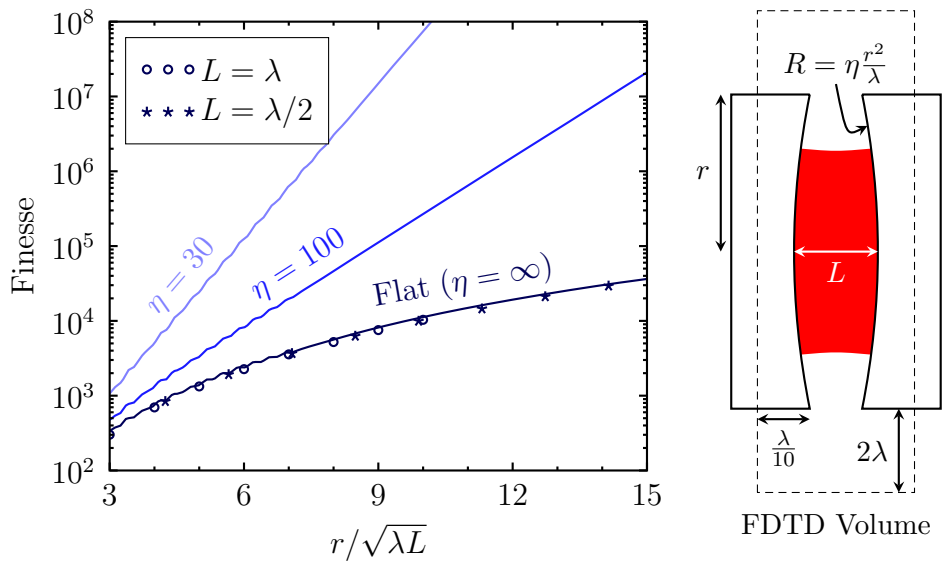

Figure 6.4: **Left:** The finesse of the fundamental mode for a short cavity with symmetric mirrors. The solid lines are the results for paraxial approximations calculations including up to $n = 100$. The fluctuations at small radii are an artifact due to the finite number of modes in the calculation. The results of FDTD simulations for flat mirrors are also shown. **Right:** A diagram of the short cavity mirror arrangement, also showing the FDTD simulated volume.

far smaller than is obtainable by conventional optical polishing. Despite this, the intrinsic stress in ion-beam deposited dielectric mirrors is high enough to produce this degree of curvature if the mirrors are free standing [90].

6.4.1 Comparison to FDTD Simulations

For cavities with $L \sim \lambda$ it is possible to do a full FDTD simulation of the electromagnetic field, owing to the small simulation volume. To do this we use the commercial software package *Lumerical FDTD**. The mirrors are represented by perfectly conducting discs of infinitesimal thickness. The simulation volume is indicated in fig. 6.4, and we use a uniform simulation mesh with a spacing of 25 nm. Due to mesh size limitations, it is only possible to simulate flat mirrors accurately. The simulated cavity is excited with a short pulse centered at the expected fundamental frequency and the resulting response of the electric field is fit to a superposition of several exponentially decaying sine waves which correspond to the different transverse modes. The results for the highest finesse modes in cavities of length λ and $\lambda/2$ and mirror radii of 3-10 λ are plotted in fig. 6.4 along with results from mode-mixing calculations. The results of the simulations agree with our previous results to within 5-10%, which is remarkable considering that the mode-mixing calculations are done in the paraxial approximation and $w_0 \sim \lambda$. Most of the difference is likely attributable to edge effects, which can cause large angle scattering that is not properly accounted for in a calculation based on the paraxial approximation.

*From Lumerical Solutions, Inc.

Chapter 7

Building a Better Optomechanical System

Although our prototype system (§4 and §5) was useful for demonstrating the basics of an optomechanical system, it falls significantly short of the criteria for demonstrating true quantum phenomena. The biggest shortcoming is the optomechanical coupling strength: for our prototype system we find that the approximate single-photon to single-phonon coupling rate is $g/\gamma_a \lesssim 10^{-4}$, and other demonstrated optomechanical systems are in a similar regime. This is due not only to the relatively low finesse, but also to the small size of the ground state wavepacket, x_0, which is determined by the mass and frequency of the micromechanical element. From our analysis in §3, we see that there is room for three orders of magnitude improvement in the finesse and another order of magnitude in the ground state wavepacket size. The method used to make the prototype micro-optomechanical resonator is apparently limited by the effect of the FIB on the tiny mirror, and commercial AFM cantilevers do not exist with sufficiently low mass and frequency. Both issues can be addressed by developing a new fabrication process using standard semiconductor fabrication procedures. In §7.1 we discuss a new process we have developed for making micro-optomechanical systems in

the UCSB cleanroom, fabricating both the mirrors and the mechanical resonators with a monolithic process.

If we wish to operate an optomechanical cavity with significant higher finesse, a number of other aspects of the system must be improved as well, including the wavefront error of the macroscopic end mirror and stability of the laser system and cavity mount. The improvements we have made to the overall system are discussed in §7.2. We also discuss our initial progress towards building a system that can operate at milliKelvin temperatures, as required for demonstrations of quantum effects.

7.1 Fabrication of the Micro-Optomechanical System

In a classic optomechanical system, the micromechanical element has two basic parts: the mirror and the resonator. The simplest possible design is to make the mechanical resonator and the mirror out of the same material. Unfortunately, this requires this material to have simultaneously ideal mechanical and optical properties. Using a dielectric mirror as the mechanical resonator results in low mechanical quality factors; for example, a standard SiO_2/Ta_2O_5 DBR mirror etched into a resonator produces a Q in the range of 10^4 [50]. In general, mechanical resonators comprised of layered materials are found to have low Q factors, apparently owing to loss at the material interfaces. Even if this could be avoided, the mass and frequency of any resonator made from mirror material is expected to be high due to the thickness of high quality mirrors ($\sim 5\mu$m); conventional micromechanical resonators can easily be made an order of magnitude thinner, resulting in a much larger ground state wavepacket size.

Another approach is to use a single layer of dielectric material, approximately $\lambda/4n$ thick, placed in the middle of a high finesse cavity; this is the previously

mentioned "membrane in the middle" approach. If aligned properly, the displacement of the membrane shifts the cavity modes in a way analogous to moving an end mirror, resulting in a functionally identical system. This system has been realized with commercially available Si_3N_4 membranes, resulting in relatively high optical quality and remarkably high mechanical Q factors, of order 10^6–10^7 at low temperatures [71]. The main disadvantage of this approach is that the finesse of the cavity is limited by the Si_3N_4 optical quality; demonstrated losses are higher than in the best dielectric mirrors, although there is room for improvement by altering the growth method. Unfortunately, the high mechanical Q is only present in tensed membranes, making it nearly impossible to achieve the low frequency required for efficient single photon-phonon coupling (§3.1). From a practical perspective, the three optical elements in the membrane approach make the system considerably more difficult to align. Although this is not a significant problem in ambient conditions, when working in a vacuum/cryogenic environment this is a significant disadvantage.

Considering these limitations, the most promising micro-optomechanical system for a superposition-type experiment at present is a small piece of SiO_2/Ta_2O_5 DBR mirror attached to a very thin resonator made from a material chosen for its low mechanical loss. As before, this will be coupled with a macroscopic curved mirror to form the optical cavity.

In general, to make the system with standard semiconductor fabrication techniques, one would start with a substrate/carrier wafer onto which the mirror and resonator layers are deposited/grown and etched into the desired shape. The resonator/mirror will be then be released from the substrate by etching away the carrier wafer underneath it. In all steps it is important to consider the interplay of different materials and their response to the various etch processes. For our devices, the highest priority is achieving high optical quality, and so we must choose etch processes that do not harm SiO_2/Ta_2O_5, or find a way to protect the mirror

during these processes.

In practice, the following issues are the most challenging:

- Whatever the mirror is deposited on must have atomic level roughness. This means either that the mirror is deposited before the mechanical material, on a bare semiconductor wafer, or the mechanical material must have extremely low roughness as deposited/grown ($\sigma \lesssim 1$ Å).
- We must be able to define/etch the mirror and resonator separately without damaging one another, especially the front surface of the mirror.
- We need a way to release the optomechanical system from the substrate without damaging the mirror/resonator.

7.1.1 Silicon Nitride as a Mechanical Material

Si_3N_4 is an attractive choice for the mechanical material in a micro-fabricated resonator: tensed membranes have been demonstrated with very high Q factors, it can be easily deposited and it has well characterized etch properties that are different from both the mirror materials and the most common substrate material, silicon. We outline the three main process steps below:

Deposition/Etching of the Silicon Nitride

Si_3N_4 can be deposited by a number of methods, the most common being PECVD (plasma enhanced chemical vapor deposition) and LPCVD (low pressure chemical vapor deposition). Although dependent on the exact deposition parameters, LPCVD and PECVD usually produce films with tensile stress, which is required for making cross or bridge type resonators with high mechanical quality factors (compressive stress makes these types of resonators buckle, resulting in extremely poor and difficult to control mechanical properties). LPCVD has the advantage of producing smoother ($\sigma \sim 1$ Å) films, but the intrinsic stress is very

Material	TMAH (10%, 85 C)	BHF	ICP (original)	ICP (modified)	CF_4 Plasma
Silicon	600	slow	-	~ 35	-
PECVD Si_3N_4	0.27	33	340	~ 200	160
SiO_2 (IBD)	0.73	340	240	~ 145	24
Ta_2O_5 (IBD)	0.04	< 0.01	165	~ 100	32
Mirror (optical)	-	-	350	210	-
Resist (various)	fast	~ 0	150	75	-

Table 7.1: Measured rates in nm/min for etchants and materials used in the micro-fabrication process. Entries marked with a "-" were not measured, but are not necessarily 0. Entries with a "$\sim$" should be regarded as approximate. Photoresist rates should also be regarded as approximate, as they were measured in several different resists, as relevant for each step of the process. The rates for the TMAH are measured in our specific setup, with the water bath temperature set at 85 C. By comparison with published results [91], we expect the sample temperature is in the range 75–80 C. The "optical rate" refers to the physical etch rate times the index of refraction – this rate is almost identical for Ta_2O_5 and SiO_2 in the CHF_3 ICP etch (by fortunate coincidence).

	Original Recipe ("SiOEtch")	Improved Recipe
CHF_3 Flow Rate	40 cm^3/min	40 cm^3/min
Ambient Pressure	0.5 Pa	0.5 Pa
RF Source	900 W	900 W
RF Forward Bias	200 W	**100 W**

Table 7.2: The process parameters of the original and modified ICP recipes used to etch the mirror. The reduced forward bias in the improved recipe reduces the etch rate but eliminates trenching almost entirely.

high, of order 1 GPa [92], making it suitable only for relatively high frequency systems. Although the tension can be controlled by altering the film stoichiometry [93], it will likely affect the optical quality. LPCVD also has the disadvantage that the deposition chamber is susceptible to contamination; this means cleanroom facilities generally only permit completely unprocessed wafers to be coated in LPCVD chambers. PECVD produces a somewhat lower quality film, with roughness on the order of 1 nm, but with a stress on the order of 200 MPa and with has fewer contamination concerns [94].

At present we have only used PECVD Si_3N_4 as a mechanical material, although it would be relatively straightforward to switch to LPCVD films if required. In either case, the Si_3N_4 can be etched in a CF_4 plasma etcher, see table 7.1 for etch rates measured on the Technics PE-IIA Plasma etcher in the UCSB cleanroom. We use a thin photoresist layer as the etch mask, with the resonator patterns defined either by contact or projection lithography. Although contact lithography is acceptable for resonators with arms of width 5 μm or larger, we find it to be unreliable for 2 μm wide resonator arms.

As discussed below, we also deposit and etch Si_3N_4 on the back side of the wafer to act as the mask for the deep silicon etch. This also has the advantage of balancing the stress of the Si_3N_4 on the front side of the wafer, eliminating most of the substrate warping that is quite prominent on 100 μm wafers.

Deposition/Etching of the Mirror

Mirror deposition is done on an ion-beam deposition (IBD) system; this is the only established method for producing ultra-high reflectivity mirrors. Deposition is possible on conventional glass mirror substrates or semiconductor wafers; either bare wafers or those coated with Si_3N_4, etc. At present we have only experimented with conventional SiO_2/Ta_2O_5 mirrors, although several other dielectric materials can be easily deposited and are occasionally used for DBR mirrors. In particular,

the Ta_2O_5 layers could be replaced with TiO_2, which has a lower density and higher index. This would significantly reduce the thickness and mass of the mirror, although it may also reduce the maximum achievable finesse or react poorly to the other process steps.

We have both deposited the mirrors ourselves (on the Veeco Nexus IBD System in the UCSB cleanroom) and outsourced the deposition to commercial companies (Advanced Thin Films, Inc. and Coastline Optics, Inc.). Although the capability to deposit our own mirrors has been instrumental in developing the fabrication process, our system produces a worse film quality than has been demonstrated commercially; the films grown in our IBD apparently limit the finesse to $F \lesssim 10^4$ at the present time*. This may be due either to the wide variety of coatings and materials used in the UCSB IBD system or non-optimal process parameters. Commercial companies extensively characterize their films and restrict the exposure of their chamber to different materials to maintain purity, producing generally higher quality films.

To etch the mirror, we use a CHF_3 plasma in a Panasonic E640 inductively coupled plasma etcher (ICP). This etch is similar to that used for the Si_3N_4, but done in a much more controlled environment. Because the etch action is primarily chemical, and not physical, this process is far gentler than cutting with a focused ion beam. In particular, there is no noticeable damage at the edges of etched mirrors, and we have no problems removing the photoresist masking layers after the etch, indicating that the mirror is never exposed to high temperatures.

With normal etching parameters (table 7.2), we found this etch to be susceptible to "trenching," where ions bouncing off the sloped sidewalls at the edge of

* This was tested by depositing mirrors on two superpolished substrates and making them into a confocal Fabry-Pérot cavity. The measured finesse was slightly over 10,000 at a pump wavelength 1064 nm. By comparison, a direct measure of mirror transmission and a thin-film calculation of the same dielectric stack indicated it should have been at least a factor of five higher. Because we do not expect this cavity to be limited by wavefront errors or mirror alignment, we attribute the loss to scattering or absorption in the mirror layers, either of which can result from impurities in the film deposition.

an etched region are concentrated around the masked features. In our case, if the Si_3N_4 layer is underneath the mirror this will cause it to be etched through completely in a ring around the mirror (fig. 7.1). This causes the mirror to completely fall off the resonator when it is released – fortunately this problem can be resolved by altering the etch conditions. We find that reducing the forward RF bias of the etch chamber by a factor of two eliminates this problem completely, at the expense of a somewhat slower etch rate.

Because of the extreme depth of the etch and the relatively poor selectivity of CHF_3 plasma, a photoresist layer of at least 5 μm thickness must be used as the mask. We use contact lithography to define the mirror pattern; the mirrors are over 10 μm in size and so feature resolution is not an issue.

Releasing the sample

Because we would like to have optical access to both sides of the resonator, we need to etch completely through the substrate wafer. There are a number of methods for doing deep silicon etches, but for simplicity we chose an anisotropic silicon wet etch. In general, anisotropic silicon etches have a much slower etch rate for the [111] plane of silicon. As shown in fig. 7.2, this effect can be used to undercut only selected features on the surface of a wafer. To exploit this effect, we designed cross resonators whose arms are at a 45° angle relative to the sides of the square substrate hole, as can be seen on the image of our photomask, fig. 7.3. The same trick can be used to fabricate cantilever-type resonators. In general, we have found cantilever resonators have a lower mechanical quality factor compared to bridge or cross resonators, on the order of 10^3–10^4; this is expected when the Si_3N_4 membranes are no longer under tension.

We used TMAH (tetramethylammonium hydroxide, $(CH_3)_4NOH$) as our anisotropic silicon etchant. Although KOH (potassium hydroxide) is more common, TMAH has a better selectivity for the resonator and mirror materials [91]. It is

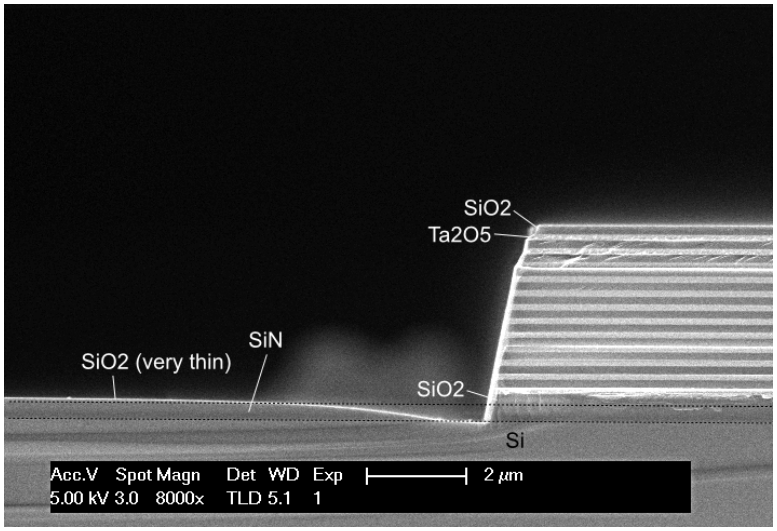

Figure 7.1: A scanning electron microscope image of a ICP etched sample cleaved through the middle of a mirror. A large amount of trenching is visible next to the edge of the etched region.

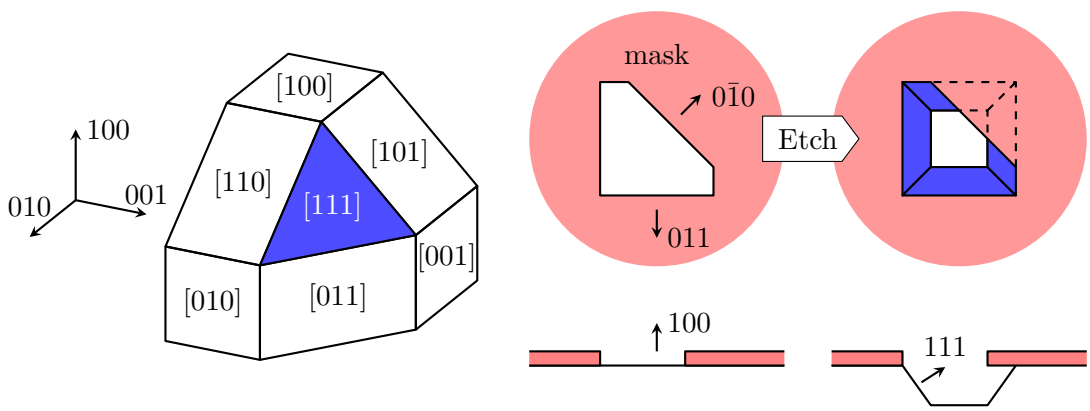

Figure 7.2: The geometry of an anisotropic silicon etch. **Left:** A diagram of some common crystal planes. The shaded plane, [111], indicates the slow direction for typical anisotropic silicon etches (for example, KOH or TMAH). **Right:** The effect of etch mask shape on undercutting for a standard [100] silicon wafer. The amount of undercutting of a masked edge depends on the angle of the edge relative to the crystal planes: edges parallel to [010] or [001] will undercut, generally leaving a square pit with [111] sidewalls. The side view (below) shows the geometry of the etched pit. The exposed [111] planes have an angle of 57.4° with respect to the wafer surface.

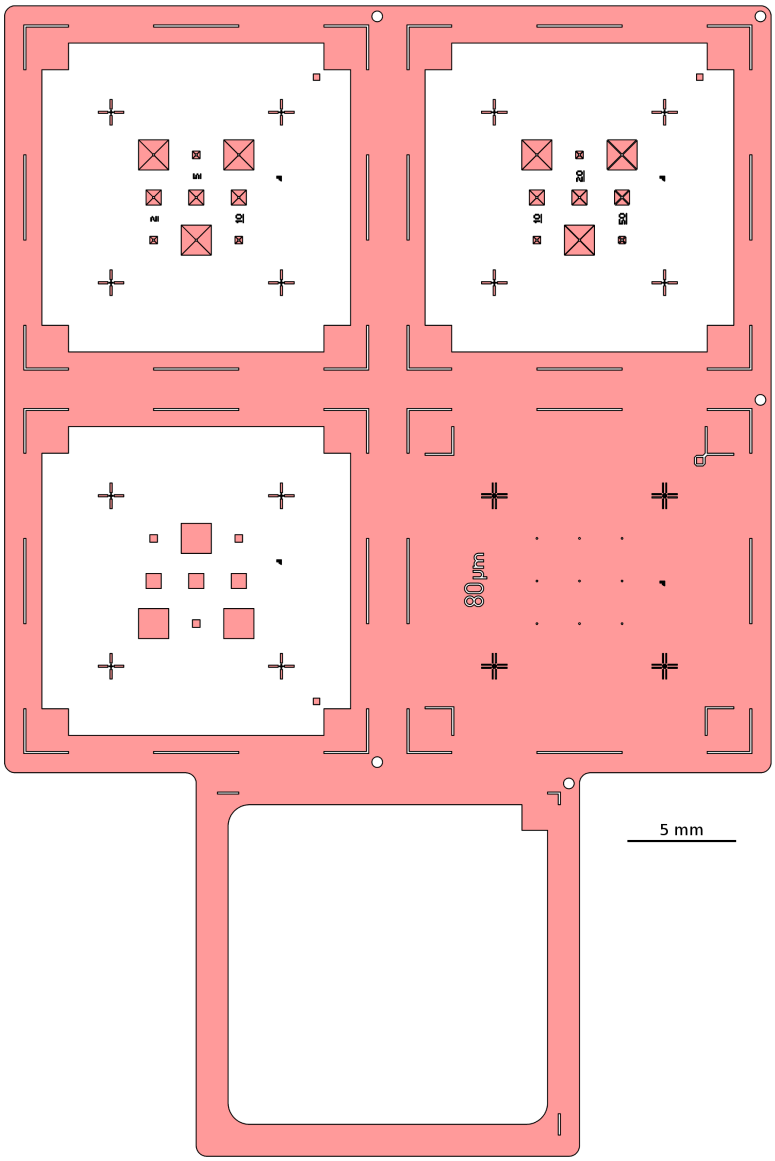

Figure 7.3: The photomask used in the original process. All device layers are on a single mask. Finished sets of devices are 14.5 mm square, with 9 devices in the central region. **Top, left and right:** the mechanical resonator (Si_3N_4) layers. The crosses have diagonals of 2, 1 and 0.5 mm. The left and right sections have different width arms; 2, 5 and 10 μm in the left section and 10, 20 and 50 μm on the right. **Center Left:** the backside layer, which defines the deep etch windows. **Center Right:** the mirror layer. The mirrors are 80 μm diameter. **Bottom:** the edge bead removal layer.

useful to keep the wafer etch time as short as possible to minimize damage to the resonator layers and undercutting of the wafer at the base of the resonator[†]. To this end, we use thin (100 μm) silicon wafers and do the deep etch from both sides simultaneously. To make a back-side etch mask, we deposit Si_3N_4 and pattern square holes that match the front-side pattern. To ensure the sides are matched, we use a contact lithography system with an IR camera and light source for which the wafer is transparent.

7.1.2 Process Order and Results

With the steps described above, it is possible to deposit the Si_3N_4 mechanical layer either on top or beneath the mirror layer. Our original approach was to process the mechanical layer first, based on the theory that potential mirror damage would be minimized if it was deposited as late in the fabrication process as possible. The detailed fabrication steps for this process are listed in §B.1. We were able to produce working resonators in this manner, although we noticed a significant fraction of the mirrors had small pieces of dirt or other defects on them. We attribute this to the fact that the front surface of the mirror is exposed during a number of processing steps and because the sample is air dried after the final etch (a normal rapid dry with compressed N_2 will definitely destroy the fragile micromechanical resonators). In some cases we also noticed that defects in the Si_3N_4 underneath the mirror carried through to the mirror layer when it was deposited on top.

[†] Significant undercutting where the resonator connects to the substrate will reduce the Q factor through what is known as clamping loss. Clamping loss occurs when the micromechanical resonator's mechanical vibration is partially transmitted into the substrate, where it becomes a traveling wave and effectively radiated away. Because the resonator is almost always much thinner than the substrate, there is an effective impedance (speed of sound) mismatch which limits the energy loss; a large undercut section can act as an impedance matcher. Unfortunately it is rather difficult to estimate the magnitude of this effect, but as long as the undercut region is much smaller than the other resonator scales it *most likely* is not the dominant loss mechanism [95].

Despite this, the best devices showed finesses in the same range as our prototype system, $F \leq 2000$, although it is somewhat unclear what the limiting factor was (see below). Mechanical quality factors were in the range of $Q \sim 10^5$, as expected for tensed Si_3N_4 at room temperature, and at least an order of magnitude of improvement can be expected at cryogenic temperatures [15, 71]. The fundamental mechanical frequencies of tested devices was in the range 10^3–10^4 kHz for cross lengths of between 0.5 and 2 mm, arms of width 2–50 μm, thickness 300–400 nm and 80 μm diameter mirrors (the frequency of individual devices agreed closely with calculations based on §A.2). The relatively large mirror size was required due to the larger radius of curvature macroscopic mirrors presently used at the operation wavelength of 1064 nm; we are currently in the process of acquiring larger mirrors that will allow tiny mirror sizes of less than 30 μm.

We subsequently modified the fabrication process to address the complications with our original process. Most importantly, we now deposit the mirror layer first, before any other processing steps. This has the important practical advantage of allowing the coatings to be done by outside companies, which are generally unwilling to put partially processed wafers in ultra-clean deposition systems. Furthermore, this also means the front surface of the mirror is facing down on the carrier wafer, and is protected during all processing steps up until the sample is released. Further protection can be obtained by making the first mirror layer from SiO_2[‡], and then stripping it in buffered hydrofluoric acid (BHF) *after* the release etch. Due to the extraordinarily low etch rate of Ta_2O_5 in BHF (table 7.1), we expect that not even a mono-layer of material would be removed in the one minute etch used to strip the top SiO_2 layer – for this reason we are confident the resulting surface should be clean and atomically smooth.

Finally, we note that the surface tension of water will often break thin res-

[‡] The front layer is usually the high index material, in this case Ta_2O_5. Adding an extra low index layer on top actually reduces the reflectivity due to the phase shift of the light reflected from the first interface.

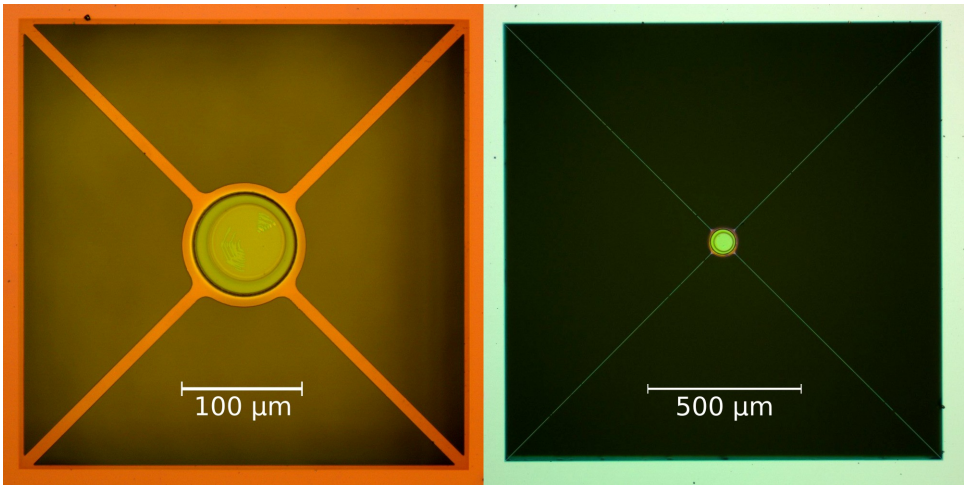

Figure 7.4: Two devices made using the improved fabrication process. Both mechanical resonators are composed of 300 nm thick Si_3N_4, with 80 μm mirrors in the center. Some scratches are visible on the "top" of the mirror (facing up in the image), which is actually the back-side of the device from the point of view of an optical cavity. These scratches, which are not present on all samples, should have negligible effect on the cavity finesse because they are not on the active mirror surface. **Left:** A cross resonator which has 500 μm length (diagonally) and 10 μm wide arms. **Right:** Another resonator, with 2 mm length and 2 μm wide arms. Despite the extreme aspect ratio, these devices can be reliably fabricated if a critical point dry is used.

onators when they are removed from etch solutions; in fact we found that resonators with 2 μm wide arms were nearly always broken after the final air dry of the original procedure. To avoid this, we transfer the samples from the TMAH solution to BHF without ever taking them above the surface of the liquid. This is done by placing the samples in a small Teflon bucket, which is transferred through several large beakers of DI water to dilute the TMAH before the sample is placed in BHF. Damage during the final drying can be avoided with a critical point dry, which takes a solution from the liquid to gas phase by going around the critical point – in this matter the sample can be dried without ever going through a liquid interface. This allows us to reliably fabricate cross resonators with arms that are 2 mm long, 2 μm wide and only 300 nm thick (fig. 7.4), which puts the resonator frequency in the 10 kHz regime with relatively high tension Si_3N_4 resonators. Fabrication of thinner resonators should be feasible; with an additional decrease in the resonator tension it may be possible to enter the sub-kHz regime. Because the Si_3N_4 is primarily a mechanical material, the reduction in optical quality that accompanies an alteration of the stoichiometry is not a concern, although lower tension material may also produce a lower mechanical quality factor.

The detailed steps for the improved fabrication process are listed in §B.2. This process produced similar results to the original process, with the exception that nearly all of the devices were clean and unbroken. We believe the finesse limitation of $F \leq 2000$ is actually caused by the macroscopic end mirror, which is specified to have a wavefront error which is on approximately the correct scale to cause this degree of loss (see §7.2.2). This issue should be resolvable with the use of larger macroscopic mirrors or smaller tiny mirrors, both of which we plan on testing in the near future. Although this may have also limited the prototype system (§4), it seems unlikely that this was the case because similar finesse was observed with 20 and 30 μm mirrors when a Ge surface protection layer was used during the FIB cutting (the larger mirrors should have been further from the diffraction limited

regime and somewhat less sensitive to wavefront error).

7.1.3 Possible Extensions

The most difficult part of developing the Si_3N_4 process above was understanding how one can perform the required etching steps without damaging the mirror. Consequently, it would be relatively easy to extend the process to fabricate mirrors with other types of mechanical resonators.

SOI Cantilevers

Perhaps the most interesting possible extension is to fabricate resonators on a thin film SOI (silicon-on-insulator) wafer. These wafers are topped with thin, $\sim$ 300 nm, layers of SiO_2 and single crystal Si. SOI wafers are used to fabricate the very high force sensitivity cantilevers used in MFRM experiments [67], which should be capable of producing an optomechanical system of low mass and frequency with a moderately high mechanical quality factor.

To explain how this could be done, we first review the basic process for making a cantilever from an SOI wafer [75]:

1. The top thin film Si layer is etched to the desired dimensions of the cantilever.

2. The back side of the sample is coated with a thick layer of material which will be used as the mask for the deep etch, usually SiO_2 or Si_3N_4 of order micron thickness. This layer is pattered to remove the regions where the carrier wafer will be etched.

3. The carrier wafer is etched completely through in the unmasked areas, using a deep dry etch or anisotropic wet etch. (If a anisotropic wet etch is used, a protective layer of SiO_2 or Si_3N_4 must first be placed on top of the cantilever

layer.) The thin SiO_2 layer underneath the cantilever acts as an etch stop, protecting the thin Si layer which will become the resonator.

4. The SiO_2 layer under the cantilever (and the protective layer, if present) is removed in a short HF etch, releasing the resonators.

5. The sample is dried in a critical point dyer, to avoid breaking the extraordinarily thin cantilevers.

Upon first reviewing this process, it appeared wholly incompatible with high reflectivity mirrors due to the (incorrect) assumption that the HF release would destroy the mirrors, which are composed entirely of oxides. With the realization that Ta_2O_5 has extraordinary resistance to etching in HF, it can be seen that the addition of mirrors is actually a rather minor modification to the process.) Although the exposed SiO_2 layers on the edges of the mirror will be slightly etched, this effect should be relatively minor if the HF etch is timed properly. In fact, all that is required is to deposit and etch the mirrors on top of the cantilever layer before the deep etch. Additionally, if the top surface of the mirror is composed of SiO_2, it will be removed completely, exposing a fresh Ta_2O_5 layer in the same manner as the improved Si_3N_4 process. All the required equipment for this process is available in the UCSB cleanroom facility, and we intend to test it in the near future.

Optomechanical Systems Suspended Above Mirrors

Another interesting possibility is a modification of the membrane-in-the-middle approach. If we remove the mirrors from the conventional Si_3N_4 process above, we can make cross-patterned Si_3N_4 membranes to be used like a conventional membrane optomechanical system, but with lower mass and frequency. Furthermore, we can avoid the complications of the three-element system alignment by fabricating the membrane on top of a dielectric mirror and a built in air spacing of, for

example, $\lambda/4$ or $3\lambda/4$. The system can then be thought of as a dielectric mirror where only the first layer is moving – a thin film calculation shows that this is nearly equivalent to moving the entire mirror. (The other end mirror remains the same as for a normal optomechanical system.) This could be fabricated relatively easily:

1. Begin with a dielectric mirror deposited on a transparent, superpolished substrate, e.g. sapphire.

2. Deposit a sacrificial spacing layer on top of the mirror. The choice of material is important; whatever is used should have an extremely high selectivity with respect to Si_3N_4 in the release etch. Alumina (amorphous Al_2O_3) is a convenient choice; smooth layers can be deposited in an IBD system (which also means it could be done at the same time as the mirror deposition) and it has a very high etch rate in BHF[§].

3. Deposit the Si_3N_4 mechanical layer and pattern it to the desired shape.

4. Undercut the mechanical resonator by etching the sacrificial layer in the areas exposed by the patterning of the mechanical layer.

5. Give the sample a critical point dry to avoid breaking the resonators.

Of course, this system has all of the disadvantages of a regular membrane approach, apart from the alignment complications. Placing a resonator only a fraction of a micron away from a flat surface may result in severe "stiction" problems [97]. Even if the resonator is stiff enough that if does not stick to the mirror, it is quite possible the surface interaction will be dissipative (due to surface charges or other interactions), severely reducing the mechanical quality factor.

[§] Despite the fact that alumina and sapphire have the same chemical formula, the etch rates in HF or BHF are completely different. In fact, sapphire's etch rate is nearly 0, while alumina etches relatively quickly [96].

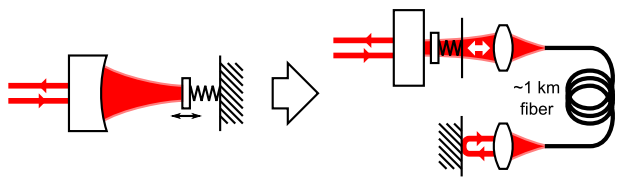

Figure 7.5: The time delay provided by the ring-down of a conventional opto-mechanical cavity could be replaced by an external delay line, e.g. in a long optical fiber.

Alternatively, a complete mirror on Si_3N_4 resonator system could also be built on top of another mirror with an engineered spacing, eliminating the big mirror of the cavity entirely. As discussed in §6.4, this may also allow for a significantly smaller mirror to be used without reducing the finesse, resulting in a lower mass opto-mechanical system. For example, a conventional optical cavity with a big mirror with $r_{big}/L = 0.1$ requires a mirror of radius 15 λ to obtain a finesse in the range of 10^6. For a short cavity system where one mirror has a radius of curvature on the order of $10^3\lambda$, the mirror radius can be a factor of 2 smaller[¶]. Of course, increasing the numerical aperture of the big mirror eliminates this advantage, but difficulties with wavefront error make this difficult to achieve in practice. As previously noted, the differing amount of stress in IBD SiO_2 and Ta_2O_5 can be used to induce the required curvature ($\sim$ 1 mm) in free standing mirrors. The curvature can also be engineered, for example, by making some mirror layers $3\lambda/4n$ thick instead of $\lambda/4n$, without affecting the peak reflectivity of the mirror.

[¶] For the big mirror system, we assume $\alpha = 2.2$ and no wavefront error ($r_{tiny} = \alpha^2\lambda/\pi\varphi$). For the small mirror, we consider a system with $\nu = 30$ and $L = \lambda$, which gives a required radius of 7–8 λ (see fig. 6.4) for both end mirrors. Presumably, the system we are describing would actually have one large flat mirror, and one small curved mirror. In this case, we expect the curvature on the small mirror would need to be approximately a factor of 2 larger. The overall loss will be slightly lower due to confining the clipping to a single mirror, although the change is expected to be less than a factor of 2 in finesse, producing a minor difference in required mirror size.

In addition to the stiction problems discussed above, the ringdown time of the optical cavity will scale with its length. This means the frequency of an optomechanical system with a short cavity needs to be extraordinarily high to enter the sideband resolved regime or do a superposition-type experiment; for a cavity length of 1 micron, this requires $\omega_c > 2\pi \times 150$ MHz (given $F = 10^6$). For such a system, the optomechanical coupling, κ, is expected to be only on the order of 10^{-2}–10^{-3} due to the increase in mechanical frequency, making a superposition-type experiment as originally conceived totally impractical.

On the other hand, it may be possible to replace the delay provided by the cavity ring-down by an external optical delay, such as a very long optical fiber (fig. 7.5). If the mechanical frequency is in the range of 10 kHz, the delay requires on the order of 10 km of optical fiber. (Optical fibers of sufficiently low loss exist to make this a feasible prospect, although the system may need to operate at telecom wavelengths of $\lambda = 1.3$–1.6 μm, which will unfortunately reduce the optomechanical coupling.) At present, it is unclear if such a system is functionally equivalent to using the intrinsic ring-down of optical cavity in a superposition or an optical cooling experiment. Of particular concern is the effect of loss (both in/out coupling and in the fiber) on the quantum interpretation of the system, and whether which-way information can be completely erased by passing light through the cavity a second time. These issues are currently under theoretical investigation.

7.2 The Complete Optomechanical System

7.2.1 Pump Laser and Cavity Locking

Our prototype system was pumped with a 780 nm tunable diode laser system, primarily for reasons of convenience. This laser has a linewidth of around several MHz, which limits measurements of the finesse via laser scanning to $F \lesssim 10^3$

(§4.2.1). Although in principle a diode laser can be stabilized so that it has a linewidth of order 1 Hz (e.g. [98]), this requires a significantly more complicated system. As a result we chose to switch to an inherently stable laser type, a Nd:YAG non-planar ring-oscillator; commercial systems are available with linewidths of order 1 kHz or less at a wavelength of 1064 nm. If desired, these systems can be frequency doubled to 532 nm; this may ultimately be a more ideal wavelength for a quantum optomechanical system. Unfortunately, working at a shorter wavelength makes the system more susceptible to scattering and absorption losses, and so we are presently fabricating systems designed for 1064 nm. The only major disadvantage of this laser is its relatively limited fast tuning range, on the order of $\Delta\omega$ = 100 MHz, implemented by a piezoelectric element pushing on the monolithic laser crystal/cavity. A larger tuning range, of order 10 GHz, is accessible with temperature tuning, but this is very slow.

The extremely narrow linewidth of an ultra high finesse cavity necessitates some sort of feedback to keep even an intrinsically stable laser locked to the cavity. In our prototype system, we used a simple method of offset fringe locking, but this had a tendency to unlock with even a moderate finesse cavity. The most commonly used locking method for high finesse cavities is known as the Pound–Drever–Hall (PDH) technique [99, 100]. The PDH method is usually implemented using an optical phase modulator operating at RF frequencies ($\sim$ 10 MHz) to create sidebands on the pump laser. Assuming these sidebands are separated from the main laser signal by more than the cavity linewidth they will be reflected from the input mirror of the cavity. These reflected sidebands interfere with the light from the original pump frequency, which is also partially reflected from the cavity if it is detuned. A measurement of the reflected power, demodulated and filtered, gives the detuning of the pump laser relative to the cavity; in particular this signal is nearly linear with detuning when close to resonance. This signal is then used as feedback to stabilize the pump laser relative to the cavity, typically

with a PID (proportional-integral-derivative) locking loop controlling either the frequency tuning of the laser or the length of the cavity.

Assuming one wishes to lock the laser to the peak of the cavity resonance, this technique has the advantage that it is null-locked. In other words, the feedback signal is zero when the system is in the desired locking position, irrespective of power fluctuations in the input beam (as opposed to a feedback system locked to some constant offset, which is sensitive to the total input power). This makes it immune to many types of technical noise, which is generally considered to be a significant advantage.

Unfortunately, the PDH technique is relatively complicated to implement, and in any case we don't always wish to lock to the peak of the cavity resonance (for example, in an optical cooling experiment). In the limit that the sidebands are not separated by more than the cavity linewidth, it is more natural to think of the PDH technique as slowly modulating the laser frequency relative to the cavity resonance. Assuming the modulation depth is much smaller than the cavity linewidth, the light reflected (or transmitted) through the cavity will undergo small modulations in intensity as the light is scanned over the cavity resonance. The depth of these modulations effectively gives the derivative of the cavity response with respect to frequency; this is in essence what the PDH technique is actually measuring.

Instead of using a RF phase modulator, we can modulate the frequency of our laser at a frequency of order 1 kHz (less than the cavity linewidth and mechanical resonance frequency) and at a depth that is only a fraction of the cavity linewidth. To generate a feedback signal, we measure the light transmitted through the cavity and feed this into a lock-in amplifier. In general, the same measurement of cavity transmission is used for other purposes, and this technique can coexist with them as long as the laser modulation frequency is far from the resonance of the optomechanical system. With the lock-in amplifier, we can measure arbitrary harmonics of the modulation signal, and so generate a feedback signal proportional

to a higher order derivative of the cavity resonance. In practice, this usefulness of higher order derivatives is limited by the measurement noise, which can be significant unless the modulation depth is comparable to the cavity linewidth.

We find that we can obtain a good signal from the second derivative with a modulation depth on the order of 10% of the cavity linewidth. The null-locking point of the second derivative is the point of maximum position sensitivity, making it ideal for measuring the mechanical resonance and doing active optical feedback cooling. This signal can be used as feedback either for the laser frequency or the cavity length using a simple integrator or PI (proportional-integral) feedback controller (the derivative term of a full PID controller is not found to be useful for this application). We find this works well at current cavity finesses ($F \sim 10^3$) and moderate laser power, ~ 1 mW, and we expect it to be appropriate for cavities with more demanding properties as well.

7.2.2 The "Big" Mirror

Although the "big" mirror of the optical cavity at first appears quite conventional, the required size of the tiny mirror is inversely proportional to the numerical aperture of the big mirror ($\varphi = r/L$). In the limit $L \gg z_0$, the radius of curvature of the mirror surface is almost exactly equal to the cavity length ($R \cong L$), and so we require superpolished mirrors whose radius of curvature is comparable to the outside diameter.

As shown in §6.3.3, the wavefront error of this mirror must also be very small, on the order of $10^{-3}\lambda$ or better at transverse scales comparable to the mirror size. In practice this is not guaranteed by traditional super-polishing techniques, both because it is very difficult to measure wavefront errors below $10^{-2}\lambda$ and because virtually no other applications require this level of perfection[‖]. The exception to

[‖] Typically the wavefront is measured several times during the polishing process and used as feedback. The process will of course not be optimized for errors that can't be resolved.

this are optics for EUV (extreme ultra-violet, $\lambda \sim 10$ nm) lithography systems. Although techniques for measuring and correcting wavefronts at the nanometer and sub-nanometer level have been developed [101], they are still in the experimental stage. The most commonly employed technique for improving long-scale wavefront errors is to selectively deposit material using, for example, a masked IBD system [102]. Generally this type of correction is applied to substrates bigger than the cm-sized mirrors we use, but in principle it should be possible to adapt this technique.

All of the experiments described in this thesis were done using mirrors of 7.75 mm diameter and either 25 or 50 mm radius of curvature, supplied by Advanced Thin Films, Inc. and Research Electro-Optics, Inc. Because the mirrors are clamped on the front surface during coating, only the central 6 mm is usable, which we will consider to be the effective size of the mirror; this results in a numerical aperture of $\varphi = 0.12$ and 0.06 for the 25 and 50 mm radius of curvature mirrors, respectively. Due to the difficulty in polishing, the 25 mm radius of curvature mirrors were provided on a limited basis and are no longer available for purchase. These mirrors were specified to <1 Å micro-roughness with a total wavefront error of better than 1/20 wave (measured at 632 nm). Unfortunately we were not provided with any wavefront maps, and we do not have the specialized equipment required to measure them, so we are unable to characterize the scale dependence of the wavefront error. We were never able to observe a finesse above 2000 with either set of mirrors coupled to a micro-optomechanical device, despite the fact that the dielectric mirrors themselves should have allowed us to achieve a much higher finesse. In the case of the 50 mm radius of curvature of mirrors, which we coated ourselves, we were able to measure a finesse of over 10^4 using two macroscopic mirrors in a confocal configuration. This suggests either that the tiny mirror or the wavefront error of the big mirror was factor limiting the finesse.

Very recently we acquired some larger numerical aperture mirrors from Coast-

line Optics, Inc. Using a custom modified polishing machine, they were able to polish 0.625 inch diameter mirrors with a 50 mm radius of curvature. With an effective mirror size of 14 mm, this corresponds to a numerical aperture of 0.14. These mirrors were superpolished and guaranteed to have a wavefront error of better than 1/20 wave, as before, but it was indicated that lower errors should be possible in practice. By request, we were also provided with a wavefront map for one of the mirrors. The reference sphere used in the wavefront measurements has a surface error of about 1/20 wave, which was found to be considerably worse than the mirrors themselves (fig. 7.6). To circumvent this measurement limitation, we asked to be provided with two surface maps of the same mirror, but with the mirror rotated by 180° between the two maps. By subtracting these two maps, we were mostly able to cancel out the imperfections in the reference sphere while retaining the anti-symmetric terms of the mirror wavefront (with respect to the mirror center). This is equivalent to using the mirror rotated by 180° as a reference for itself. The resulting wavefront map, once the tilt and focus error are removed, is shown in fig. 7.6.

Considering only the central 1–7 mm of the mirror surface (the center region is clipped to exclude a defect in the center of the particular interferometer used in the original measurement), this subtracted wavefront map has an RMS roughness of 3.0 nm, with most of the error concentrated at scales comparable to the mirror diameter. If we assume the roughness is equally distributed among the symmetric and anti-symmetric terms, we expect the real mirror RMS roughness to be smaller by a factor of $\sqrt{2}$, implying an RMS roughness of $\sigma \sim 2.1$ nm. Unfortunately, we currently have no method of confirming that the symmetric and anti-symmetric terms of the surface profile have similar magnitudes. Although one might intuitively expect this to be the case, we note that any sort of edge effects from the polishing process would be expected to show up as completely symmetric terms, and be undetectable in our analysis. In the future, we intend

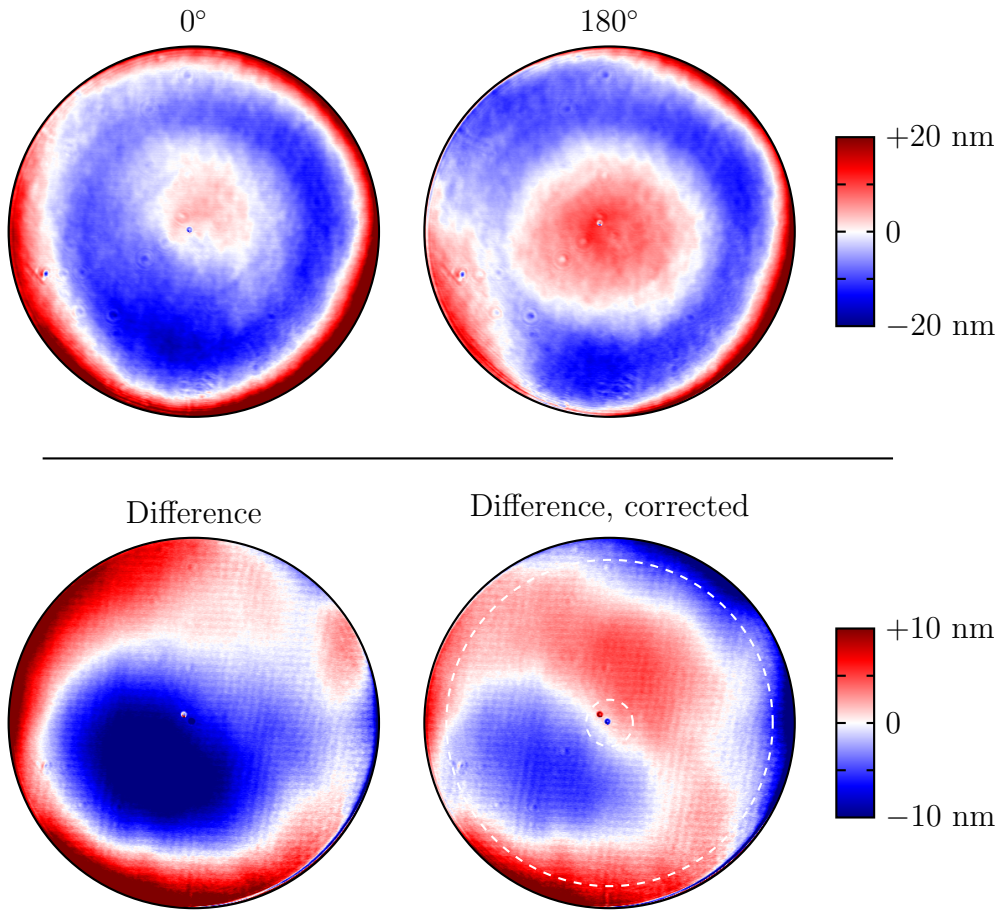

Figure 7.6: Wavefront map for the 0.625" mirror provided by Coastline Optics, Inc. Each plotted wavefront map shows the central 97% of the mirror ($r = 7.7$ mm). **Top:** The raw wavefront maps, where the sample is rotated approximately 180° between them. The wavefront error is dominated by the reference sphere. **Bottom-left:** The difference of the raw wavefront maps. The point-like defects in the center and semi-regular high-frequency noise are artifacts of the interferometric imaging system. **Bottom-right:** The wavefront map, corrected for the tilt and defocusing caused by the slightly different position of the mirror when it was rotated. This tilt/defocus is determined by a least-squares fitting of the previous map to $f(x, y) = a + bx + cy + d\,(x^2 + y^2)$. After correction, the map is seen to be nearly anti-symmetric, as expected (the deviation from perfect asymmetry is caused by the mirror not being rotated by exactly 180°). The total RMS error of the corrected map in the region $1 < r < 7$ mm, indicated with dashed lines, is found to be 3.0 nm.

to apply characterization techniques from EUV optics to these mirrors, so as to provide more concrete measurements of the wavefront error.

If we assume that our calculated roughness is approximately correct, we find that the mirrors are just shy of the required surface figure for an ultra-high finesse cavity. If the optical cavity operates at $\lambda = 1064$ nm, as is the case now, the wavefront-limited finesse should be approximately 2×10^5 if $\alpha = 2.5$ and we assume the effective roughness scale is the diameter of the mirror (i.e. $\nu_r = 1$, see §6.3.3). Furthermore, this would be a factor of 4 worse if the cavity is operated at 532 nm, as would likely be more appropriate for a superposition experiment. Some improvement may be possible by increasing the size of the tiny mirror, although in practice this may not be desirable. For example, if the tiny mirror's radius is increased by a factor of 4 (going from $\alpha = 2.5$ to $\alpha = 5$), the wavefront limited finesse is expected to increase by a factor of nearly 100. On the other hand, the mass of the mirror is increased by a factor of 16, increasing the finesse required for efficient opto-mechanical coupling by a factor of 4 (assuming ω_c is held constant). Although this seems like a net gain, the required finesse is already straining the limit imposed by the bulk reflectivity of dielectric mirrors ($F \lesssim 10^6$), and so it may not offer any real advantage. Although complicated, correcting the wavefront of the mirror is a far more attractive option in the long run. The fact that the relevant wavefront error is at scales of several millimeters is encouraging, as it means it is likely possible to adapt wavefront correction techniques from EUV optics experiments.

The mount/lens system required to test the mirrors in a real cavity is currently being fabricated. As soon as this is finished we will characterize the big mirrors in both a conventional and micro-optomechanical system. We note that if the wavefront error present in our previous mirrors was truly on the order of 10 nm, as specified, this would be enough to limit the finesse to the observed values. Thus the new mirrors should either improve the finesse or at least eliminate wavefront

error as a potential limiting factor until the finesse is considerably improved.

7.2.3 Cavity Alignment System

As discussed in §3.1.2, the critical degrees of freedom for cavity alignment correspond to the translations of the tiny mirror. For the transverse translations, the required accuracy is of order microns, over a range on the order of millimeters (as dictated by the degree of accuracy with which the system components can be "pre-aligned" by hand in their respective mounts). This accuracy can be achieved with slip-stick piezo motors, such as those used in our prototype system, which typically have a range of approximately a centimeter with a step size of 20 nm. Because they rely on piezos, they can be made to function in cryogenic and vacuum conditions, although careful choice of materials and coatings is required to obtain the same magnitude of frictional force over such a wide range of temperatures.

The length of the cavity requires an accuracy of several nanometers, better than the step size of slip-stick motors. Although a conventional piezo system seems like a good choice, electrical noise on the high-voltage amplifier poses a practically insurmountable problem. Even with a relatively short adjustment range of 100 μm, the total electrical noise of the piezo driver (a high-voltage amplifier) would need to be less than 100 nV (assuming the total range of the piezo corresponds to 100 V across the piezo element) to achieve the required cavity length stability of 10^{-13} m (see §3.5). Commonly available drivers have output noise on the order of 1 mV or higher, more than four orders of magnitude too high. Even if better drivers could be made, the long term drift of the piezo would likely be an issue (active feedback piezo positioning systems can correct this, but the positioning accuracy is only of order nm).

Despite the apparent step size limitations, slip stick motors are still probably the best choice. In general, these motors have slightly different step sizes in the forward and backward direction, and this could be exploited to achieve sub-step

resolution. We note that the cavity itself is an extraordinarily good interferometer, which can easily measure nanometer changes in cavity length and be used as feedback**.

When a slip-stick motor is off, the piezo leads are generally shorted, which should result in virtually no noise if the electrical leads are properly shielded. In this case, long term drift should be dominated by thermal expansion. Although this drift is readily apparent for ultra-high finesse cavities at room temperature, it should negligible at the required cryogenic temperatures. For example, copper has a coefficient of thermal expansion of 6×10^{-10} K^{-1} at 4 K, comparable to other common metals [103]. Assuming the general T^{-3} trend of the low temperature thermal expansion continues, the extrapolated coefficient of thermal expansion at dilution refrigerator temperatures (10 mK) is of order 10^{-17} K^{-1}. This is so low that even changing the temperature by a factor of two produces a thermal expansion that is many orders of magnitude below the required stability.

Although the θ_x-θ_y-z style cavity alignment used for the macroscopic mirror in the prototype system worked reasonably well, it is not particularly convenient for the micro-fabricated systems, which usually have multiple devices on the same sample wafer. In this case, tilting the big mirror to couple to different devices, which are 1–2 mm apart, causes the angle of the tiny mirror to be become significantly misaligned. This can be avoided by instead putting the micro-mechanical devices on an x-y-z translation stage, where the stage can be driven by the slip-stick motors. We built such a system, only to discover that conventional translation stages have extremely poor torsional stiffness. This results in low frequency ($\sim$ 100 Hz) resonances of the mechanical mount itself, which will be easily excited by ambient vibrations. In practice we found vibrations on the nanometer scale, even with the system on a vibration isolation table and in vacuum. Adding

** In the long term, this ability to measure length changes is limited by the drift of the pump laser. On the time scale of minutes, this is specified to be less than 1 MHz, which corresponds to Å-level precision.

acoustic isolation on the vacuum insert improved the situation, but the stability was still orders of magnitude worse than required.

Ultimately, this required us to return to a mount Si_3N_4 design similar to that of the prototype system. To allow us to couple to multiple devices without removing the system from vacuum, we added motors to drive the tip-tilt gimbal mount of the micro-mechanical devices. The vacuum insert is shown in fig. 7.7. Due to the presence of acoustic isolation on the new insert, we find it to be far more stable at low frequencies than the prototype system, for which significant low frequency noise was observed.

7.2.4 Cryogenic Temperatures

In the long term, we also require a system capable of operating at milliKelvin temperatures, and we have began development of a system capable of meeting this goal at the University of Leiden. Sub-Kelvin temperatures are typically reached using dilution refrigerators, which work by exploiting the natural separation of He^3 and He^4 at very low temperatures [104]. The best dilution refrigerators are capable of reaching temperatures of slightly less than 10 mK, which is apparently an order of magnitude too high for a superposition-type experiment. Lower temperatures can be achieved with the addition of a nuclear adiabatic demagnetization (NAD) stage to a dilution refrigerator [105]. A demagnetization stage consists of a large piece of material with non-zero nuclear spin which is placed in a superconducting magnet. When the superconducting magnet is turned on, typically producing a field of several Tesla, the nuclear spins will become aligned (although in practice, it may take hours or days for them to come to thermal equilibrium). If the magnet is then slowly ramped down, the spins begin to unalign and absorb thermal energy. This makes it possible to cool to extraordinarily low temperatures, in some cases even nanoKelvin or picoKelvin, although in this case there is often a thermal decoupling between the nuclear and bulk temperature.

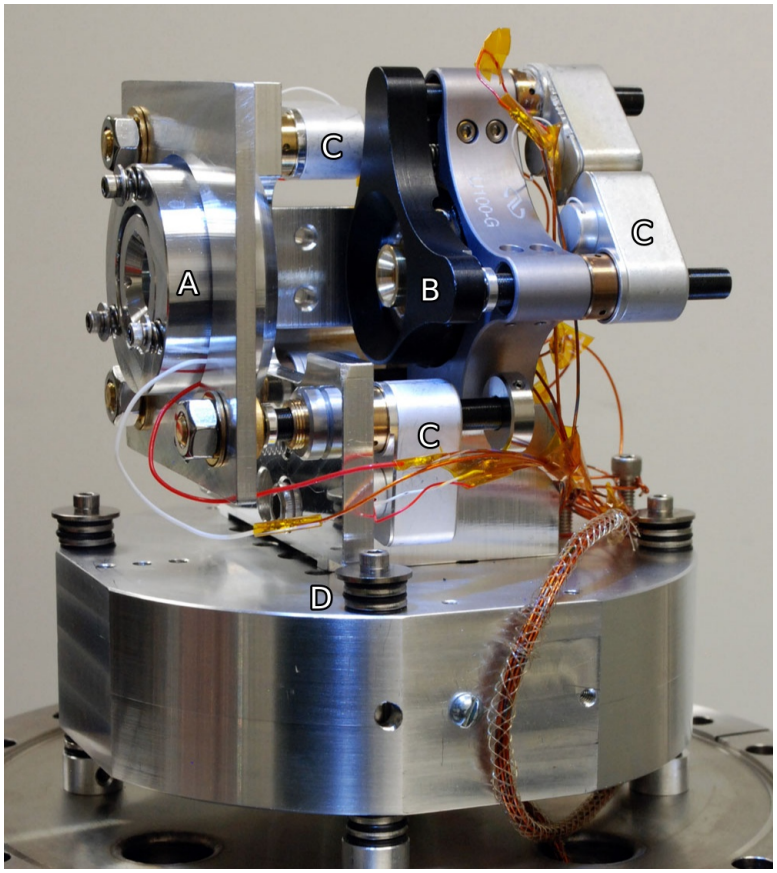

Figure 7.7: The improved vacuum cavity mount. **A)** One end of the optical cavity, with θ_x-θ_y-z alignment provided by three motors, two of which are visible. There is also an integrated piezoelectric element in the mirror holder which allows fast scanning of the cavity length (this can be easily removed or grounded for higher finesse cavities, where the piezo noise should be problematic). **B)** The other end of the optical cavity; this end mirror is mounted on a conventional gimbal optical mount controlled by motors. This mount can be mounted in several places to allow for different cavity lengths. **C)** Vacuum compatible New Focus Picomotors, which control the five axes of cavity alignment. **D)** The optical base plate, made from a 1.5" thick aluminum block. This is mounted to the top flange of the vacuum chamber via compressed viton o-rings, which, combined with the weight of the aluminum block, provide good isolation from vibrational resonances outside the vacuum chamber.

We are instead aiming for more moderate temperatures in the range of 100 μK, provided by a NAD stage composed of a large piece of ultra-pure copper in a several Tesla magnet. Because the cantilever is not mounted directly on the NAD stage[††], we expect the thermal coupling to limit the range of temperatures that can be achieved. At milliKelvin temperatures, thermal transport is dominated by the boundary resistance, known as Kapitza resistance, due to the speed of sound mismatch in different materials [104, 106]. We have built and tested a NAD stage, but we have not yet attempted to couple it to an optomechanical system.

An image of our prototype cryogenic cavity mount is shown in fig. 7.8. We couple light into the dilution refrigerator via a single mode optical fiber. The cavity transmission is presently monitored on an InGaAs photodiode located behind the optical cavity. (1064 nm photons are above the bandgap energy for Si at room temperature, but not at cryogenic temperatures, requiring different photodetectors if they are to be used inside the dilution refrigerator.) It should be possible to instead use either transition edge sensors (§3.4) or to couple the light out of the cavity via a fiber, if required.

In our initial design, the cavity mount was adjusted using slip-stick x-y-z translation stages for the mirror and micro-mechanical resonator. As with the room temperature design, which was built at around the same time, this resulted in considerable noise due to low frequency resonances in the mechanical mount. Vibration isolation inside the dilution refrigerator improved the situation, but again was not enough for experiments with an ultra-high finesse cavity. At present, there are no commercially available screw-type slip-stick motors that could be used for a θ_x-θ_y-z style mount. We are currently having custom slip-stick cryogenic position-

[††] The copper piece can not be vibration isolated, while the sample/cavity mount must be to eliminate ambient vibrations. By necessity, the superconducting magnet is immersed directly in liquid He, outside the inner heat shield of the dilution refrigerator. If the copper piece moves while the magnet field is even partially on, it generates eddy currents that cause significant heating at sub-mK temperatures. This effect is a serious concern for NAD stages, and requires that the copper piece is rigidly mounted.

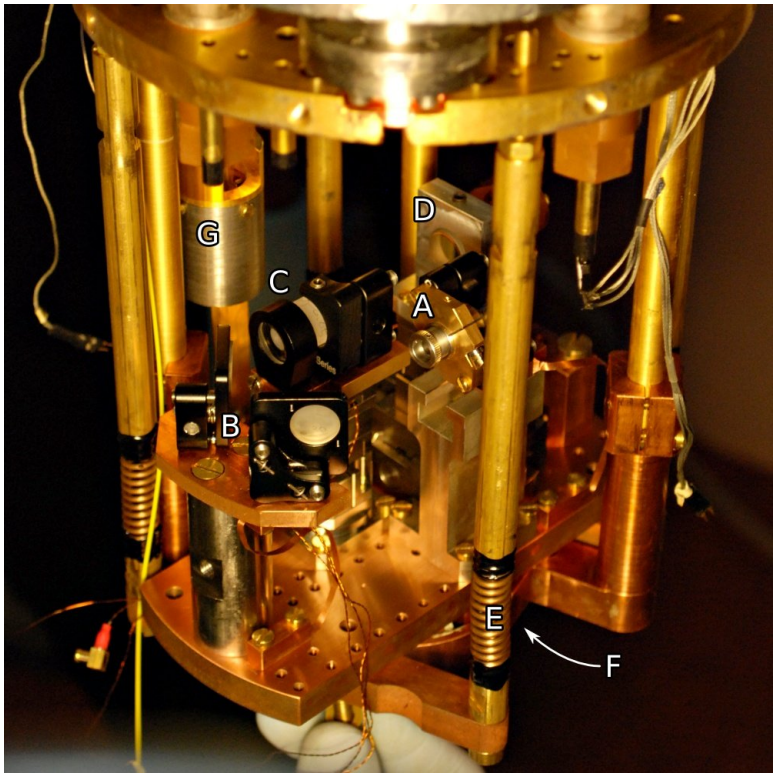

Figure 7.8: A photograph of an early version of the cryogenic cavity mount. The system is mounted to the bottom of a dilution refrigerator; the bottom of the mixing chamber is just visible at the top of the image. **A)** The lens/mount for coupling light from a single mode fiber (not shown) into the optical system. **B)** The beam steering mirrors used to match light to the cavity mode. **C)** The macroscopic mirror and incoupling lens. The cavity mirror is mounted on a nano-positioning system to control the length of the cavity. **D)** The mount for the micromechanical element. For testing the cavity alignment, a flat mirror can be used in its place (as shown). The mount is on a two axis nano-positioning stage for transverse alignment, as well as a manual goniometer for adjusting the angle. An InGaAs photodiode (not visible) is located behind the cavity. **E)** Springs to mechanically isolate the optical stage from the bottom of the dilution refrigerator. **F)** A magnetic damping system (only partially visible) to prevent large low frequency oscillations of the vibration isolated stage. **G)** A superconducting heat switch used to decouple the adiabatic nuclear demagnetization stage from the dilution refrigerator. The demagnetization stage would normally be installed underneath the optical stage and is coupled only to the mount for the mechanical resonator.

ers designed to allow us to replicate the design of the current room-temperature system, which has been demonstrated to be far more stable.

Chapter 8

Conclusion

When I began my research in Dirk Bouwmeester's group, optomechanical systems were not established as a significant field of research. We have now shown that it is possible to fabricate a high-finesse optical cavity with one tiny end mirror on a mechanical resonator; this system, with significant improvements, could be used to create a quantum superposition in an optomechanical device. We have also demonstrated optical cooling of the fundamental resonator mode in this system by over three orders of magnitude, as predicted by the extremely high signal-to-noise level observation of the cantilever's thermal motion. After our experiments on this prototype system, we began to turn our attention to better understanding the quantum nature of the proposed experiments with optomechanical systems and to making the required improvements in the micro-optomechanical system. This led to a new method for calculating the loss and mode structures of diffraction limited high finesse cavities, especially in the presence of imperfections, which is crucial to understanding the experimental requirements for constructing such a cavity. We also began to develop new micro-fabrication techniques to overcome the limitations imposed by our prototype process. We are now producing resonators with this method; although initial results are comparable to the prototype system, we expect our newfound flexibility should soon produce improved devices. Combined

with a new system capable of operating at milliKelvin temperatures, this should allow observation of true quantum effects in an optomechanical system in the near future.

Despite the significant progress in the development of optomechanical systems by many groups around the world, a true realization of quantum phenomena has been elusive. The first demonstration of non-classical behavior will almost certainly be ground state optical cooling; demonstrations of cooling to within 1–2 orders of magnitude of the ground state have already been performed in several systems [58, 59]. In a closely related NEMS experiment, it has just been reported that the ground state and phonon number state superpositions of a GHz mechanical resonator have been observed [107]. The primary barrier for ground state optical cooling with a conventional optomechanical system is working at base temperatures below the characteristically required decoherence temperature; although non-trivial, this is a technical hurdle which should be soon overcome. Barring unexpected complications, ground state optical cooling should be conclusively demonstrated in the next several years.

The biggest obstacle to a superposition-type experiment is achieving the required high optical quality in an optomechanical system. This issue may be resolved either by limiting oneself to experiments with lower optomechanical coupling requirements or by overcoming the technical hurdles for making ultra-high finesse micro-optomechanical systems. There have been several very recent proposals for quantum demonstration experiments that are possible with a lower degree of optomechanical coupling by making use of the effective enhancement observed with a strong optical field [63, 64]. These experiments have their own technical challenges, but they may be significantly easier to realize than the original proposals if the finesse of optomechanical systems can not be made comparable to the best conventional optical systems. Although all demonstrations of quantum phenomena have a number of issues that must be addressed, all the experimental

problems appear to be resolvable with current technology.

Appendix A

Mechanical Properties of Resonator Geometries

A.1 Cantilever

We will assume that the cantilever is thin and narrow compared to its length. In this case it can be treated as thin beam, where its bending is governed by the Euler-Bernoulli beam equation, which for a uniform beam cross-section is given by [108]:

$$EI\partial_x^4 u(x) = w(x), \tag{A.1}$$

where E is the elastic modulus, $w(x)$ is the beam loading and $u(x)$ is the beam displacement at a position x, and I is the second moment of the cross-sectional area; $I = \frac{bh^3}{3}$ for a square beam of width b and thickness h. (The assumption that the cross-section is uniform can be removed by assuming be letting $I \to I(x)$.)

The boundary conditions are given by:

$$\left.\begin{aligned} u&=0 \\ \partial_x u&=0 \end{aligned}\right\} \quad \text{clamped} \tag{A.2}$$

$$\left.\begin{aligned} \partial_x^2 u&=0 \\ \partial_x^3 u&=0 \end{aligned}\right\} \quad \text{free} \tag{A.3}$$

$$\left.\begin{aligned} \partial_x^2 u&=0 \\ \partial_x^3 u&=F \end{aligned}\right\} \quad \text{loaded with force } F \tag{A.4}$$

The loading function for a vibrating beam is given by:

$$w(x,t) = -\mu\ \partial_t^2 u, \tag{A.5}$$

where μ is the linear mass density, which we assume is constant. The modal solution can be found by separating out the time dependence and assuming harmonic motion:

$$\begin{aligned} u(x,t) &= \Phi(x)e^{i\omega t} \\ \Rightarrow EI\partial_x^4\Phi &= \mu\omega^2\Phi \\ \Rightarrow \Phi &= A\sin(\zeta x) + B\cos(\zeta x) + C\sinh(\zeta x) + D\cosh(\zeta x)\,, \end{aligned}$$

where $\zeta = \sqrt[4]{\omega^2\mu/EI}$. With the appropriate boundary conditions, one can find the mode frequencies and shapes.

We can simplify things by assuming the tip mass dominates, as is often the case for a dielectric mirror at the tip of a thin cantilever, and let $\mu \to 0$. In this case the solution is given by:

$$\partial_x^4\Phi = 0 \tag{A.6}$$

$$F_{tip} = m\omega^2\Phi e^{i\omega t} \tag{A.7}$$

Assuming the beam is clamped at $x = 0$ and has a mass at $x = L$, the fundamental

solution is given by:

$$\Phi = \frac{1}{2}\left[3\left(\frac{x}{L}\right)^2 - \left(\frac{x}{L}\right)^3\right] \tag{A.8}$$

$$\omega = \sqrt{\frac{3EI}{mL^3}} = \sqrt{\frac{Ebh^3}{4mL^3}} \tag{A.9}$$

$$A_{eff} = \frac{33}{140}bL \tag{A.10}$$

where we have also assumed a square cross-section. In the limit $\mu \to 0$ there are no higher order modes, or equivalently $\omega_{i>0} \to \infty$ as expected for a massless resonator. For finite μ, there of course exists a set of higher order modes, but as tip mass is increased, the amplitude at the tip vanishes, $\Phi_{i\neq 0}(L) \to 0$. This means we can safely ignore higher order modes for optomechanical systems as long as the mirror mass is much larger than the rest of the resonator – a useful effect if we want the system to behave like a simple harmonic oscillator. In fact, cantilevers used in MFRM experiments often have add large amounts of mass to the tip to suppress the amplitude of higher order modes [109].

A.2 Tensed Beam

The restoring force for the Si_3N_4 cross resonators discussed in §7.1.1 is primarily provided by the intrinsic tension in the Si_3N_4, which is created in the deposition process. Thus we will ignore the force due to the bending of the resonator and treat it as a tensed string. In this case the equation of motion for small displacements is given by:

$$f + T\ \partial_x^2 u = \mu\ \partial_t^2 u, \tag{A.11}$$

where $u \equiv u(x,t)$ is the displacement, $f \equiv f(x,t)$ is the force at a given point and $\mu \equiv \mu(x)$ is the linear mass density at a given location. To find the modal solutions, we again assume harmonic motion, resulting in:

$$f + T\ \partial_x^2 \Phi = -\mu\omega^2\Phi. \tag{A.12}$$

For an unloaded resonator pinned at both ends, the solution is simply:

$$\Phi_j = \sin\left(\frac{\pi x}{L}(j+1)\right) \tag{A.13}$$

$$\omega_j = \sqrt{\frac{T}{\mu}}\frac{\pi}{L}(j+1) \tag{A.14}$$

$$A_{eff} = \frac{1}{2}bL \tag{A.15}$$

Alternatively, if we want to consider a resonator dominated by the mass at the center (where the mirror is located), we can let $\mu \to 0$ and place a mass m at $x = L/2$. In this case the solution is trivial:

$$\Phi = \frac{1}{2} - \left|\frac{x}{L} - \frac{1}{2}\right| \tag{A.16}$$

$$\omega = \sqrt{\frac{4T}{mL}} \tag{A.17}$$

$$A_{eff} = \frac{1}{3}bL \tag{A.18}$$

Appendix B

Detailed Micro-fabrication Procedures

Our standard cleaning process is 3 minutes sonication in each of acetone/isopropanol/DI water, in that order, with a rinse in between the steps. The sample is then blown dry with compressed N_2 to avoid residue from the evaporated water.

Our standard photoresist application procedure is:

1. Give the sample a standard clean.
2. Dehydrate the sample by baking it for 5 min at 110 C.
3. Mount the sample on the vacuum chuck of a spinner and blow it with compressed air while spinning to remove any dust.
4. To improve resist adhesion, pipette HMDS onto the surface of the sample. Let it sit for 30 s and then spin it for 30 s at 3500 RPM to dry it.
5. Pipette the resist onto the sample, and spin as indicated for the resist.
6. Remove the sample from the spinner. *If indicated by the process,* remove the resist edge-bead by wiping the sample along all four edges using a swab

with EBR 100 on it.

7. Bake the sample as indicated for the resist.

B.1 Original Process

Our original (Si_3N_4 first) process was as follows:

1. Cleave a piece of a 100 μm thick silicon wafer (standard [100] surface plane) to the appropriate size, 15–16 mm square, and give it a standard clean.

2. Deposit Si_3N_4 on both the front and back-side (typically 300-400 nm on the front and 200-300 nm on the back) using the Plasmatherm 790 PECVD.

3. Apply a standard thickness (2 μm) layer of AZ4210 resist to the front side.

4. Using a optical contact aligner, roughly align the edge-bead removal mask to the center of the sample and expose it for twice the indicated exposure time for AZ4210. Develop in 4:1 AZ400K developer until the edges of the photoresist are removed. Rinse and dry the sample.

5. Using the contact aligner again, align the front side mask to the cleaved edges of the sample, which should be in the [110] direction if a standard [100] wafer is used. The angle of the mask to the crystal planes should be as accurate as possible to avoid unwanted undercutting during the anisotropic Silicon etch. Expose and develop the photoresist as indicated.

6. Etch the front side on the Technics PE-IIA Plasma etcher (300 mTorr gas / 100 W RF power for all steps).

   (a) O_2 descum: 1 min

   (b) CF_4 etch: 1 min + 1 min/100 nm Si_3N_4

(c) O_2 descum: 1 min

Some etching may occur on the edges of the backside Si_3N_4, but it should not etch through.

7. Apply AZ4210 resist to the backside, replacing the standard clean with a sonication in DI water only (to leave the front-side layer of resist intact).

8. Roughly align and expose the edge bead removal pattern to the backside. Develop until the edges are removed.

9. Align the backside mask to the front side features using an IR mask aligner. Expose and develop the photoresist.

10. To protect the front side, mount the sample upside-down on a dummy wafer with a thin layer of SantoVac vacuum grease. Etch the backside on the Technics plasma etcher, as before.

11. Put the sample in 1165 resist stripper at 80 C for 5 min or until resist is stripped. Give the sample a standard cleaning and check under a microscope for stray particles, especially at the mirror locations. Re-clean if needed.

12. Deposit the mirror in the IBD, using standard process parameters.

13. Apply a layer of 7 μm thick SPR-220-7.0 resist on the front side, wiping the edge bead away with EBR 100 before baking.

14. Align the mirror mask to the front side pattern; expose and develop resist as indicated.

15. Measure the optical reflection spectrum of the sample in one or two places without resist and where the Si_3N_4 is not etched. Keep track of the location where each spectrum is taken (to account for Si_3N_4 non-uniformity). Fit the spectra to determine the characterize the mirror and Si_3N_4 thicknesses.

16. Mount the sample on a carrier wafer with SantoVac, making sure the center is contacted with grease to the carrier wafer (the center should bulge upwards slightly due to the intrinsic stress in the unetched IBD mirror). Etch the mirror in the ICP, aiming to leave about 1 mirror layer.

17. Without unmounting the samples from the dummy wafer, measure the optical reflection spectrum of a few samples in the same locations as before. Fit these spectra to determine the amount of mirror remaining. Use this to information to recalculate the ICP etch rate.

18. Return the samples to the ICP, aiming to over-etch the mirror by 20-50 nm to account for non-uniformity.

19. Remeasure the mirror spectrum to ensure all mirror was removed and check the Si_3N_4 thickness. Return to the ICP if any mirror remains. (The ICP rate is often observed to decrease over long etches, leading to under-etching in many cases.)

20. Unmount the samples, strip the resist in 1165 and clean them.

21. Put 175 mL of 5% TMAH in a beaker and place it in a 75 C water bath. Give the TMAH solution at least 30 min to come to thermal equilibrium.

22. Mount the samples vertically in a Teflon basket. Etch them in the TMAH solution for 2 hours, or until the silicon is completely etched through.

23. Gently rinse the samples in DI water, keeping them under water as much as possible. Bake the samples, still held vertically in the Teflon basket, at 110 C for 5' or until all water has evaporated.

B.2 Improved Process

1. Cleave a piece of a 100 μm thick silicon wafer to 14±1 mm square and give it a standard clean. Check for cleanliness under a microscope, and re-clean if needed.

2. Deposit mirrors on a blank silicon wafers using the IBD. Both the top and bottom layers of the mirror should be SiO_2.

3. Apply SPR-220-7.0 resist, removing the edge bead with EBR 100.

4. Using a contact aligner, align the mirror mask layer to the edges of the sample as best as possible. (Since future layers are all aligned to this layer, alignment with the crystal planes is critical.) Expose and develop the resist.

5. Mount the sample on a carrier wafer with SantoVac. Etch the mirror in the ICP, aiming to leave about 1 mirror layer.

6. Roughly determine the amount of mirror remaining, either using a color guide or by measuring the optical spectrum in a reflectometer and fitting it.

7. Etch the mirror again in the ICP, aiming to leave about half of the SiO_2 layer. Check the thickness and etch again if any of the etched areas are have part of the bottom Ta_2O_5 layer remaining. (If the center-to-edge etch anisotropy is too high, it is acceptable, but not preferable, to etch completely through the mirror.)

8. Unmount the sample from the carrier wafer, and strip the photoresist in 1165. Give the sample a standard clean.

9. Using the Technics PE-IIA plasma etcher, do a 1 min oxygen plasma descum (300 mTorr gas / 100 W RF power). This step removes a thin polymer left from the mirror etch, and is absolutely essential for proper adhesion of the PECVD Si_3N_4.

10. Give the sample a standard clean and check for cleanliness under a microscope.

11. Deposit Si_3N_4 on the front and back sides with the PECVD.

12. Apply SPR510A resist to the front side – no edge bead removal of any type is necessary.

13. Using the GCA 6300 projection lithography system, position the sample using the alignment marks in the mirror layer. Expose the front side resonator pattern.

14. Etch the front side Si_3N_4 on the Technics PE-IIA Plasma etcher (following the directions in the original recipe).

15. Apply SPR510A resist to the back side. Replace the standard clean with a sonication in DI water only, to leave the front side resist intact.

16. Using the IR mask aligner, align the backside mask to the features on the front of the sample. Because the backside feature resolution is not critical, only contact the mask to the sample very gently (to avoid sticking the sample on the edge bead). Expose the backside pattern.

17. Mount the sample front side down on a carrier wafer using SantoVac grease.

18. Etch the back side Si_3N_4 on the Technics PE-IIA Plasma etcher, as before.

19. Remove the sample from the carrier wafer, strip the resist and 1165 resist stripper. Give the sample a standard clean and check for cleanliness under a microscope. (Note: this is the last possible cleaning step!)

20. Put 175 mL of 20% TMAH in a beaker with a reflux condenser and place the whole thing in a 80 C water bath. Give the TMAH solution at least 30 min to come to thermal equilibrium.

21. Mount the samples vertically in a Teflon basket with a solid bottom. Etch them in the TMAH solution for 2 hours, or until the silicon is completely etched through.

22. Transfer the sample basket to a large beaker of fresh DI water, being careful to keep the samples below the water line at all times. While keeping the samples under water, transfer them to a new Teflon basket and rinse the original. Repeat this dilution procedure two or three times, or until the pH of the water in the sample basket is nearly neutral.

23. Transfer the sample basket to a beaker of undiluted BHF. Etch for 1 min with gentle agitation to ensure the BHF mixes with the water in the basket.

24. Repeat the dilution procedure as before, again checking that the pH of the water in the basket is normal at the end.

25. Place the sample basket in a large beaker of ethanol. Transfer the samples, under ethanol, to the sample boat of the critical point dryer pressure vessel.

26. Transfer the sample boat into the pressure vessel and quickly seal it. As soon it is sealed, slowly let CO_2 into the pressure vessel with the release valve cracked open to let ethanol escape. Continue until the ethanol is completely displaced by liquid CO_2.

27. Close all the pressure valves and heat the vessel above the critical point of CO_2. Once the CO_2 is super-critical, release the pressure slowly (over approximately 5 minutes), and remove the sample boat. The samples should come out dry and ready to use.

Bibliography

[1] S. Mancini, V. I. Man'ko, and P. Tombesi, Phys. Rev. A **55**, 3042 (1997).

[2] S. Bose, K. Jacobs, and P. L. Knight, Phys. Rev. A **56**, 4175 (1997).

[3] S. Bose, K. Jacobs, and P. L. Knight, Phys. Rev. A **59**, 3204 (1999).

[4] W. Marshall, C. Simon, R. Penrose, and D. Bouwmeester, Phys. Rev. Lett. **91**, 130401 (2003).

[5] M. Arndt, O. Nairz, J. Vos-Andreae, C. Keller, G. van der Zouw, and A. Zeilinger, Nature **401**, 680 (1999).

[6] W. Schöllkopf and J. P. Toennies, Science **266**, 1345 (1994).

[7] C. H. van der Wal, A. C. J. ter Haar, F. K. Wilhelm, R. N. Schouten, C. J. P. M. Harmans, T. P. Orlando, S. Lloyd, and J. E. Mooij, Science **290**, 773 (2000).

[8] J. Friedman, V. Patel, W. Chen, S. Tolpygo, and J. Lukens, Nature **406**, 43 (2000).

[9] V. B. Braginsky and I. I. Minakova, Vesln. Mosk. Univ. Fiz. **1**, 69 (1964).

[10] V. B. Braginsky, A. B. Manukin, and M. Y. Tikhonov, Sov. Phys. JETP **31**, 829 (1970).

[11] V. B. Braginsky, V. A. Kuznetsov, and V. N. Rudenko, Moscow Univ. Phys. Bull. **26**, 92 (1971).

[12] V. B. Braginsky and A. B. Manukin, *Measurement of Weak Forces in Physics Experiments* (Univ. Chicago Press, 1977).

[13] H. Rokhsari, T. Kippenberg, T. Carmon, and K. Vahala, Opt. Express **13**, 5293 (2005).

[14] M. Eichenfield, J. Chan, R. M. Camacho, K. J. Vahala, and O. Painter, Nature **462**, 78 (2009).

[15] J. D. Thompson, B. M. Zwickl, A. M. Jayich, F. Marquardt, S. M. Girvin, and J. G. E. Harris, Nature **452**, 72 (2008).

[16] I. Favero and K. Karrai, Nature Photonics **3**, 201 (2009).

[17] S. Mancini, D. Vitali, V. Giovannetti, and P. Tombesi, Eur. Phys. J. D **22**, 417 (2003).

[18] D. Vitali, S. Gigan, A. Ferreira, H. R. Böhm, P. Tombesi, A. Guerreiro, V. Vedral, A. Zeilinger, and M. Aspelmeyer, Physical Review Letters **98**, 030405 (2007).

[19] V. Giovannetti, S. Mancini, and P. Tombesi, Europhysics Letters **54**, 559 (2001).

[20] I. Wilson-Rae, N. Nooshi, W. Zwerger, and T. J. Kippenberg, Phys. Rev. Lett. **99**, 093901 (2007).

[21] F. Marquardt, J. P. Chen, A. A. Clerk, and S. M. Girvin, Phys. Rev. Lett. **99**, 093902 (2007).

[22] S. Mancini and P. Tombesi, Phys. Rev. A **49**, 4055 (1994).

[23] F. K. T. Corbitt, Y. Chen and D. Ottaway, Phys. Rev. A **73**, 023801 (2006).

[24] P. T. S. Giannini, S. Mancini, Quantum Inf. Comput. **3**, 265 (2002).

[25] C. K. Law, Phys. Rev. A **51**, 2537 (1995).

[26] H. B. G. Casimir, Proc. K. Ned. Akad. Wet. **60**, 793 (1948).

[27] J. Chan, M. Eichenfield, R. Camacho, and O. Painter, Opt. Express **17**, 3802 (2009).

[28] O. Stenzel, *The Physics of Thin Film Optical Spectra: an Introduction*, Springer Series in Surface Sciences (Springer, 2005).

[29] D. Kleckner, I. Pikovski, E. Jeffrey, L. Ament, E. Eliel, J. van den Brink, and D. Bouwmeester, New Journal of Physics **10**, 095020 (2008).

[30] F. Károlyházy, Nuovo Cimento A **42**, 390 (1966).

[31] R. Penrose, General Relativity and Gravitation **28**, 581 (1996).

[32] L. Diósi, Physical Review A **40**, 1165 (1989).

[33] J. Zsolt Bernád, L. Diósi, and T. Geszti, Physical Review Letters **97**, 250404 (2006).

[34] M. A. Nielsen, I. L. Chuang, and D. F. V. James, Physics Today **54**, 60 (2001).

[35] E. Wigner, Physical Review **40**, 749 (1932).

[36] M. Hillery, R. F. O'Connell, M. O. Scully, and E. P. Wigner, Physics Reports **106**, 121 (1984).

[37] W. P. Schleich, *Quantum Optics in Phase Space* (Wiley-VCH, 2001), ISBN 3-527-29435-X.

[38] A. Kenfack and K. Zyczkowski, Journal of Optics B: Quantum and Semiclassical Optics **6**, 396 (2004).

[39] R. P. Feynman and F. L. Vernon, Jr., Annals of Physics **24**, 118 (1963).

[40] A. O. Caldeira and A. J. Leggett, Physica A Statistical Mechanics and its Applications **121**, 587 (1983).

[41] W. H. Zurek, Reviews of Modern Physics **75**, 715 (2003).

[42] A. Bassi, E. Ippoliti, and S. L. Adler, Physical Review Letters **94**, 030401 (2005).

[43] G. C. Ghirardi, A. Rimini, and T. Weber, Physical Review D **34**, 470 (1986).

[44] S. Weinberg, Annals of Physics **194**, 336 (1989).

[45] P. F. Cohadon, A. Heidmann, and M. Pinard, Physical Review Letters **83**, 3174 (1999).

[46] M. Vogel, C. Mooser, K. Karrai, and R. J. Warburton, Applied Physics Letters **83**, 1337 (2003).

[47] D. Kleckner and D. Bouwmeester, Nature **444**, 75 (2006).

[48] M. Poggio, C. L. Degen, H. J. Mamin, and D. Rugar, Phys. Rev. Lett. **99**, 017201 (2007).

[49] J.-M. Courty, A. Heidmann, and M. Pinard, Eur. Phys. J. D **17**, 399 (2001).

[50] S. Gigan, H. R. Böhm, M. Paternostro, F. Blaser, G. Langer, J. B. Hertzberg, K. C. Schwab, D. Bäuerle, M. Aspelmeyer, and A. Zeilinger, Nature **444**, 67 (2006).

[51] O. Arcizet, P.-F. Cohadon, T. Briant, M. Pinard, and A. Heidmann, Nature **444**, 71 (2006).

[52] A. Schliesser, P. Del'Haye, N. Nooshi, K. J. Vahala, and T. J. Kippenberg, Phys. Rev. Lett. **97**, 243905 (2006).

[53] T. Corbitt, Y. Chen, E. Innerhofer, H. Müller-Ebhardt, D. Ottaway, H. Rehbein, D. Sigg, S. Whitcomb, C. Wipf, and N. Mavalvala, Phys. Rev. Lett. **98**, 150802 (2007).

[54] I. Favero, C. Metzger, S. Camerer, D. König, H. Lorenz, J. P. Kotthaus, and K. Karrai, Applied Physics Letters **90**, 104101 (2007).

[55] S. Gröblacher, S. Gigan, H. R. Böhm, A. Zeilinger, and M. Aspelmeyer, Europhys. Lett. **81**, 54003 (2008).

[56] T. Corbitt, C. Wipf, T. Bodiya, D. Ottaway, D. Sigg, N. Smith, S. Whitcomb, and N. Mavalvala, Physical Review Letters **99**, 160801 (2007).

[57] A. Schliesser, R. Rivière, G. Anetsberger, O. Arcizet, and T. J. Kippenberg, Nature Physics (Advance Online Publication) (2008).

[58] S. Gröblacher, J. B. Hertzberg, M. R. Vanner, G. D. Cole, S. Gigan, K. C. Schwab, and M. Aspelmeyer, Nature Physics **5**, 485 (2009).

[59] Y.-S. Park and H. Wang, Nature Physics **5**, 489 (2009).

[60] C. H. Metzger and K. Karrai, Nature **432**, 1002 (2004).

[61] J. G. E. Harris, B. M. Zwickl, and A. M. Jayich, Rev. of Sci. Inst. **78**, 3107 (2007).

[62] C. W. Gardiner and M. J. Collett, Phys. Rev. A **31**, 3761 (1985).

[63] O. Romero-Isart, M. L. Juan, R. Quidant, and J. I. Cirac, ArXiv e-prints (2009), `0909.1469v2`.

[64] U. Akram, N. Kiesal, M. Aspelmeyer, and G. J. Milburn, ArXiv e-prints (2010), `1002.1517v1`.

[65] C. Hood, H. Kimble, and J. Ye, Phys. Rev. A **64**, 033804 (2001).

[66] G. Rempe, R. J. Thompson, H. J. Kimble, and R. Lalezari, Opt. Lett. **17**, 363 (1992).

[67] H. J. Mamin and D. Rugar, Applied Physics Letters **79**, 3358 (2001).

[68] D. Kleckner, W. Marshall, M. J. A. de Dood, K. N. Dinyari, B.-J. Pors, W. T. M. Irvine, and D. Bouwmeester, Phys. Rev. Lett. **96**, 173901 (2006).

[69] S. Gigan, H. R. Böhm, M. Paternostro, F. Blaser, G. Langer, J. B. Hertzberg, K. C. Schwab, D. Bäuerle, M. Aspelmeyer, and A. Zeilinger, Nature **444**, 67 (2006).

[70] I. Favero, C. Metzger, S. Camerer, D. König, H. Lorenz, J. P. Kotthaus, and K. Karrai, Appl. Phys. Lett. **90**, 4101 (2007).

[71] B. M. Zwickl, W. E. Shanks, A. M. Jayich, C. Yang, A. C. B. Jayich, J. D. Thompson, and J. G. E. Harris, Applied Physics Letters **92**, 103125 (2008).

[72] G. S, K. Hammerer, M. R. Vanner, and M. Aspelmeyer, Nature **460**, 724 (2009).

[73] R. G. Christian, Vacuum **16**, 175 (1966).

[74] P. Li and R. Hu, Microfluidics and Nanofluidics **3**, 715 (2007).

[75] T. D. Stowe, K. Yasumura, T. W. Kenny, D. Botkin, K. Wago, and D. Rugar, Applied Physics Letters **71**, 288 (1997).

[76] B. Cabrera, R. M. Clarke, P. Colling, A. J. Miller, S. Nam, and R. W. Romani, Applied Physics Letters **73**, 735 (1998).

[77] M. E. F. R. Blom, S. Bouwstra and J. H. J. Fluitman, J. Vac. Sci. Technol. B **10**, 19 (1992).

[78] M. Pinard, P. F. Cohadon, T. Briant, and A. Heidmann, Phys. Rev. A **63**, 013808 (2001).

[79] A. Hopkins, K. Jacobs, S. Habib, and K. Schwab, Phys. Rev. B **68**, 235238 (2003).

[80] J. Mertz, O. Marti, and J. Mlynek, Appl. Phys. Lett. **62**, 2344 (1993).

[81] K. J. Bruland, J. L. Garbini, W. M. Dougherty, and J. A. Sidles, J. of Appl. Phys. **80**, 1959 (1996).

[82] J. M. W. Milatz, J. J. van Zolingen, and B. B. van Iperen, Physica **19**, 195 (1953).

[83] L. D. Turner, K. P. Weber, C. J. Hawthorn, and R. E. Scholten, Optics Communications **201**, 391 (2002).

[84] D. Vitali, S. Mancini, L. Ribichini, and P. Tombesi, Phys. Rev. A **65**, 063803 (2002).

[85] K. Schwab, E. A. Henriksen, J. M. Worlock, and M. L. Roukes, Nature **4064**, 974 (2000).

[86] H. Kogelnik and T. Li, Appl. Opt. **5**, 1550 (1966).

[87] A. Yariv, *Optical Electronics* (Saunders College Publishing, 1991).

[88] T. Klaassen, J. de Jong, M. van Exter, and J. P. Woerdman, Opt. Lett. **30**, 1959 (2005).

[89] P. Beckmann and A. Spizzichino, *The Scattering of Electromagnetic Waves from Rough Surfaces* (Pergamon, New York, 1963).

[90] J. E. Klemberg-Sapieha, J. Oberste-Berghaus, L. Martinu, R. Blacker, I. Stevenson, G. Sadkhin, D. Morton, S. McEldowney, R. Klinger, P. J. Martin, et al., Appl. Opt. **43**, 2670 (2004).

[91] K. Biswas and S. Kal, Microelectronics Journal **37**, 519 (2006).

[92] W. Shi, H. Zhang, G. Zhang, and Z. Li, Sensors and Actuators A: Physical **130-131**, 352 (2006).

[93] Y. Toivola, J. Thurn, R. F. Cook, G. Cibuzar, and K. Roberts, Journal of Applied Physics **94**, 6915 (2003).

[94] A. Stoffel, A. Kovacs, W. Kronast, and B. Muller, J. Micromech. Microeng. **6**, 1 (1996).

[95] M. R. Geller and J. B. Varley, ArXiv e-prints (2005), `cond-mat/0512710v1`.

[96] K. Williams, K. Gupta, and M. Wasilik, Microelectromechanical Systems, Journal of **12**, 761 (2003).

[97] Z. Yapu, Acta Mechanica Sinica **19**, 1 (2003).

[98] H. Stoehr, F. Mensing, J. Helmcke, and U. Sterr, Opt. Lett. **31**, 736 (2006).

[99] R. W. P. Drever, J. L. Hall, F. V. Kowalski, J. Hough, G. M. Ford, A. J. Munley, , and H. Ward, Appl. Phys. B **31**, 97 (1983).

[100] E. D. Black, American Journal of Physics **69**, 79 (2001).

[101] K. A. Goldberg, *EUV Lithography* (SPIE Press, Bellingham, WA, 2008).

[102] T. Arnold, G. Böhm, R. Fechner, J. Meister, A. Nickel, F. Frost, T. Hänsel, and A. Schindler, Nucl. Instr. and Meth. A (2009).

[103] N. J. Simon, E. S. Drexler, and R. P. Reed, NIST Monograph **177**, 7 (1992).

[104] F. Pobell, *Matter and Methods at Low Temperatures, Third Edition* (Springer Berlin Heidelberg New York, 2007).

[105] F. Pobell, Journal of Low Temperature Physics **87**, 635 (1992).

[106] G. L. Pollack, Rev. Mod. Phys. **41**, 48 (1969).

[107] A. Cho, Science **327**, 516 (2010).

[108] C. W. de Silva, ed., *Vibration and Shock Handbook* (CRC Press, Boca Raton, FL, 2005).

[109] B. W. Chui, Y. Hishinuma, R. Budakian, H. J. Mamin, T. W. Kenny, and D. Rugar, Transducers 2003 Technical Digest pp. 1120–3 (2003).